Reconstruction of neutrino-induced showers with ANTARES

Dorosti Hasankiadeh, Qader

RIJKSUNIVERSITEIT GRONINGEN

Reconstruction of Neutrino-Induced Showers with ANTARES

Proefschrift

ter verkrijging van het doctoraat in de
Wiskunde en Natuurwetenschappen
aan de Rijksuniversiteit Groningen
op gezag van de
Rector Magnificus, dr. E. Sterken,
in het openbaar te verdedigen op
vrijdag 4 oktober 2013
om 11:00 uur

door

Qader Dorosti Hasankiadeh

geboren op 23 april 1982
te Bandarabbas, Iran

Promotor:	Prof. dr. Herbert Löhner
Beoordelingscommissie:	Prof. dr. A. M. van den Berg
	Prof. dr. P. Coyle
	Prof. dr. M. Spurio

To my parents and my family,
who gave me more than I realised

Contents

Introduction

Since the discovery of cosmic rays in 1912, new tools have been developed in order to investigate the Universe in the light of cosmic rays. Cosmic rays consist of high-energy protons and nuclei coming from space. The observations of cosmic rays have provided important contributions to our understanding of processes taking place in the dense regions of the Sun and other stars, but also have led to many discoveries in particle physics, e.g. discovery of positrons [And33], muons [NR43], and some *strange particles* [RB47]. Exploiting the advanced technologies, we now have access to very high-energy cosmic rays. The Pierre Auger cosmic-ray observatory, operating in Argentina, is currently measuring high-energy particles with ultra-high energies above 10^{17} eV [Col10]. This raises the important and intriguing questions how and from where the cosmic rays with such high energies originate. Theoretical models try to explain the origin of such ultra-high energy cosmic rays by acceleration mechanisms which are thought to take place in super-massive astrophysical objects, such as *Active Galactic Nuclei*, *Gamma Ray Bursts*, or *Supernova Remnants* (see section 2.3). However, such models cannot be easily tested, since cosmic rays do not necessarily point back to their sources, as their flight paths can be deflected by the magnetic fields in the Universe.

The very models of cosmic-ray acceleration predict non-thermal radiations from the same sources. Non-thermal radiations are high-energy photons, i.e. gamma rays, which can be produced through two different processes: 1) interactions of high-energy protons with nuclei or photons of the ambient medium can lead to the production of π^0-mesons which decay into gamma rays, or 2) if a cosmic-ray source generates a beam of high-energy electrons, these electrons may cause synchrotron radiation in local magnetic fields or may transfer their energy to an ambient photon via the *inverse Compton* scattering process, which then generates high-energy photons. Gamma-ray detectors, e.g. the H.E.S.S. experiment [HoftHC00], locate many sources of high-energy non-thermal radiation in the Universe (as an example see figure 1.1). Compared to cosmic rays, gamma rays are electrically neutral, so that they can propagate on straight lines through the Universe and may give rise to detection on Earth. However, gamma rays can be absorbed by the medium between the source and the observer. This can
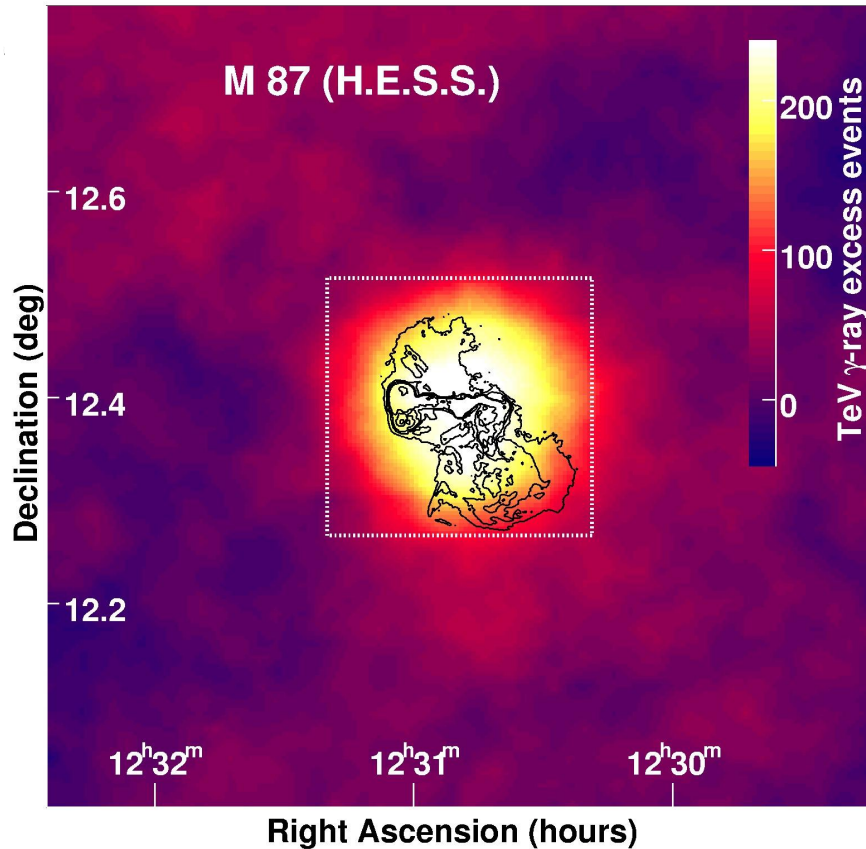
Figure 1.1: M87 radio galaxy observed by H.E.S.S. M87 consists of a supermassive black hole which may act as an engine to accelerate particles to extremely high energies. The colour presents the photon intensity and the black lines show the structure of the galaxy detected by a radio telescope. The coordinates show the position of the object on the sky. The figure is taken from [colc].

be considered as an important disadvantage for gamma-ray astronomy, specially when the aim is to study the hot and dense regions of astronomical objects, e.g. the centre of active galactic nuclei.

The interactions of high-energy charged particles with the ambient medium may also lead to the production of cosmic neutrinos, which can escape from the acceleration regions. Neutrinos are electrically neutral and, therefore, their flight paths to the Earth remain undisturbed. This property of neutrinos provides the possibility to trace back the position of neutrino sources; consequently, evidence may be derived for the acceleration mechanism of cosmic rays in astrophysical objects. Being stable particles, neutrinos can reach us from (very) distant sources. In addition, neutrinos are weakly interacting particles, so that they can penetrate regions which are opaque to photons or cosmic rays. All together, neutrinos are considered unique cosmic messengers. However, the measurement of cosmic neutrinos requires a large detector volume as a consequence of the very low interaction probability.

Historically, the Homestake solar-neutrino experiment (1970-1994) [Cle98] can be considered as the first neutrino observatory. The aim of the experiment was to measure the neutrinos produced by nuclear-fusion reactions taking place in the core of the Sun. The detection method of the experiment relies on the measure-

ment of the reaction $\nu_e + {}^{37}\text{Cl} \rightarrow {}^{37}\text{Ar} + e^-$ in a tank of chlorine. The detection of these neutrinos proved that nuclear fusion is the process supplying the energy source for the Sun.

Kamiokande [H$^+$87] and IMB [V$^+$88] (1987) were the first ever experiments which observed extraterrestrial neutrinos. A total of 19 neutrinos from a *supernova explosion* (SN1987) in the *Large Magellanic* cloud were observed. The observation confirmed theoretical models describing the core collapse of supernovae. These few observed cosmic-neutrino events have not only provided us information about the evolution of supernovae, but have also led to several limits on properties of neutrinos, such as limits on neutrino mass, charge, and magnetic moment.

ANTARES, the Deep-Sea Neutrino Telescope

The neutrinos generated in the Sun and in supernova explosions have energies in the order of several MeV, whereas the neutrinos produced by cosmic-ray accelerators are expected to have much higher energies. The two largest operating high-energy neutrino detectors, i.e. ANTARES [A$^+$11a] in the Mediterranean Sea and IceCube [HK10] at the South Pole, are able to reconstruct the direction of high-energy neutrinos up to the sub-degree precision level. This precision is sufficient to pursue astronomical research goals and the reason for the term *neutrino telescope* used for a high-energy neutrino detector. The ANTARES neutrino telescope aims to measure the high-energy neutrino flux and locate point sources in the multi-TeV energy range. Primarily this is achieved by detecting up-going muons caused by charged-current interactions of neutrinos having passed through the Earth. However, the reconstruction of neutrino-induced showers, initiated by the charged-current interaction of electron neutrinos as well as the neutral-current interaction of all neutrino flavours, extends the sensitivity of the detector to all neutrino flavours. A neutrino-induced shower consists of short-range (typically of the order of a few meters) trajectories of particles emitting Cherenkov light. Due to this property, showers have a poor angular resolution compared to muon tracks (which have a typical range of several hundred meters). However, showers are well-contained events in the detection volume. This characteristic of showers allows for a better energy estimation compared to muon tracks.

In this thesis, the emphasis is put on the measurement of neutrino-induced showers. We have pursued this measurement in order to search for a diffuse flux of high-energy extraterrestrial neutrinos. The search for a diffuse flux of extraterrestrial neutrinos from unresolved astrophysical sources can probe the existence of high-energy neutrinos. The search strategy relies on the expectation of a hard spectrum, $d\phi/dE \propto E^{-2}$, associated with the astrophysical neutrino flux ϕ, in contrast to the soft spectrum, $d\phi/dE \propto E^{-3.7}$, for atmospheric neutrinos. For diffuse-flux searches, neutrino-induced showers have two important advantages over muon-tracks induced by ν_μ interactions. First, the atmospheric neutrino background for neutrino-induced showers is lower than that for ν_μ-induced tracks. Second, as mentioned before, the measurement of showers allows a better energy estimation compared with muon tracks, which eventually leads to a better differentiation between the hard spectrum of the astrophysical neutrino signal and the soft spectrum of the atmospheric neutrino background.

A major challenge associated with the measurement of neutrino-induced showers is the selection of showers from the overwhelming background of downgoing atmospheric muons. We have developed a strategy to reconstruct and eventually select up-going neutrino-induced showers. The event selection relies on sharp criteria for observables describing the directions and topologies of shower-candidate events. To this end, we have exploited the multivariate analysis (MVA) in order to efficiently combine various selective cuts and to express them as one discriminating variable. This reduces the cut optimisation problem to a one-dimensional problem. Chapter 6 will describe the event selection in more detail.

KM3NeT, the Future Deep-Sea Neutrino Telescope of Multi Cubic-km Size

Based on the experiences of the pilot projects ANTARES [A$^+$11a], NEMO [C$^+$09] and NESTOR [Rap09], the KM3NeT collaboration plans to equip an active detection volume of multi cubic-km size at the bottom of the Mediterranean Sea with an array of Multi-PhotoMultiplier Tube Digital Optical Modules (Multi-PMT DOMs) [B$^+$11]. A DOM consists of 31 3-inch PMTs, which is designed to provide a homogeneous photon acceptance and to reduce the environmental background by local coincidences between neighbouring sensors. Even though this thesis is focused on the ANTARES data analysis, we have also studied the performance of the KM3NeT DOMs (see [H$^+$12]). Furthermore, we have taken some preliminary steps towards evaluating the potential of KM3NeT for the measurement of neutrino-induced showers [Zij11]. In the outlook of this thesis, we will discuss the prospects of this work for KM3NeT.

Outline

The outline of this dissertation is as follows. Chapter 2 gives a brief overview of cosmic-ray detection and the neutrino-production mechanisms. The ANTARES experiment is described in chapter 3. Chapter 4 summarises the simulation tools as well as the experimental and Monte-Carlo data samples used in this analysis. Chapter 5 describes the algorithm we have developed to reconstruct the parameters of neutrino-induced showers, i.e. interaction vertex, direction and energy. Chapter 6 introduces the selection strategy developed in the context of this work in order to select the shower signals induced by a diffuse flux of cosmic neutrinos. The selection strategy has been optimised by using a blind analysis method in order to prevent possible biases in the selection [HL]. Only 5% of the experimental data sample was used to study the selection strategy. After the analysis procedure was accepted by the ANTARES collaboration, the remaining 95% of the data has been processed without changing the selection criteria. Chapter 7 summarises the result obtained after the data unblinding. Finally, chapter 8 is devoted to the summary and an outlook to future observations.

Chapter

Neutrino Astronomy

The knowledge of anything, since all things have causes,
is not acquired or complete unless it is known by its
causes.

Ibn Sina (Avicenna)

The observation of high-energy cosmic rays has led to a conceptual problem that involves both astronomy and particle physics and concerns the origin and the possible production mechanisms of high-energy cosmic rays. High-energy cosmic rays consist of protons and nuclei and are thought to be produced by non-thermal processes in astronomical objects which release a large amount of energy. The locations of such astronomical objects are yet unidentified, because the flight paths of cosmic rays can be deflected by galactic magnetic fields. However, high-energy neutrinos, which can be produced by interactions of cosmic rays in or around the source, can reach the Earth undisturbed and, therefore, they are considered unique cosmic messengers. Measurements of high-energy neutrinos can provide new insight into the non-thermal processes in the Universe.

Section 2.1 describes the non-thermal processes through which cosmic rays can gain high energies. The related processes of neutrino production are described in section 2.2.

The candidates for cosmic neutrino sources and the theoretical predictions are summarised in section 2.3. Finally, section 2.5 explicitly discusses the expectations for a detectable diffuse flux of cosmic neutrinos.

2.1 High-Energy Cosmic Rays

High-energy cosmic rays are ions stripped from their surrounding electrons due to their high-speed passage through space. Cosmic rays consist of about 90% protons, 9% helium nuclei and 1% electrons, as well as a small fraction of nuclei of heavier elements [GS06]. Our current knowledge about cosmic rays is based on either direct measurements by experiments on board satellites and balloons or indirect measurements by ground-based experiments observing the extensive air showers caused by the interactions of cosmic rays with the Earth's atmosphere.
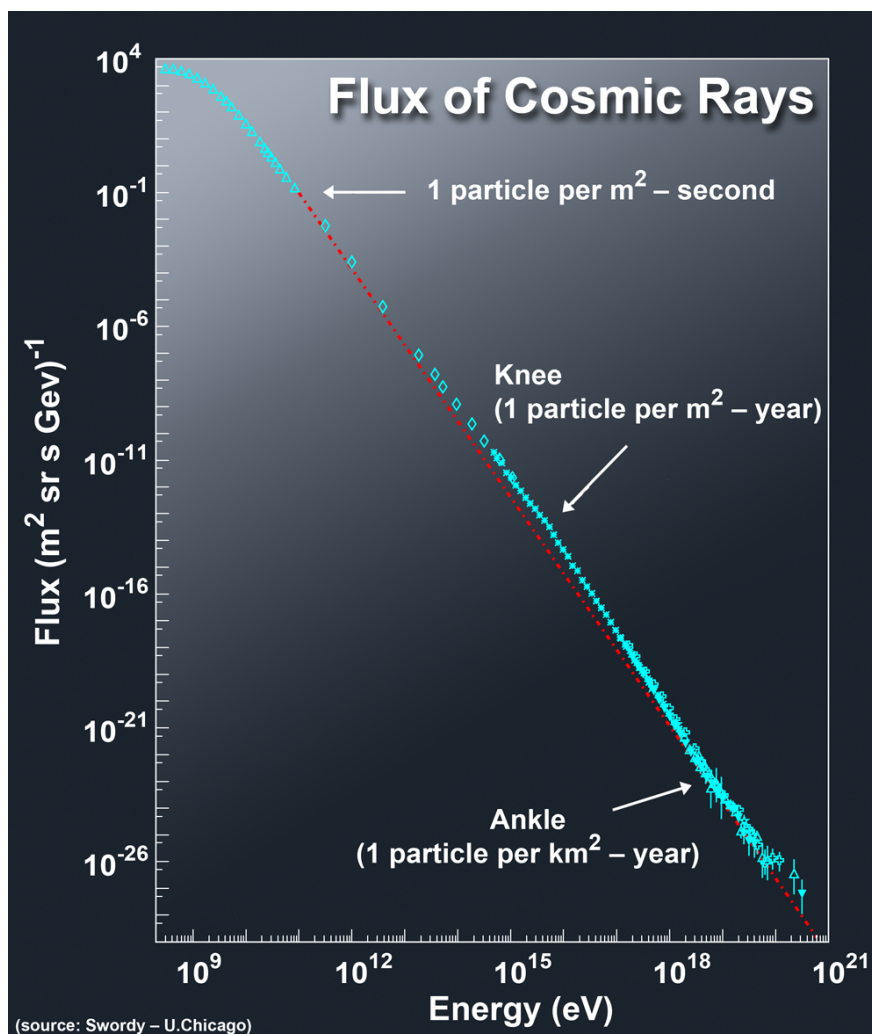
Figure 2.1: Differential energy spectrum of cosmic rays. The measured spectrum (data points) presents two abrupt changes in the spectral index just above 10^{15} eV, known as knee, and above 10^{18} eV, known as ankle, both of which deviate from the standard exponential decline (dashed (red) line). Plot taken from [Cha].

Figure 2.1 presents the measured flux of cosmic rays impinging on the Earth's atmosphere. The measured energies of the cosmic rays span many orders of magnitude, up to energies above 10^{20} eV. The spectrum follows a broken power law $dN/dE \propto E^{-\gamma}$. The measured value of the spectral index γ changes from about 2.7 to about 3.0 at an energy of about 3×10^{15} eV. The change in the spectral slope of cosmic rays may be due to several effects such as the acceleration limit of Galactic cosmic ray sources, the leakage of high-energy cosmic rays from the Galaxy and the interaction with the background photons. This phenomenon is known as *spectral knee*. At the energy about 3×10^{18} eV, the value of the spectral index changes back to about 2.7. This feature is known as *spectral ankle*. The observed cosmic rays with the energies above the ankle are expected to originate from extra-galactic sources.

The origin of cosmic rays is still an open question. Some theoretical models have been developed to explain the possible sources of cosmic rays, which will

be discussed in the following sections. These theoretical models also predict the production of high-energy neutrinos by related processes in the very sources of cosmic rays. The high-energy neutrinos can directly reach the Earth, since their propagation in space is not affected by magnetic fields in space. Relying on our current knowledge on neutrino interactions, productions and propagation, therefore, it is feasible to identify the sources of cosmic rays and reveal the mechanisms causing the very high energy release. The measurement of high-energy neutrinos requires a large detector volume as a consequence of the low interaction probability.

Before discussing the production and propagation of high-energy neutrinos, we intend to explain the acceleration mechanism of cosmic rays, in order to provide the important link between the sources of cosmic rays and high-energy neutrinos.

Fermi Acceleration

The first-order Fermi acceleration was proposed to describe the acceleration taking place in supernova shocks [Pro12]. The Fermi acceleration mechanism is applicable to strong shocks in other astrophysical contexts. Therefore, it is considered the primary acceleration mechanism responsible for accelerating particles up to the observed cosmic-ray energies. A supernova explosion ejects materials in the amount of several solar masses in the interstellar medium (ISM) with a typical speed $|\vec{u}| \simeq 10^4$ km/s driving a shock wave into the ISM. The velocity of the ejecta is related to the shock velocity $\vec{V}_s$ by hydrodynamics [Pro12]:

$$\vec{u} = \frac{3}{4}\vec{V}_s. \tag{2.1}$$

Figure 2.2 depicts the situation in the frame of an observer at rest, where the shock propagates through the stationary ISM. The acceleration occurs when the particles around the shock boundary are repeatedly reflected while crossing the shock front. The reflection can take place by elastic scattering caused by magnetic irregularities in the medium surrounding the shock. In the frame of the downstream region, the energy of a particle crossing the shock front with energy E_1 and angle θ_1 is given by:

$$E_1' = \Gamma E_1 \left(1 - \beta \cos\theta_1\right), \tag{2.2}$$

where $\beta = \frac{|\vec{u}|}{c}$, c is the speed of light in vacuum and $\Gamma = (1-\beta)^{-\frac{1}{2}}$. The energy of the particle E_2, when reflected back to the upstream region, crossing the shock front with angle θ_2 is given by:

$$\begin{aligned} E_2 &= \Gamma E_1' \left(1 + \beta \cos\theta_2\right) \\ &= \Gamma^2 E_1 \left(1 + \beta(\cos\theta_2 - \cos\theta_1) - \beta^2 \cos\theta_2 \cos\theta_1\right). \end{aligned} \tag{2.3}$$

Neglecting the terms proportional to β^2, the average fractional energy gain ϵ in one acceleration cycle considering isotropic fluxes of cosmic rays in the downstream and upstream regions, i.e. $\langle\cos\theta_2\rangle = -\langle\cos\theta_1\rangle = 2/3$, is given by:

$$\epsilon = \left\langle \frac{E_2 - E_1}{E_1} \right\rangle = \beta \left(\langle\cos\theta_2\rangle - \langle\cos\theta_1\rangle\right) = \frac{4}{3}\beta = \frac{V_s}{c}. \tag{2.4}$$
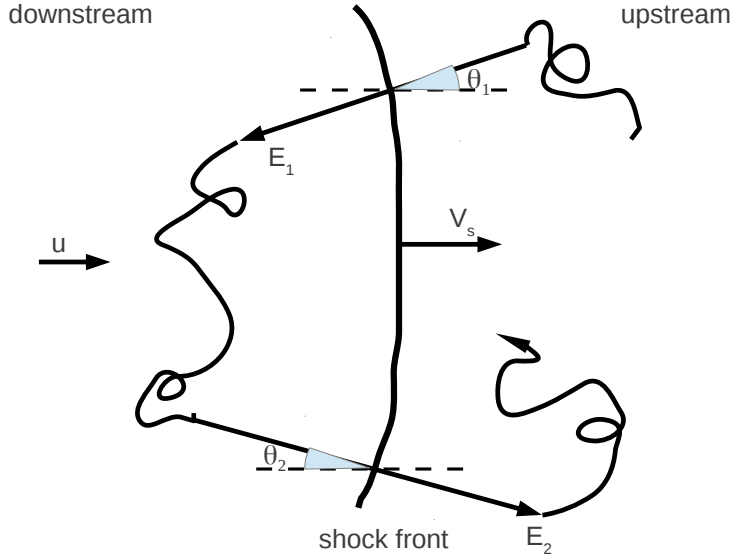
Figure 2.2: Schematic view of the first-order Fermi acceleration mechanism. A particle can be repeatedly scattered by the magnetic irregularities in the two plasmas in the downstream and upstream regions. As the particle in the upstream region gets reflected back by the downstream plasma, it gains a fraction of its original energy.

The energy of the particle linearly increases in each acceleration cycle. Therefore, in order to reach the energy E, a particle with initial energy E_0 has to bounce n_b times between the downstream and upstream regions:

$$n_b = \frac{\log{(E/E_0)}}{\log{(1+\epsilon)}}. \tag{2.5}$$

To calculate the energy spectrum of cosmic rays, we need to find the *escape probability* $P_{esc} = R_{loss}/R_{scat}$ of cosmic rays, i.e. the ratio of the rate R_{loss} of cosmic rays lost downstream to the rate of cosmic rays scattered back to the downstream region. Assuming an isotropic flux for cosmic rays in the upstream region, one can simply calculate the scattering rate R_{scat} for the cosmic rays in the upstream region travelling at speed c and angle θ to the shock normal in the frame of an observer at rest:

$$R_{scat} = \frac{n_0}{4\pi} \int_0^1 c \, \cos\theta \, 2\pi \, d(\cos\theta) = \frac{n_0 c}{4} \quad [m^{-2}s^{-1}], \tag{2.6}$$

where n_0 is the number density of cosmic rays. Since cosmic rays are advected away from the shock with velocity $|\vec{V}_s - \vec{u}|$, R_{loss} is given by:

$$R_{loss} = \frac{n_0 V_s}{4}. \tag{2.7}$$

If we have N_0 particles at time $t = 0$, there are $N_0(1 - P_{esc})^{n_b}$ left after n_b acceleration cycles. Using equation 2.5, the differential flux of cosmic rays is given by:

$$\frac{dN}{dE} \propto (1 - P_{esc})^{n_b} = \left(\frac{E}{E_0}\right)^{\frac{log(1-P_{esc})}{log(1+\epsilon)}} \propto E^{-\gamma}. \tag{2.8}$$

The last step is obtained by using the identity relation ($X^{logY} = Y^{logX}$). The spectral index γ for non-relativistic shock fronts with a Mach number M is calculated in [Gai90] resulting in $\gamma = 2 + 4/M^2$. In case $M >> 1$, $\gamma = 2$. More precise calculations predict values for the spectral index at the source between 2.1 and 2.4 [LM00].

The measured spectral index is larger and thus the spectrum is steeper than the expected spectrum at the source. This deviation can be explained by models describing the propagation and interaction of cosmic rays between the source and the Earth. For inter-galactic sources, the leakage of the high-energy cosmic-rays can cause a steeper spectrum at the Earth. The leakage can be caused by high-energy particles which have larger probability to escape from the Galaxy due to their larger gyromagnetic radii. For extra-galactic sources, the steepness can be due to the interactions of cosmic rays with the Cosmic Microwave Background which results in photo-meson production (see section 2.2), as well as electron-positron pair production. This effect is known as Greisen-Zatsepin-Kuzmin (GZK) effect, which suppresses the propagation of cosmic rays with energies above 10^{19} eV over distances larger than 50 Mpc [Gre66, ZK66].

2.2 Neutrino Production in Astrophysical Sources

The observation of cosmic rays as well as the known sources of non-thermal radiations can provide a guidance for the observation of cosmic neutrinos. Models of neutrino production rely on the decay of charged pions caused by the interactions of high-energy protons with target protons or photons surrounding the accelerating astrophysical objects:

$$\begin{aligned} p + X \to & \ \pi^{\pm} + Y \\ & \hookrightarrow \mu^{\pm} + \nu_\mu(\bar{\nu}_\mu) \\ & \quad \hookrightarrow e^{\pm} + \nu_e(\bar{\nu}_e) + \bar{\nu}_\mu(\nu_\mu) \\ p + \gamma \to & \ \pi^{+} + n \\ & \hookrightarrow \mu^{+} + \nu_\mu \\ & \quad \hookrightarrow e^{+} + \nu_e + \bar{\nu}_\mu \end{aligned}$$

(2.9)

(2.10)
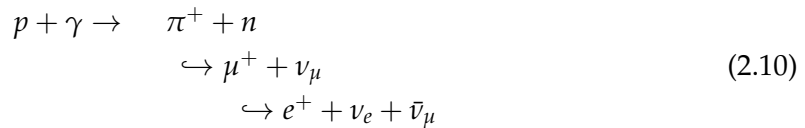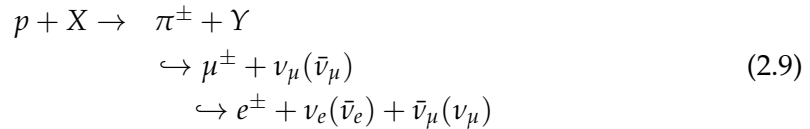
An additional outcome of the interaction can be the production of neutral pions which decay in gamma rays:

$$\begin{aligned} p + X \to & \ \pi^{0} + Y \\ & \hookrightarrow \gamma + \gamma \end{aligned} \tag{2.11}$$

Therefore, the fluxes of neutrinos and gamma rays, caused by decays of pions, are closely related. A calculation by [GSv1] shows that the two fluxes are roughly equal. However, it must be noted that the gamma rays can induce electromagnetic cascades via $e^- e^+$ pair production, which causes radiations at lower energies. Therefore, the fluxes of gamma rays and neutrinos can be related only if
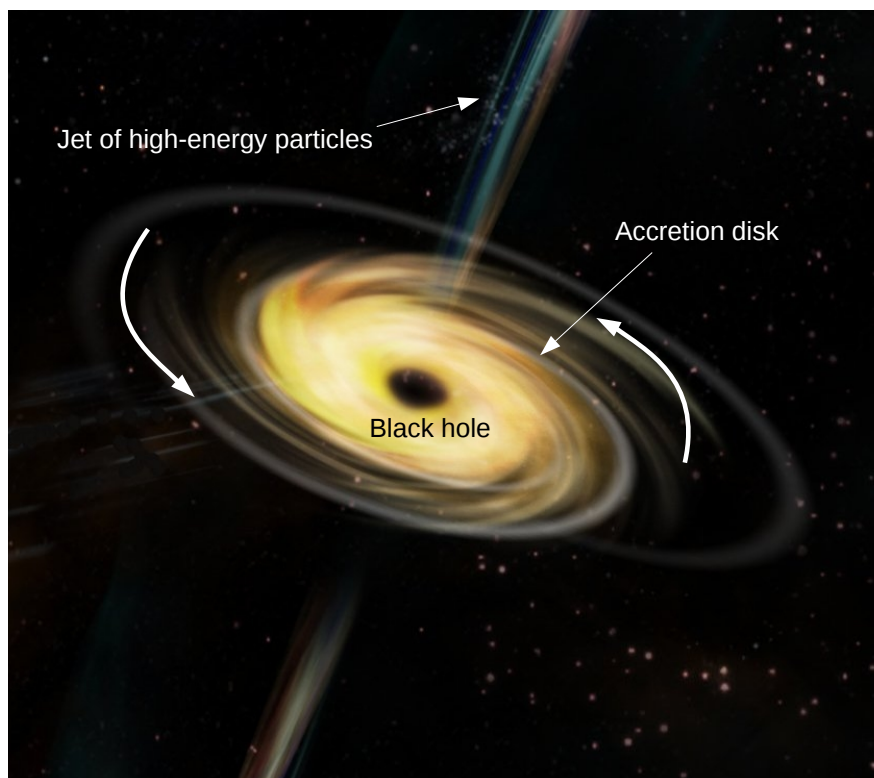
Figure 2.3: Schematic view of the standard AGN model. Picture adapted from [Bra].

the fluxes are obtained by integrating over energy. Nevertheless, the observation of gamma rays cannot necessarily indicate neutrino production in the sources. Contrary to neutrinos, the gamma rays can also be produced by electromagnetic interactions, e.g. gamma-ray production via bremsstrahlung radiation or inverse Compton scattering caused by high-energy electrons.

The range of gamma rays is limited, since they can interact electromagnetically. Neutrinos, however, are free from the electromagnetic interaction and thus can be exploited as messengers from distant sources.

2.3 Sources of Cosmic Neutrinos

Active Galactic Nuclei

An Active Galactic Nucleus (AGN) ranges among the brightest gamma-ray sources in the Universe. Therefore, AGNs are considered as the most promising candidate for neutrino sources. Although AGNs are compact objects, their energy emission is comparable to that of an entire galaxy [Ree84].

Figure 2.3 schematically illustrates the standard AGN model. AGNs consist of a super-massive black hole (10^8 Solar masses) located at the centre of a galaxy, surrounded by matter in an accretion disk. The matter is heated in the accretion disk and spirals into the black hole. The heated matter is ejected by relativistic jets perpendicular to the disk.

AGNs with a relativistic jet pointing to the Earth are called Blazars. Markarian 421 [K+01] is one of the blazars closest to the Earth and has been observed to

produce gamma-ray signals with an energy spectrum between 260 GeV and 17 TeV. Typically the emission spectrum of AGNs ranges over the full electromagnetic spectrum, from radio wavelengths to TeV gamma rays. Currently there are two models describing the observed spectrum of AGNs: leptonic [G$^+$17] and hadronic jet [Sik10] accretion models. The leptonic models rely on inverse Compton scattering of relativistic electrons on abundant photons emitted by synchrotron radiation from the radio jet. Thus the low-energy synchrotron photons are up-scattered to high-energy photons. On the other hand, hadronic models, as discussed before, rely on the photo-meson production caused by the interaction of high-energy protons with abundant photons in the surrounding medium. A combined model, exploiting both leptonic and hadronic emission processes, fits well to the observed spectrum of many AGNs [A$^+$80].

Gamma-Ray Bursts

Gamma-ray bursts (GRBs) are the most luminous electromagnetic sources known in the Universe. The amount of energy that GRBs can release in a few seconds is larger than the energy that the Sun will emit in its entire 10 billion-years lifetime. The typical energy release of a GRB corresponds to the conversion of about 1% of the mass of the Sun into energy. GRBs emit gamma rays in a short time window between a few milliseconds to a few seconds. Depending on the duration of the emission time window, GRBs are classified into two main classes: *long GRBs* and *short GRBs*.

Long GRBs have an average duration of 30 seconds. The studies shows that the long GRBs are associated with Supernovae, i.e. the explosive death of massive a star, which occurs when the core collapses to a neutron star or a black hole, and galaxies with rapid star formation [G$^+$08]. Short GRBs last for some fractions of a second. Short GRBs typically emit a total kinetic energy which exceeds that of long GRBs by several orders of magnitude. It is believed that short GRBs are associated with processes relying on the mergers of neutron star - neutron star binaries or neutron star - black hole binaries [LRR07]. The binary system loses its energy due to gravitational radiation and spirals closer until the tidal forces disintegrate the neutron star. This process releases a tremendous amount of energy in a short period of time before merging into a single black hole takes place.

Despite the different processes governing the two GRB classes, the acceleration mechanisms which give rise to the gamma-ray emission most likely are independent of the GRB class. Figure 2.4 schematically presents a so-called Fireball model [MR93], the most favoured model for GRBs. The model proposes a relativistic expanding fireball caused by an explosion initiated by the collapsing core of a massive star or the merger of two compact objects. Therefore, the model probes ultra-relativistic electrons and protons accelerated in the relativistic expanding fireball. High-energy protons can initiate photo-meson production which subsequently can cause neutrino production.

Supernova Remnants

A massive star (with a mass 8 times heavier than the Solar mass) at the end of its life can initiate an explosion releasing an amount of energy of about 6.24×10^{52}
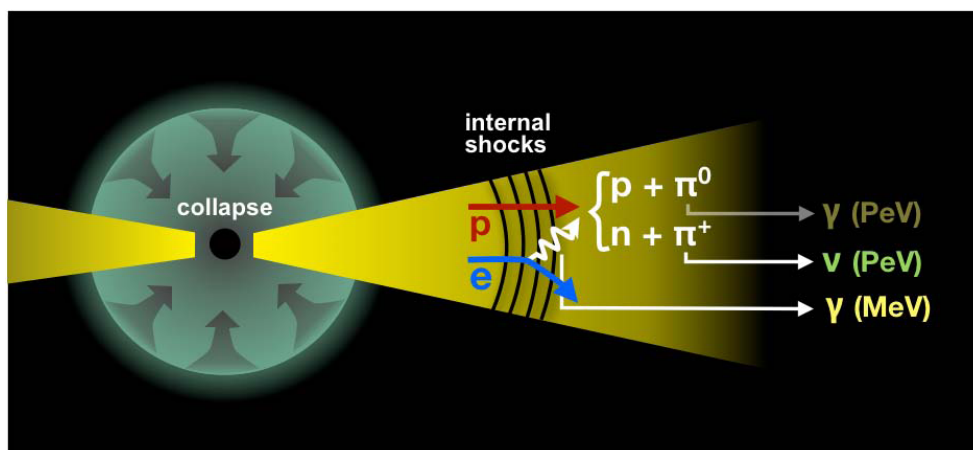
Figure 2.4: Schematic view of a Fireball-GRB model. Picture taken from [uIfHEI].

TeV [vdS$^+$40]. About 99% of this energy is emitted as neutrinos in the MeV range. The remaining energy is propagated into the interstellar medium forming a relativistic shock wave which may cause particle acceleration. As a consequence, the interaction of accelerated protons with the ambient matter can cause photo-meson production which ultimately may lead to the production of high-energy gamma rays and neutrinos. Supernova remnants (SNRs) have been observed which provide evidence for proton acceleration [G$^+$68, E$^+$22].

The remnant of a supernova explosion is a rapidly spinning neutron star with pulsed radio emission, which is called *Pulsar*. A constant outflow of particles from the Pulsar's magnetosphere creates the Pulsar wind nebula. The wind can hit the interstellar medium and can eventually cause shock waves and photo-meson production. Alternatively, the magnetic field of a rapidly spinning neutron star can accelerate protons [Roy99]. The supernova remnants can provide a target for accelerated protons and can ultimately initiate the high-energy neutrino production.

SNRs are the most promising galactic sources of neutrino production. In particular, the SNR RXJ1713 [Col11] is one of the best known galactic sources emitting high-energy gamma rays. This potential source can be used as a prime target for KM3NeT, the future deep-sea neutrino telescope [ATftKC13].

Microquasars

Microquasars are galactic objects associated with X-ray binary systems (see figure 2.5). Microquasars consist of a central compact star, e.g. a neutron star or a black hole, which attracts matter from a companion *red giant* star. Therefore, a microquasar resembles a small AGN accreting matter and, therefore, leading to the formation of relativistic jets which may cause particle acceleration [Z$^+$10]. Consequently, the interaction of the accelerated protons with the synchrotron photons caused by accelerated electrons can cause neutrino production.
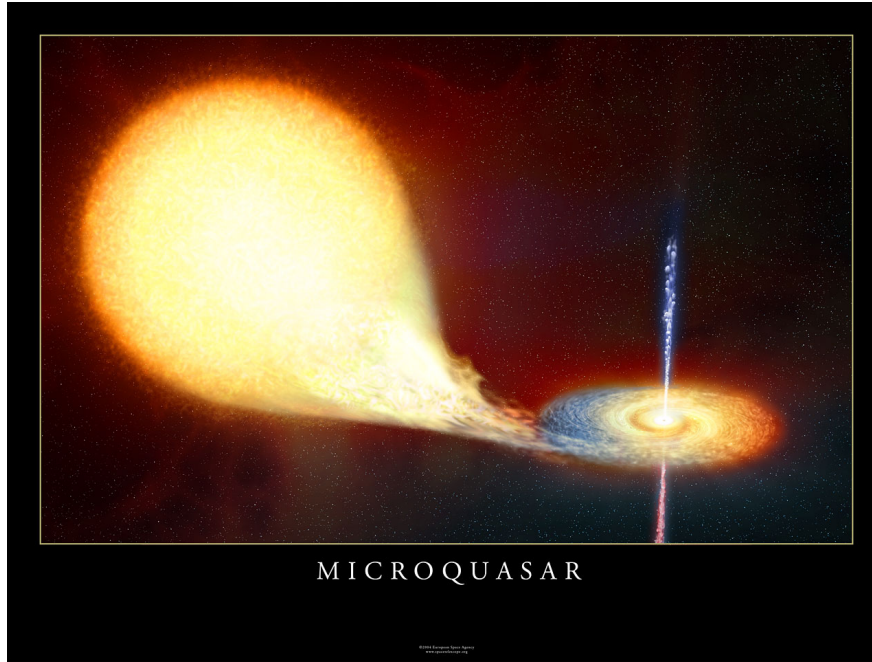
Figure 2.5: Schematic view of a Microquasar accretion process. Picture taken from [ESA].

2.4 Atmospheric Muons and Neutrinos

The interaction of cosmic rays with the air in the atmosphere causes a cascade of particles, i.e. an air shower. Similar to the process described in section 2.2, atmospheric muons and neutrinos are produced through the decay of pions in the air shower. Among all particles produced in the air shower, atmospheric muons are abundantly detected by underground or underwater neutrino telescopes aiming at neutrino detection and present a serious background for the detection of astrophysical neutrinos.

The rate of atmospheric muons in the ANTARES detector is about 1-10 Hz which exceeds the rate of neutrinos by several orders of magnitude (see figure 2.6). A large number of these muons can be rejected by selecting only upgoing events, exploiting the Earth as the natural filter against all charged particles (see section 3.1.1). However, muon bundles produced in the same air shower induce events which can be misinterpreted as up-going events [Hei04]. A muon bundle consists of multiple muons produced by an interaction of a primary cosmic ray, passing the detector so that their signals are causally connected.

Atmospheric muon neutrinos are produced through the decay of pions and kaons while the electron neutrinos are mostly produced in $K^{\pm}$ and K_L^0 decays. The flux of the atmospheric neutrinos is also shown in figure 2.6. The mean free path of pions and kaons in the atmosphere is shorter than their decay length for energies above 100 GeV. Therefore, the energy spectrum of the emerging neutrinos becomes steeper, i.e. $dN/dE \propto E^{-3.7}$. This property of atmospheric neutrinos allows to discriminate them from astrophysical neutrinos with a harder energy spectrum $dN/dE \propto E^{-2}$.
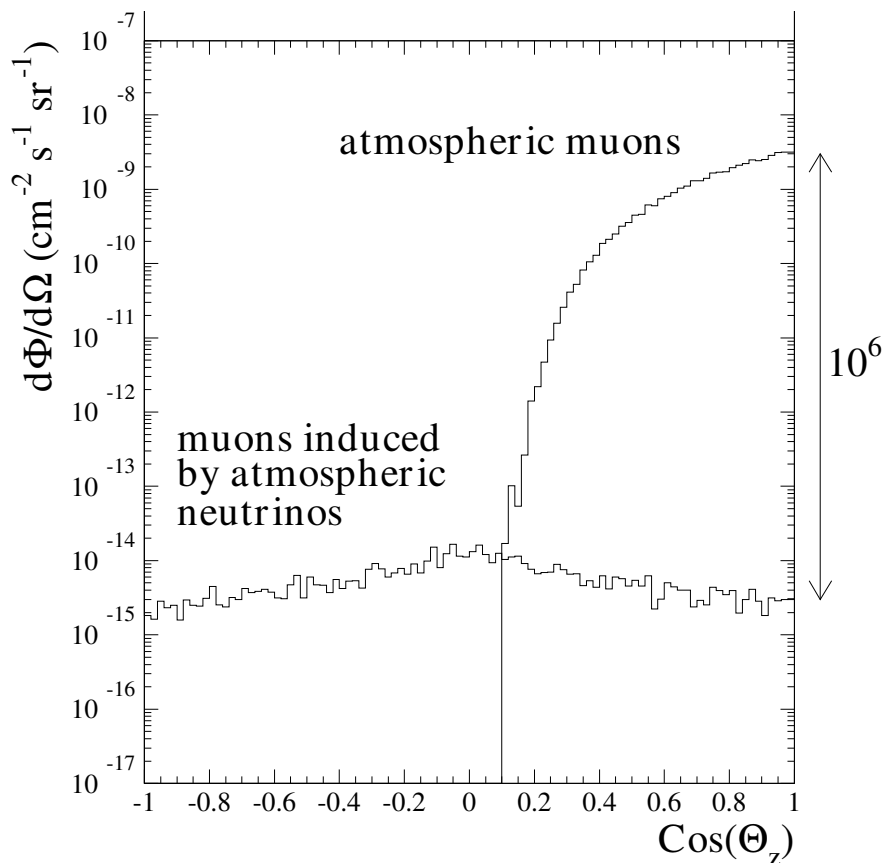
Figure 2.6: Flux of atmospheric muons and muons induced by atmospheric neutrinos as a function of the cosine of the zenith angle Θ_z. The figure is taken from [Col32].

2.5 Diffuse Cosmic Neutrinos

The observation of previously described individual sources of high-energy neutrinos can furnish the most direct way of probing the existence of cosmic neutrinos. In practice, the direct observation of high-energy neutrinos by the ANTARES detector can be challenging due to the low intensity of such sources [Bia10]. However, the measurement of a so-called diffuse flux of extraterrestrial neutrinos from unresolved astrophysical sources can probe the existence of high-energy neutrinos. The measurement of a flux $\phi(E)$ of extraterrestrial neutrinos of diffuse origin (diffuse flux) relies on the expectation of a hard spectrum, $d\phi/dE \propto E^{-2}$, associated with astrophysical neutrinos in contrast to the soft spectrum, $d\phi/dE \propto E^{-3.7}$, for atmospheric neutrinos. In other words, the analysis aims to detect an excess of high-energy events over the expected yield of atmospheric neutrino events.

As described previously, the observation of a diffuse flux of gamma rays can provide a theoretical upper limit for the observation of a diffuse flux of cosmic neutrinos. However, our current observations of a diffuse flux of gamma-rays are limited to only a few sectors of the full energy range [Act08]. The EGRET satellite has measured the diffuse flux of gamma-rays in an energy range between 30 MeV and 100 GeV [S+98]:

$$E^2\phi_\gamma(E) = (1.37 \pm 0.06) \times 10^{-6}[\text{GeVcm}^{-2}\text{sr}^{-1}\text{s}^{-1}] \quad (2.12)$$

There are several theoretical models predicting the diffuse neutrino flux from astrophysical sources. Figure 2.7 shows the neutrino spectrum for three of the most favoured theoretical predictions: the Waxman-Bahcall (WB) bound [WB98], a model for pγ interactions in Blazar jets [Man95], and the GRB model by Waxman and Bahcall [WB97].

Among all the theoretical predictions, the WB bound is of highest interest, because it represents a reference threshold which may ultimately be reached by large volume neutrino detectors. The WB method constrains the neutrino flux using the observation of cosmic rays at the energy about 10^{19} eV. The calculation of the upper bound relies on several hypotheses: a) the high-energy cosmic rays are associated with the decay of neutrons escaping the magnetic fields of the sources; b) neutrinos are generated by photo-meson production; c) the sources are transparent to high-energy neutrons; d) the spectral shape of cosmic rays is given by $dN/dE \propto E^{-2}$.

All the predictions have been normalised to one neutrino flavour. The horizontal lines indicate the 90% confidence-level upper limits on the diffuse flux of extraterrestrial muon neutrinos as they have been set by ANTARES (334 data-taking days), AMANDA (807 data-taking days), IceCube-40 (IC-40, 375 data-taking days). Upper limits on extraterrestrial neutrino-induced showers have been set by AMANDA (807 data-taking days), Baikal-NT200 (1038 data-taking days) and IceCube-79 (IC-79, 317 data-taking days). For details of the measurements see [KS07].

The ultimate goal of any search for a diffuse flux of cosmic neutrinos is to either present a sensitive upper limit excluding certain models of cosmic neutrino production or to present an experimentally determined flux of cosmic neutrinos.
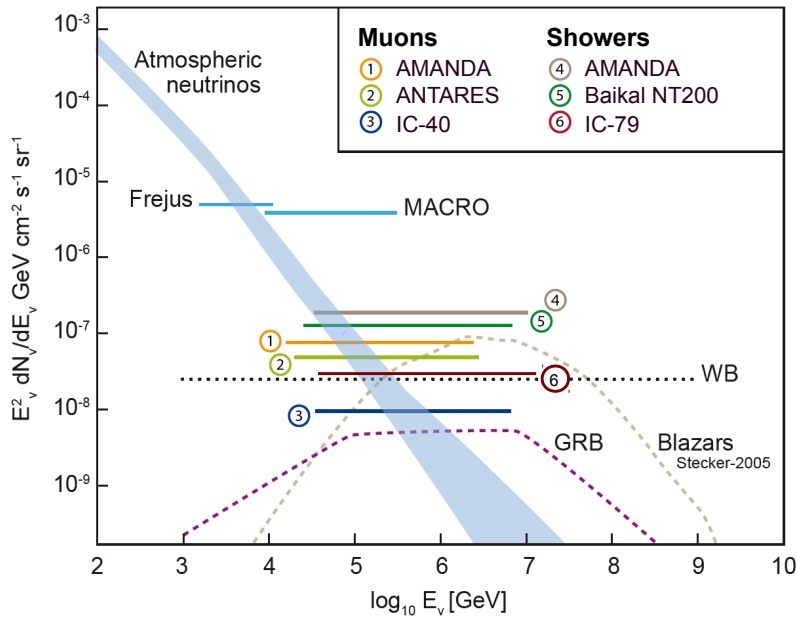
Figure 2.7: The upper limits on the diffuse flux of extraterrestrial neutrinos at 90% confidence level. See text for details. The figure is adapted from [KS07].

The ANTARES Experiment

In seeking wisdom, the first step is silence, the second listening, the third remembering, the fourth practicing, the fifth teaching others.

Ibn Gabirol

This chapter describes the basic principle of underwater neutrino telescopes. The main features of the ANTARES detector are summarised in section 3.2. In section 3.3 we describe the Data-Acquisition System of the experiment. We present some aspects of the calibration of the detector in section 3.4. Finally, in section 3.5, we discuss the optical background observed in the ANTARES detector.

3.1 Neutrino Telescopes

3.1.1 Principle of Measurement

The detection principle of high-energy neutrino telescopes relies on the measurement of Cherenkov light emitted from relativistic charged particles caused by the interaction of neutrinos with matter (ice or water) inside or surrounding the active detection volume. The direction and energy of neutrinos can be inferred from a precise measurement of the arrival time and intensity of the Cherenkov light on a three-dimensional array of PhotoMultiplier Tubes (PMTs). Neutrinos create trajectories of leptons through charged-current interactions, while neutral-current neutrino interactions cause hadronic showers and provide sensitivity to all neutrino flavours.

Muons initiated by interactions of muon neutrinos can travel a considerable distance producing Cherenkov light along the muon trajectory. If the length of the trajectory of a charged particle exceeds the granularity of the detector, the trajectory is called *track*. As described in section 2.4, the interactions of cosmic rays with the Earth's atmosphere induce air showers. High-energy atmospheric muons can penetrate the atmosphere and the overburden water reaching the ANTARES detector (see section 3.2). Therefore, up-going muons as the signatures of neutrinos are selected in order to reject the overwhelming background
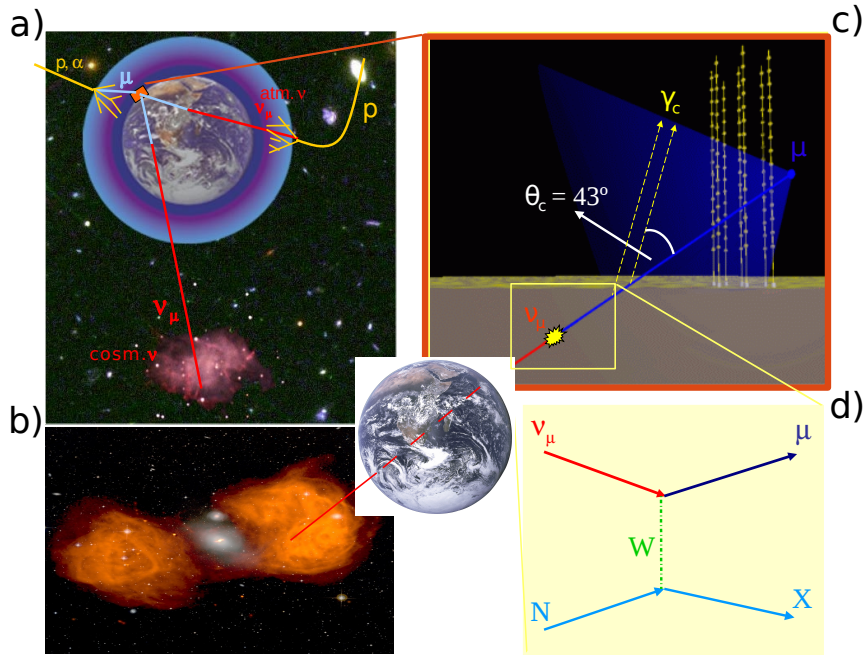
Figure 3.1: Primary detection principle of neutrino telescopes. a) Up-going muons caused by a charged-current interaction of extraterrestrial muon neutrinos, e.g. neutrinos emitted from an AGN (image b), are free from the background of atmospheric muons. c) The neutrino direction can be reconstructed from the cone of Cherenkov light emitted from the neutrino-induced muon passing the 3-dimensional grid of PMTs. d) Feynman diagram of the charged-current interaction of a muon neutrino with a nucleon (N).

of atmospheric muons, exploiting the Earth as a natural filter against all charged particles (see figure 3.1). Most of these neutrinos originate from air showers, i.e. atmospheric neutrinos, forming an irreducible background for the study of astrophysical muon neutrinos. Neutrino telescopes are primarily focused on the reconstruction of muon tracks, aiming at a direct detection of astrophysical sources of cosmic neutrinos.

On the other hand, the electron resulting from a charged current interaction of an electron neutrino as well as hadronic cascades caused by neutral current interactions of all neutrino flavours produce a localised source of Cherenkov light. Such localised events allow a better energy estimation for neutrino-induced showers (see section 5.5) compared with neutrino-induced muons, which eventually leads to a better differentiation between a hard spectrum of astrophysical neutrinos and a soft spectrum of the atmospheric neutrino background. This feature is particularly of interest for the measurement of a diffuse flux of astrophysical neutrinos, which is composed of contributions from many unresolved sources of astrophysical neutrinos.

In this thesis, we will focus on up-going neutrino-induced showers in order to search for a diffuse flux of extraterrestrial neutrinos in the multi-TeV energy range (see chapter 6). In this energy range, the contribution of the background of atmospheric neutrinos is efficiently reduced to allow the study of high-energy extraterrestrial neutrinos.

3.1.2 Cherenkov Radiation

Detection of neutrinos in a neutrino telescope relies on the measurement of *Cherenkov* light induced by the passage of the relativistic charged particles produced by interactions of neutrinos.

A charged particle displaces the electrons in the atoms along its trajectory as it moves through a medium; therefore, the atoms are turned into dipoles along the trajectory of the passing charged particle. In the wake of the charged particle, the atoms revert to their previous orientation. The reorientation of the dipoles results in emission of electromagnetic radiation. For a charged particle travelling at a speed less than the speed of light in the medium c/n (n is the index of refraction), the induced dipoles are symmetrically oriented around the charged particle; therefore, the photon amplitudes interfere destructively. When the speed of the particle exceeds the speed of light in the medium, the symmetry is broken and the photon amplitudes interfere constructively, resulting in a radiation along a so-called *Cherenkov cone*.

The angle θ_C of the Cherenkov cone is defined as follows:

$$\cos\theta_C = \frac{1}{\beta n},$$
(3.1)

where β is the ratio between the speed v of the particle and the speed c of the light in vacuum. For reactions of high-energy neutrinos, $\beta \approx 1$ in water, θ_C is about $42.3°$.

3.2 The ANTARES Detector

ANTARES stands for "Astronomy with a Neutrino Telescope and Abyss environmental RESearch". The ANTARES 12-string configuration was completed in May 2008, making it the largest neutrino telescope operating in the Northern hemisphere [A+11a]. It is located at a depth of approximately 2500 m in the Mediterranean Sea, about 40 km off the coast of Toulon. Currently 8 countries are collaborating in the ANTARES experiment providing 150 members from 30 institutes of particle physics, astronomy and sea science. Figure 3.2 shows the location of ANTARES.

The ANTARES telescope explores the southern sky including the Galactic Centre which locates identified sources of high-energy gamma rays [A+11a]. Complementary to the IceCube detector [HK10], ANTARES extends the reach of neutrino astronomy to the whole Universe. Moreover, being located in the deep sea, the ANTARES infrastructure provides innovative techniques for research in Earth and marine sciences. Since the ANTARES infrastructure maintains a permanent cable connection to shore, a variety of sensors for the measurement of sea parameters, like salinity, oxygen content, flow and temperature, can be installed and surveyed over long periods of times.

Detection Units

As shown in figure 3.3, the ANTARES neutrino telescope consists of 12 detection strings which are cables anchored on the sea bed via a Bottom String Socket (BSS) and kept vertically straight by a buoy located at the top. The BSS houses a dead
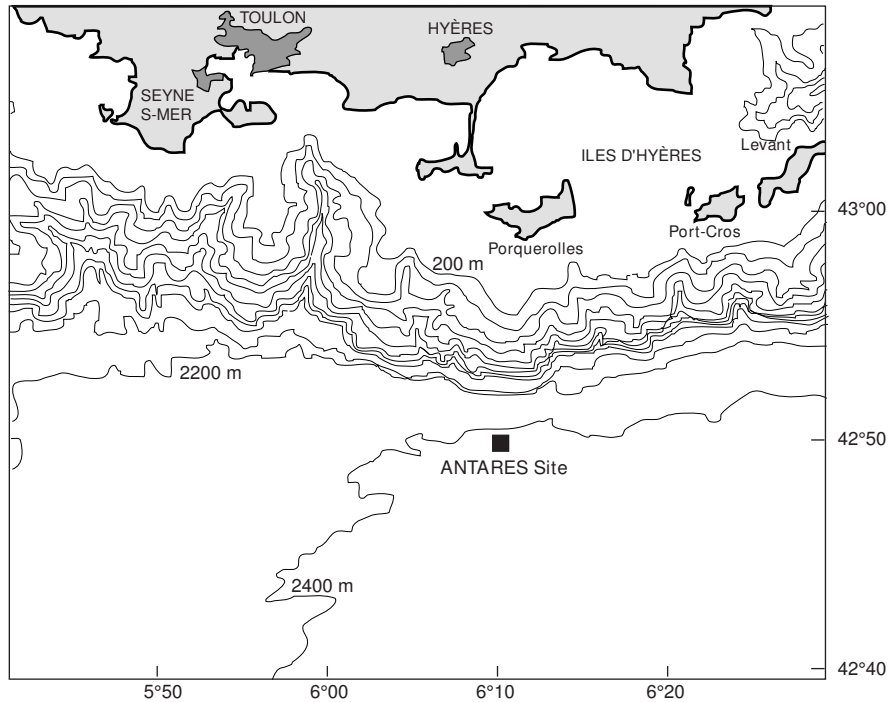
Figure 3.2: Location of the ANTARES neutrino telescope. Figure taken from [Col32].
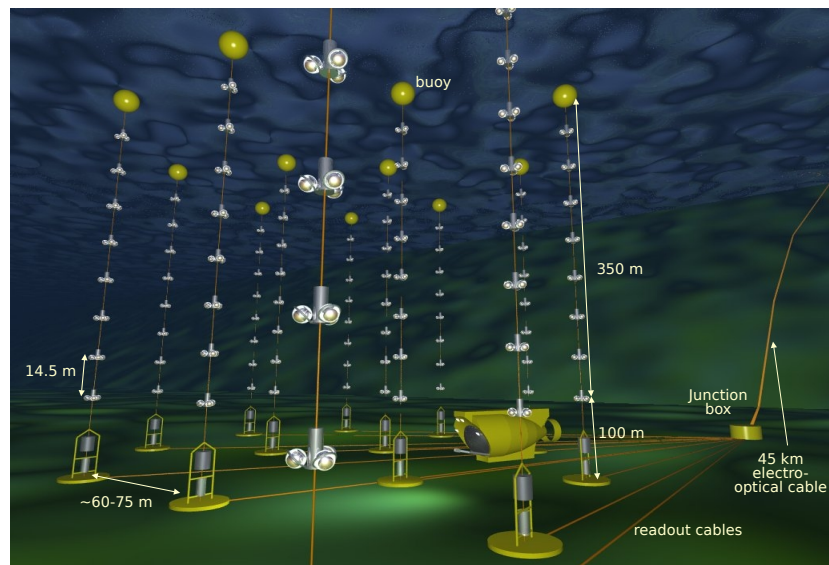
Figure 3.3: Schematic layout of the ANTARES detector. A floor consists of three optical modules, housing one PMT each, together with a local control module. Each string is made up by 25 floors and connected to the junction box. The data are transfered to shore via the electro-optical cable, where they are processed by a computer farm situated in the shore station.

weight and a String Control Module (SCM), as well as an acoustic device which allows the strings to be released when an acoustic command is sent from a ship on the surface. The distance between the strings is about 60-75 m.

20
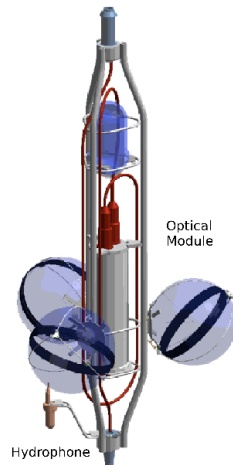
Figure 3.4: Drawing of the ANTARES detection floor showing the three optical modules and the cylindrical container for the electronics. A hydrophone is visible on the left bottom of the picture (see section 3.4).

A string consists of five sectors which are stand-alone systems connected to the Data AcQuisition (DAQ) and the power distribution system. Each sector is a group of five detection floors (storeys), containing a Master Local Control Module (MLCM) which collects the data taken by the floors and sends them to shore. The distance between the adjacent floors is 14.5 meters. A floor consists of a triplet of Optical Modules (OMs) which is depicted in figure 3.4. The OMs are oriented downward at an angle of 45° with respect to the vertical. The OMs are held by a titanium frame which provides the mechanical connection to the string and contains a cylinder housing electronics, which is called the Local Control Module (LCM).

An OM is a pressure resistant glass sphere with a diameter of 43 cm, housing a PMT. The PMT is glued to one of the hemispheres with silicone gel, and the other hemisphere is painted black, providing the electrical connection between the outside and the inside of the OM via a penetrator. Hamamatsu R7081-20 PMTs [Col05] with a diameter of 10 inch and 14 amplification stages are used for the ANTARES detector. The timing resolution of an ANTARES PMT is typically better than 3 ns and is determined by the Transit Time Spread (TTS) of the photo-electrons. In addition to timing resolution, the *dark rate* of the PMT is a key parameter that influences the total performance of the detector. The ANTARES PMTs are selected to have a dark rate below 10 kHz such that the dark rate is negligible compared to the photon background rate. A detailed description of the ANTARES optical module is given in [A+11a].

The full ANTARES detector consists of 885 OMs and 15 acoustic neutrino detection systems (for more details about the acoustic detection see [A+10a]). The ANTARES detection units are connected to a so called Junction Box (JB) which provides the junction to the Main Electro-Optical Cable (MEOC) of 45 km length. The cable transmits the power and the data between the detector and the shore station. The data arrive in a computer farm located at the Shore Station (near Toulon, France), i.e. the location of the ANTARES control room.

In addition to the ANTARES physics instrumentation (the 12 lines), there is

a 13th line (IL07) containing an ensemble of oceanographic sensors dedicated to the measurement of the environmental parameters.

3.3 Data Acquisition System

The main task of the Data Acquisition System is to digitise the analogue signals from the ANTARES PMTs and eventually convert them into a format suitable for the physics data analysis. The data preparation consists of the conversion of the analogue pulses from the PMTs into digital data, data filtering, storage of the filtered data, and archiving the run settings. Figure 3.5 shows a schematic view of the ANTARES DAQ system. This section covers some aspects of the ANTARES DAQ system. More detailed information can be found in [A^{+}07].

3.3.1 Hit Digitisation

During data taking the analogue signals from the ANTARES PMTs are processed by front-end chips, so called ARS (Analogue Ring Sampler) chips, which digitise the time stamp of each PMT signal and the total charge of the pulse. The digitisation is triggered when the signal voltage crosses the *voltage threshold* (typically the equivalent of 0.3 photo-electrons). The voltage threshold is set to eliminate the noise which is mainly due to the dark current in the PMT. In addition to the voltage threshold, the ARS can be programmed with a value for the *integration gate*, i.e. a time interval during which the current on the anode is integrated (typically an interval of 35 ns). The integration gate is set to integrate most of the PMT signal, while limiting the contribution of electronic noise.

A local clock is used to timestamp each triggered PMT signal. Sub-ns precision is achieved by a time-to-voltage converter (TVC) that is used to interpolate between two subsequent clock pulses. The voltage provided by the TVC is digitised with an eight-bit analogue-to-digital converter. The ARS produces *hits* from the combined time and charge information of the PMT signal during the integration time.

The ARS has a dead time of about 200 ns due to the limited transfer speed in the analogue pipelines. To compensate for this dead time, each PMT is read out by two ARS chips, which alternately digitise the analogue signals.

3.3.2 Master Clock System

The reconstruction of neutrino interactions relies on the accurate determination of the arrival times of Cherenkov photons. The key element for this precision is a *master clock* which generates 20 MHz signals on the shore and distributes them through an optical cable network to local clocks in the LCMs. The master clock periodically measures the relative offsets between the local clocks by echoing signals received in the LCMs back to the shore station. The offset is caused by the differences in the optical path lengths.

In order to provide coincidence detection with other astrophysical observations, e.g. from satellites detecting Gamma Ray Bursts or from gravitational-wave detection systems, an absolute timing accuracy of the order of 1 ms is required. This is achieved by linking the master clock to the *Global Positioning System* (GPS).
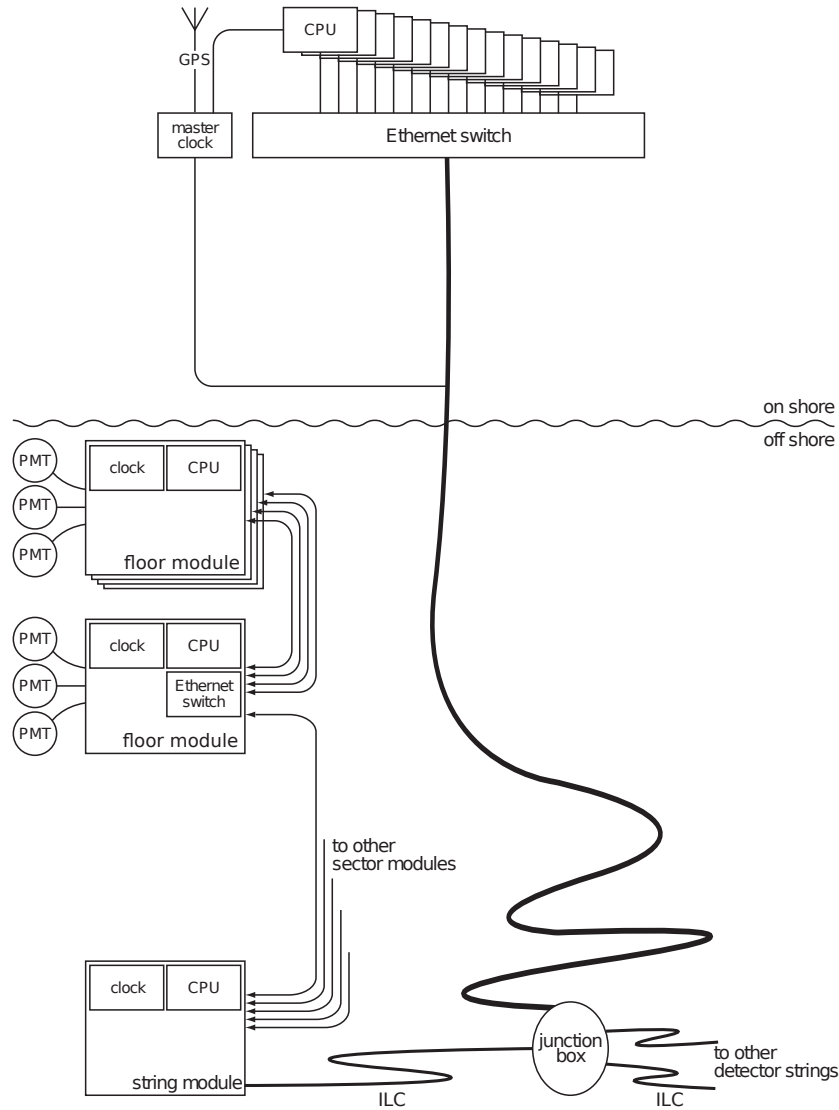
Figure 3.5: Schematic view of the ANTARES DAQ system. Each detection floor (storey) contains a local clock as well as a CPU. The sector modules contain an Ethernet switch in addition. Interconnecting link cables (ILC) provide the connection between the junction box and the detection strings. The junction box is connected to a single cable leading to the on-shore PC farm and the master clock. The figure is adapted from [A⁺07].

3.3.3 Onshore Data Processing

High capacity buffers (64 MB SDRAM) in the LCMs temporarily store the data collected offshore, allowing a de-randomisation of the data flow. The data are packed offshore in hit maps with a predefined time-frame duration of about 100 ms. Subsequently, the data collected for the full detector in the same time frame are sent to the shore station and are processed by a single data filter process in the onshore data processing system.

The onshore data processing system consists of about 50 PCs, each PC handling four data filter processes on its four processor cores. A data filter process uses a fast algorithm to filter physics events from the data (see section 3.3.4).

The algorithm processes each event (with frame duration of 100 ms) in about 500 ms. The filtered data are prepared in ROOT (Rapid Object-Oriented Technology) [BR97] format and copied every night to the computer centre in Lyon [1].

3.3.4   ANTARES Triggers

Various selection criteria, i.e. triggers, are applied to the ANTARES data in order to suppress the contamination of physics data by the optical background (see section 3.5). The ANTARES triggers are a *standard* trigger, a directional trigger, muon triggers based on local coincidences, a minimum-bias trigger for monitoring the data quality, and triggers for multi-messenger search. In this section, we only describe the ANTARES standard trigger, the so-called "3N" trigger which has been used in our data analysis. More detailed information about the ANTARES trigger system can be found in [A+11a].

The standard trigger relies on the general causality relation:

$$\left| t_i - t_j \right| = \frac{n}{c} \cdot r_{ij} \tag{3.2}$$

where $t_i(t_j)$ is the time of the hit, r_{ij} is the distance between the PMT hit i and j, c is the speed of light in vacuum, and n is the index of refraction of the sea water (see figure 3.6). In order to increase the efficiency of the hit selection, a preselection is exploited. The preselection searches for *L1* hits which are defined as a) coinciding hits appearing in a time window of 20 ns between two neighbouring PMTs in the same floor, or b) large hits, i.e. the number of photo-electrons measured by a single PMT has to be larger than three. Then, the standard trigger criteria are defined as either a set of at least five causally related L1 hits or a local cluster of neighbouring L1 hits.

3.4   Calibration

Accurate information on the position and the timing of the ANTARES OMs plays an essential role for the reconstruction of neutrino events. This section briefly describes the calibration techniques which are exploited to determine the timing and position of the ANTARES detector. More detailed information about the detector calibration can be found in [A+11a].

3.4.1   Position Determination

The ANTARES OMs are mounted on flexible strings. Therefore, their positions and orientations can be influenced by the sea current. Figure 3.7 presents the typical x-y displacement of the five hydrophones in the horizontal plane. The acoustic sensors are mounted on 5 sectors of a string (at different heights) and are followed during a period of 6 months. In order to precisely measure the orientation of the ANTARES OMs, each LCM is equipped with a tilt meter and a compass. The positions of the OMs are determined by an acoustic positioning system which exploits hydrophones located at each line sector, recording the acoustic signals from transmitters located at the bottom of each string. The position of the hydrophones can be measured by calculating the propagation times

---

[1]http://cc.in2p3.fr
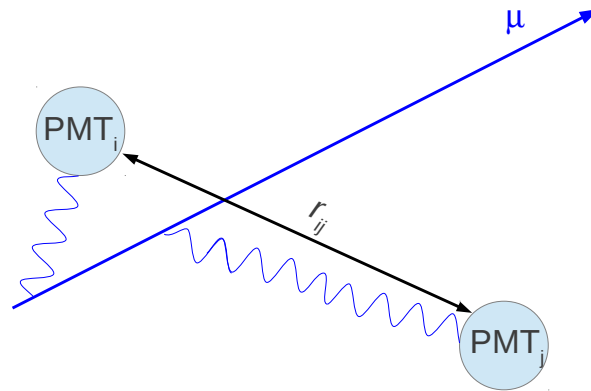
Figure 3.6: Passage of a muon emitting Cherenkov light which is detected by two PMTs i and j.
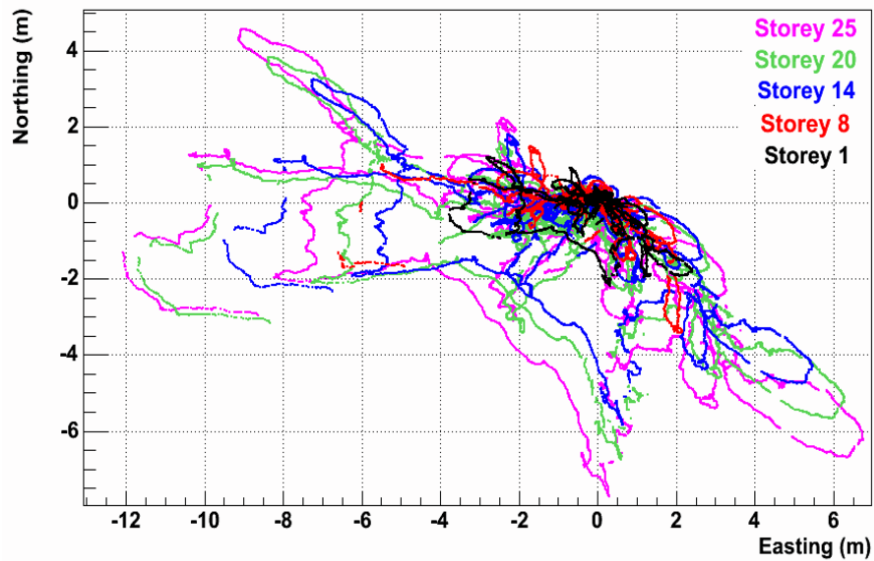
Figure 3.7: Displacements in the horizontal plane of the five storeys (floors) housing positioning hydrophones of a line. The figure is taken from [A$^+$11a].

of the acoustic signals. The shape of each detection string is reconstructed by performing a global χ^2 fit using the information of the combined measurements from the tilt meters, compasses, and the acoustic positioning system. The relative position of each individual OM is then calculated from this fit with an accuracy of a few cm, which translates into a timing accuracy better than 0.5 ns.

3.4.2 Timing Calibration

As mentioned in section 3.3.2, the relative time delays between the local clocks are determined by the master clock. However, the Transit Time Spread (TTS) of the PMTs, which may change during the operation of the detector, cannot be measured using the clock system. LED pulsers mounted inside each OM illuminating the back of the photocathode are exploited to measure the TTS of the PMTs. Since both the LED trigger and the resulting PMT signal are recorded by the ARS, the transit time can be determined directly.

In addition to the clock system and the LED calibration, two different optical beacons, i.e. LED and laser beacon, are used in order to calibrate the whole system. LED beacons are distributed at different levels along each line, so that their light can illuminate all storeys on the neighbouring strings. Two laser beacons are located at the bottom of two central lines and operate in a similar way as the LED beacons. Since the laser beacons provide more intense light, they are mainly used for a cross-check of the timing calibration of the OMs of different lines. The analysis of the resulting hit times provides the overall calibration of the PMTs and the clock system. Precise measurements of position and time of the detector module result in an overall timing accuracy of 1 ns [A$^+$11a].

3.5 Optical Background

The optical background in the deep sea consists of two components: the *baseline* and the *bursts*. Figure 3.8 shows the median rates (in kHz) measured with the ANTARES PMTs on optical modules at two different depths (2037 m and 2386 m), using data collected during 2006 to 2008. The background from the baseline has a typical rate between 60 kHz and 100 kHz. The baseline noise is partially caused by the Cherenkov radiation induced by β-decays of the ^{40}K contained in the salt water, which is estimated to produce a random noise with a constant rate of about 40 kHz per each 10-inch ANTARES PMT. The other contribution is coming from the luminescence produced by living organisms, the so-called bioluminescence which varies with the environmental conditions, e.g. flow and nutrition conditions. The baseline rate mainly causes uncorrelated photon signals in the individual PMTs, so that it can be largely filtered by the ANTARES trigger system (see section 3.3.4).

The bursts are caused by underwater multi-cellular organisms which can emit light. The background of this type is known as occasional extremely high rates up to several MHz, which last for a few seconds. Bursts produce localised and aperiodic hits in the ANTARES detector, so that they cannot affect the whole detector. The fraction of time during which the instantaneous background rate exceeds the baseline rate by at least 20% is referred to as the burst fraction. Similar to the baseline, the burst fraction also varies with time. The burst fraction in ANTARES has a typical value between 0 and 40%.

3.6 ANTARES Event Topologies

A Charged-Current (CC) interaction of neutrinos may cause a leptonic particle as well as a cascade of hadronic particles, exchanging a W-boson. On the other
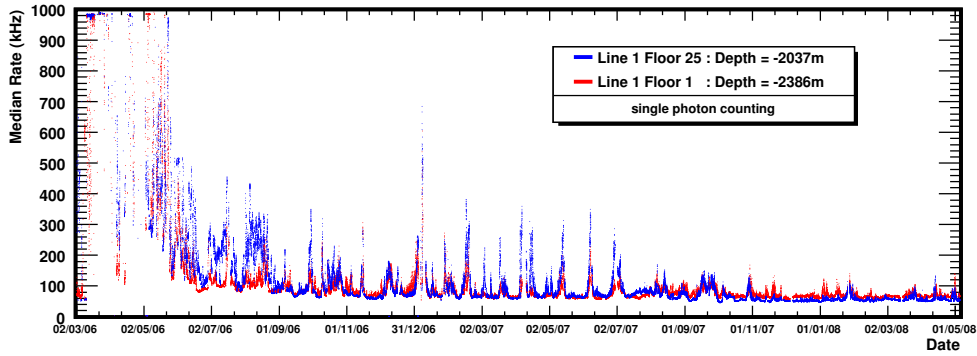
Figure 3.8: Median rates (in kHz) measured on two floors of Line 1 with ANTARES during the period from March 2, 2006 to May 1, 2008.

hand, a Neutral-Current (NC) interaction of neutrinos may cause a cascade of hadronic particles, exchanging a Z-boson. Depending on the neutrino flavour, different interactions of neutrinos may cause different event topologies in the ANTARES detector. In order to reconstruct and identify neutrino interactions, it is important to analyse the different event topologies that may be observed. The ANTARES events can be divided in two main event topologies: Events with a track and events without a track.

3.6.1 Events With a Track

CC interactions of $\nu_\mu(\bar{\nu}_\mu)$ and $\nu_\tau(\bar{\nu}_\tau)$ [2] cause a cascade of short-range hadronic particles, i.e. showers, as well as long trajectories of leptonic particles, i.e. μ and τ tracks, as shown in figure 3.9 (a) and (b), respectively. In case of a CC ν_μ interaction, the length of the muon track can be 2-3 orders of magnitude longer than the length of the hadronic shower part, so that this type of event can be well distinguished if the interaction vertex is located far from the instrumented volume. In a special case, a so-called *escaping muon* event, only the hadronic part of the neutrino interaction is contained inside the instrumented volume, while the muon track leaves the detector without depositing sufficient energy and causing a sufficient number of PMT hits. In this case, most of the observed hits are caused only by the hadronic shower part of the neutrino interaction. This type of event can mimic a neutrino-induced shower without track.

On the other hand, CC interactions of ν_τ can cause totally different event topologies. The sought signature of ν_τ can be a hadronic shower, a track, and a shower. This event topology is called a *double bang event*. The average path length for τ is only in the order of a few meters for τ energy below a few PeV (see [Har06]). Therefore, the average path length of the τ is often suppressed in the ANTARES energy range, so that the two showers cannot be separated and the CC interaction of ν_τ is observed as a single shower-like structure.

---

[2]In this analysis, we assumed that the reactions of neutrinos and anti-neutrinos are indistinguishable. From this moment onward, for simplification, we will use the term neutrino for both neutrino and anti-neutrino.
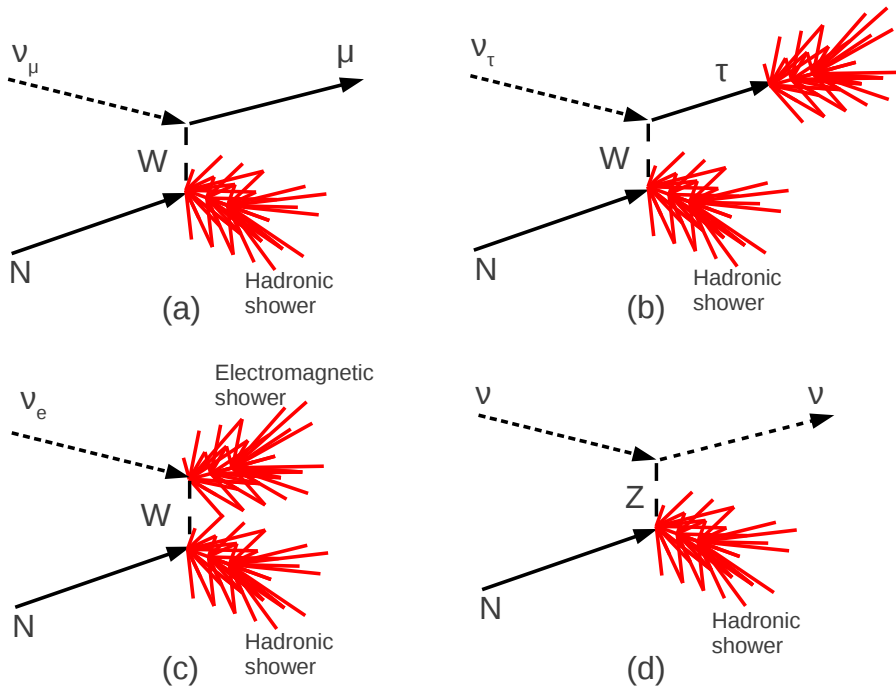
Figure 3.9: Feynman diagrams of neutrino interactions with a nucleon N, corresponding to each event class in ANTARES. The interactions in the upper row refer to event classes with a track and the interactions in the lower row are events without a track. The figure is adapted from [Fol09].

3.6.2   Events Without a Track

A CC interaction of ν_e (see (c) in figure 3.9) causes a cascade of hadronic particles followed by the induced electron. The induced electron undergoes substantial energy loss via bremsstrahlung which can further cause the production of secondary electron-positron pairs. Secondary lepton pairs can re-iterate the whole process until the energy of the secondary leptons drops below the critical energy, i.e. the energy at which the rates of the losses by bremsstrahlung and ionization are equal [Eid04]. Therefore, the induced electron generates an electromagnetic shower. The range of the shower particles is only a few meters in the ANTARES energy range (see section 5.1), so that the trajectories of the shower particles cannot be resolved. Therefore, a ν_e-induced shower is observed as a bright, point-like source of Cherenkov light with an emission volume much smaller than for track events.

NC interactions of all neutrino flavours cause hadronic showers (see (d) in figure 3.9). Even though the light production mechanism for a hadronic shower is different from that for an electromagnetic shower (see section 5.5), due to the spacing between the ANTARES OMs, a hadronic shower cannot be distinguished from an electromagnetic shower.
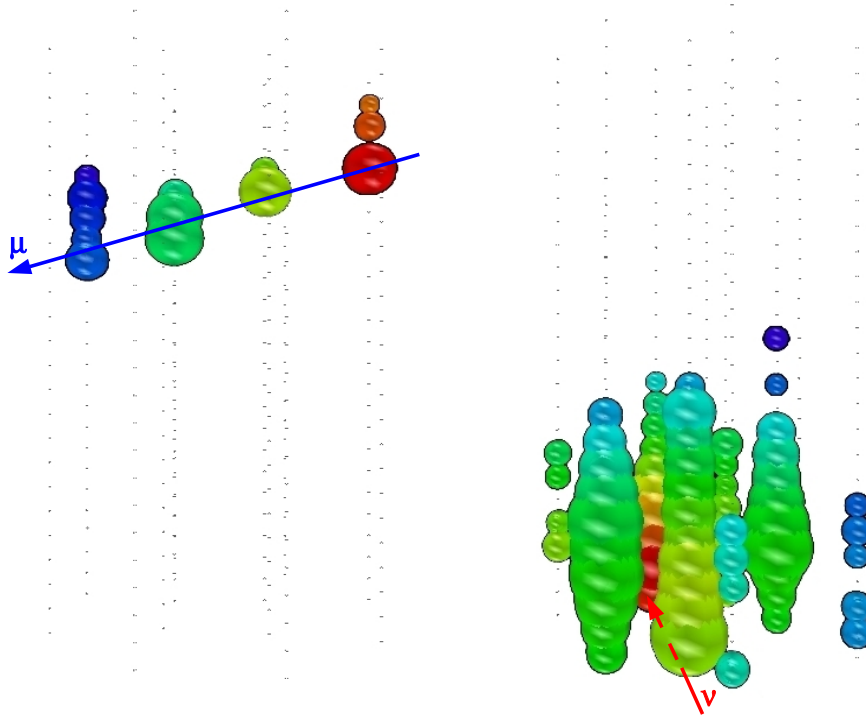
Figure 3.10: Visualisation of Monte-Carlo hit patterns for a down-going muon track (left) and an up-going neutrino-induced shower (right) in ANTARES. The hit OMs are shown as circles with a size proportional to the hit amplitudes. The colour coding presents the photon arrival time (red to dark blue).

3.6.3 Event Signatures

As discussed in the previous sections, the interactions of neutrinos can cause different event topologies. A severe background for neutrino-induced showers is the overwhelming background of down-going atmospheric muon tracks. In order to reject this background, we classify the ANTARES events into two main classes, i.e. track-like and shower-like events. Based on this classification, we will build the tools for reconstruction and selection of neutrino-induced showers in chapters 5 and 6, respectively.

Figure 3.10 compares typical Monte-Carlo simulations for a down-going muon track (left) and an up-going neutrino-induced shower (right). Both events have an energy of about 10 TeV, which are visualised by the SeaTray 3D-event viewer (GLshovel module) [EK]. The hit OMs are shown as circles with a size proportional to the hit amplitudes. A neutrino-induced shower event resembles a bright point-like source of Cherenkov light which is fully contained in the detection volume, whereas a muon emits Cherenkov light along the muon track which is partially contained in the detector.

3.7 Sparking PMTs

In exceptional case, after long operation times, it may happen that the PMT vacuum starts leaking. Such a PMT may suffer from electrostatic discharges between the dynodes and the anode, causing the PMT to spark. Even though it happens
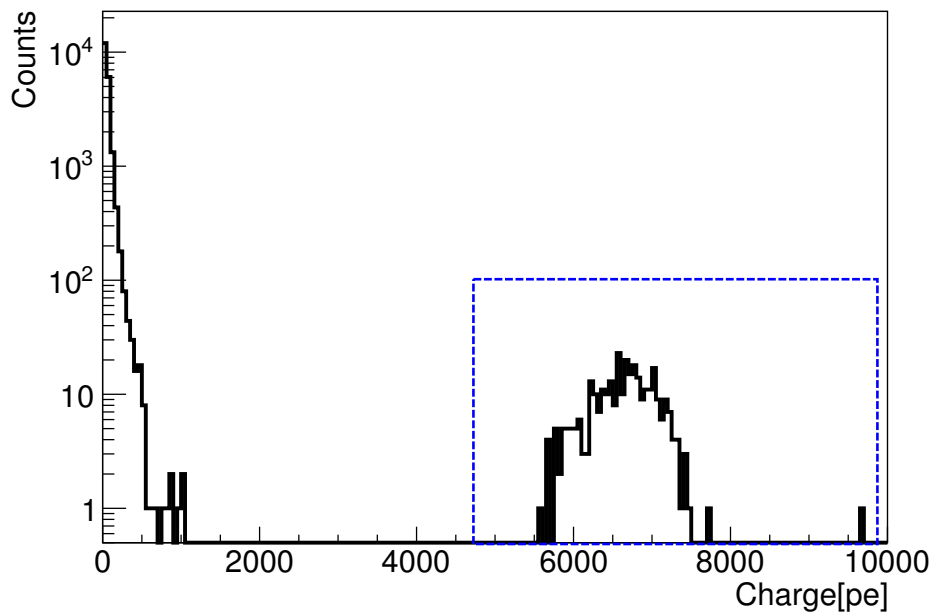
Figure 3.11: Distribution of the total deposited charge per event, i.e. the sum of the amplitudes of all triggered hits in an event (in photo-electrons), for a known sparking run (number 33608). The events with an extremely large charge, marked by the dashed (blue) rectangle, are thought to be sparking events.

rarely in ANTARES, it is known that there are some non-physical events, the so-called *sparking events*, which are likely caused by sparking PMTs [cola]. Such events consist of an anomalous number of hits on specific PMTs, which can be misinterpreted as high-energy neutrino events (see figure 3.11). Although there are some methods to identify the sparking events (see [Pre11, Cor]), it is very important to study the potential of a selection strategy for rejecting such anomalous events. In section 7.1, we will present the rejection potential of our shower-selection strategy for sparking events.

Event Simulation

*When I consider what people generally want in
calculating, I found that it always is a number.*

Muhammad ibn Musa al-Khwarizmi

The shower reconstruction and selection strategy, which will be introduced
in the next chapters, has been tuned with Monte-Carlo (MC) simulated events.
This chapter is devoted to describe the tools which are used to simulate neutrino
interactions, atmospheric muons, and the response of the detector to muons and
neutrinos. In addition, the simulated and experimental data, which have been
used in this study for a detailed analysis, will be summarised in this chapter (see
section 4.5).

In order to optimise the computing time of the event generation, a weighting
factor for each event is assigned. The concept of the event weighting, which will
be frequently used in the context of this work, will be described in section 4.1.

Section 4.2 discusses the aspects of the event generation, which concern the
tools generating the neutrino interactions and atmospheric muons as well as sim-
ulating the Cherenkov light emission from charged particles.

The response of the detector will be covered in section 4.3. In order to in-
crease the reliability of comparing MC simulations to a set of experimental data,
the so called *Run-by-Run* simulation has been developed by the ANTARES collab-
oration (see [G$^+$]). Section 4.4 describes the relevant aspects of the Run-by-Run
simulation.

4.1   Event Weighting

The straightforward simulation of high-energy neutrinos can be very time con-
suming and inefficient considering the steep slope of the involved energy spec-
tra and the large volume of ANTARES. Therefore, one needs to impose a flat
energy spectrum in order to simulate events with sufficient statistics in a wide
energy range covering several decades in intensity. Afterwards, one has to apply
a weighting procedure to scale down the simulated neutrino rate to any other
realistic physics rate, e.g. neutrino-diffuse flux or atmospheric neutrinos. In this
section we explain the event weighting procedure used in ANTARES by calcu-
lating the neutrino event rate for any arbitrary neutrino flux used as input.

The neutrino detection rate R for a differential neutrino flux $\frac{d\Phi(E)}{dE}\left[\frac{1}{\text{GeV cm}^2 \text{ s sr}}\right]$
in an energy interval (E_{min}, E_{max}) in a detector can be given by:

$$R = \int_{E_{min}}^{E_{max}} \frac{d\Phi(E)}{dE} A_{eff} dE,$$
(4.1)

where the factor A_{eff} is the effective area of the detector, i.e. the area in which the detector can potentially detect the interaction of the neutrino. Therefore, the effective area can depend on the following parameters:

- $n(r)$, the number density of the target nucleons per unit volume

- $\sigma(E)$, the total neutrino-nucleon cross section

- P, the total neutrino propagation (through the Earth) and interaction probability. This value is calculated for each neutrino by means of a simulation.

A_{eff} can be written as:

$$A_{eff} = \int P\sigma(E)n(r)r^2 dr d\Omega.$$
(4.2)

Applying equation 4.2, the neutrino detection rate can be rewritten as:

$$R = \iint_{E_{min}}^{E_{max}} \frac{d\Phi(E)}{dE} P\sigma(E)n(r)r^2 dr d\Omega dE.$$
(4.3)

As explained above, in order to efficiently simulate high-energy neutrinos, we impose an arbitrary but fixed neutrino spectrum of the general form:

$$\frac{dN}{dE} = \beta E^{-\gamma},$$
(4.4)

where γ is the spectral index which is conveniently chosen to have a value between 1 to 1.4 [Bai], in order to reduce the computing time. β is a normalisation factor which can be calculated as:

$$\beta = \frac{(1-\gamma)N_{sim}}{(E_{max}^{1-\gamma} - E_{min}^{1-\gamma})},$$
(4.5)

where N_{sim} is the number of simulated neutrinos in a neutrino energy interval (E_{min}, E_{max}). Subsequently the neutrino detection rate can be expressed as:

$$R = \iint_{E_{min}}^{E_{max}} P\sigma(E)n(r)\frac{dE}{dN}\frac{d\Phi(E)}{dE}r^2 dr d\Omega dN.$$
(4.6)

Substituting equation 4.4, the neutrino detection rate for a discrete distribution of the simulated events can be rewritten as:

$$R = \frac{1}{N_{sim}}\sum_{i=1}^{i=N_{sim}} w_i \frac{d\Phi(E)}{dE},$$
(4.7)

where w_i is the generation weight. If the energy bin of the simulation is considered to be as small as it only contains one event per each bin ($\Delta N = 1$), w_i can be defined as:

$$w_i = \frac{(E_{max}^{1-\gamma} - E_{min}^{1-\gamma})}{(1-\gamma)}\int E_i^{\gamma}P_i\sigma(E_i)n(r)r^2 dr d\Omega.$$
(4.8)

Using equation 4.7, one can (re)calculate event-wise the neutrino detection rate for any given neutrino flux.

4.2 Event Simulation

This section describes the simulation chain to generate neutrino and atmospheric muon events, as far as they are used in the context of this study.

4.2.1 Simulation of Neutrino-Induced Showers

The simulation procedure for neutrinos in ANTARES consists of two distinct simulation steps:

- Simulation of the interactions of neutrinos.

- Propagation of the neutrino-induced secondaries and the production of Cherenkov light.

The interaction of all (anti-)neutrino flavours (NC and CC interactions) as well as the propagation of the neutrinos through the Earth are simulated by the *GENHEN* package which is described in detail in [Bai]. Neutrinos start to interact when they enter the *CAN*, a user defined cylindrical object surrounding the ANTARES detector, which will be addressed in section 4.5. *GENHEN* uses the *LEPTO* package to simulate the Deep Inelastic Scattering (DIS) events. *LEPTO* provides the sampling of the differential CC and NC cross sections for the underlying parton-level scattering process in order to obtain the characteristics of the out-going leptons and the struck quarks (a detailed description of *LEPTO* can be found in [I$^+$86]). The fragmentation of the produced partons into the observable hadrons are modelled by the Lund string model, using the *PYTHIA/JETSET* packages (see [Sjo94]).

GENHEN can generate events according to different models of the atmospheric neutrino flux, e.g. the Bartol flux [B$^+$30] and the atmospheric prompt flux, e.g. the Recombination Quark Parton Model (RQPM) [Cosv3]. The output of *GENHEN* consists of the kinematic properties of the primary neutrino, the time and the position of the interaction vertex of the neutrino as well as the energy, position, and direction of the long-lived neutrino-induced secondaries (with a lifetime $\geqslant 10^{-11}$s).

The neutrino-induced secondaries generated by *GENHEN* are sent to the next simulation step, i.e. particle propagation and light generation, which is done by the *GEASIM* package exploiting the General Event-Analysis Tools *GEANT* 3.21 [Cos93]. For each particle a Cherenkov cone is produced. If the Cherenkov cone intersects with ANTARES OMs, hits will be registered by calculating the amplitude and the arrival time of the Cherenkov light. The characteristics of the OMs, e.g. angular efficiency, transparency, and the quantum efficiency of the phototubes, are taken into account. The attenuation of light due to the light absorption in sea water is considered, however, the attenuation due to the scattering of photons is neglected. The systematic uncertainty due to the light scattering will be discussed in section 6.6.

The current version of *GEASIM* which has been used for the shower simulation, i.e. *GEASIM v4r12*, generates events in an energy range of $10^2 - 10^9$ GeV. Since *GEASIM* considers all the physics processes which can occur during the passage of the secondaries through the medium, the computing time increases with the energy of the particle. The simulation of all the processes can be very

time consuming, in particular when a high-energy neutrino induces an electron in a CC ν_e interaction. The electron is responsible for a large fraction of electromagnetic cascades which have to be traced down to the Cherenkov level. In order to minimise the computing time for ν_e events, the whole shower is approximated by only the neutrino-induced electron. This approximation, the so called One Particle Approximation (OPA), is considered when the energy of the incident neutrino is higher than 10^5 GeV.

The output of *GEASIM* includes the positions of the hit OMs with the information of the amplitude and the arrival time of the hit. This information is added to the information provided by *GENHEN*. After these two steps, the processed events will be fed to the detector simulation tools, in which the response of the detection units will be simulated (see section 4.3) and the optical noise will be added.

4.2.2   Simulation of Atmospheric Muons

Downward going atmospheric muons, caused by the interactions of cosmic rays with the Earth's atmosphere, can be considered the most serious background for any physics analysis of data from neutrino telescopes, if the muons are wrongly reconstructed as upward going events. However, atmospheric muons can be exploited to calibrate the detector, e.g. by real-time monitoring of the detector status and the time variation of the efficiencies of the detector, or to study the pointing accuracy of the detector e.g. by a measurement of the disappearance of the down-going muons caused by the shadow of the moon [Opp]. All together, the study and accurate simulation of atmospheric muons is essential in order to correctly interpret the obtained neutrino data.

The spectrum of atmospheric muons can be accurately reproduced by the full MC simulation of the air showers, caused by the interaction of cosmic rays with atmospheric nuclei. However, such a full simulation requires a large amount of computing time for a detector with cubic-kilometre scale. Therefore, the ANTARES collaboration developed the *MUPAGE* package, a fast MC algorithm, to generate underwater/ice atmospheric muons up to a depth of 5.0 km (for more detail see [C+08]). *MUPAGE* is based on a parametrisation of the flux of atmospheric muons, derived from full simulations of the air showers caused by the interaction of cosmic rays with the Earth's atmosphere. Like *GENHEN*, *MUPAGE* defines an imaginary *CAN* around the active detector volume and reports only those events which develop inside the *CAN*. The output of the code includes the kinematic information about muons as well as the energy, direction and the multiplicity of muons. The livetime of the corresponding ANTARES data taking is calculated from the number of muons simulated by *MUPAGE*, thus in order to obtain a more realistic simulation, *MUPAGE* is parametrised according to the run livetime, which will be discussed in more detail in section 4.4.

4.3   Detector Simulation

The response of the OM to Cherenkov photons can be precisely simulated by taking into account the detailed information on the quantum efficiency, the (relative) gain, angular acceptance, effective area and after-pulse rates of the ANTARES

PMTs. All these effects are dependent on the wavelength and can also be functions of the measurement time.

The events simulated by the previously mentioned methods, i.e. *MUPAGE* and *GEASIM*, are sent to the last step of the ANTARES simulation chain, where the response of the detector to neutrino-induced signals and the optical background are simulated. This last step of the ANTARES simulation chain is called *TriggerEfficiency* [dJ]. The *TriggerEfficiency* module reads the status of the detector from the data-taking summary which is automatically stored during the experimental data taking. Previously mentioned parameters of PMTs such as the quantum efficiencies, the probability of the after-pulses, and angular acceptance, are applied in the simulation. The charge and time calibration parameters, i.e. TVC and AVC, are taken from the calibration runs, in order to compute the time interpolation and the timestamping. The *TriggerEfficiency* can also add trigger selections to the simulated data in order to have the simulated results resemble the experimental data as close as possible.

4.4 Run-by-Run Event Simulation

The conditions of the underwater environmental activities and the status of the detector can vary on a moderate time scale during experimental data-taking periods. The typical entity, for which the condition can be specified consistently, is a data-taking *run* covering about 2-3 hours depending on the background rates and selected trigger conditions. The Run-by-Run variations can have some significant consequences for the quality of the data. In order to simulate the events in a more realistic way, one has to include the status of the detector as well as the realistic condition of the optical background in every run. Figure 4.1 shows examples of typical ANTARES run-evaluation spectra for a data-taking duration of about one week. The ANTARES collaboration has introduced the *Run-by-Run* simulation project in order to impose the realistic conditions of data taking onto the event simulation [G+]. The parameters included in the *Run-by-Run* simulation are: Displacement of the detector units due to Sea current, number of active OMs, mean rate of the active OMs, and run duration.

The *Run-by-Run* simulation exploits the previously mentioned simulation tools *GENHEN*, *GEASIM* and *MUPAGE*, to simulate physics events and then it applies *TriggerEfficiency*, including the above discussed data-taking parameters, to simulate the detector response as close as possible to reality.

4.5 Data Samples

We have prepared a number of data samples in order to test the performance of the reconstruction and classification algorithms. The data samples are described as follows.

4.5.1 Sample 1

This sample has been generated to test the performance of the shower reconstruction strategy. The sample contains NC interactions of muon neutrinos. In order to obtain reproducible performance plots of the shower reconstruction algorithms,
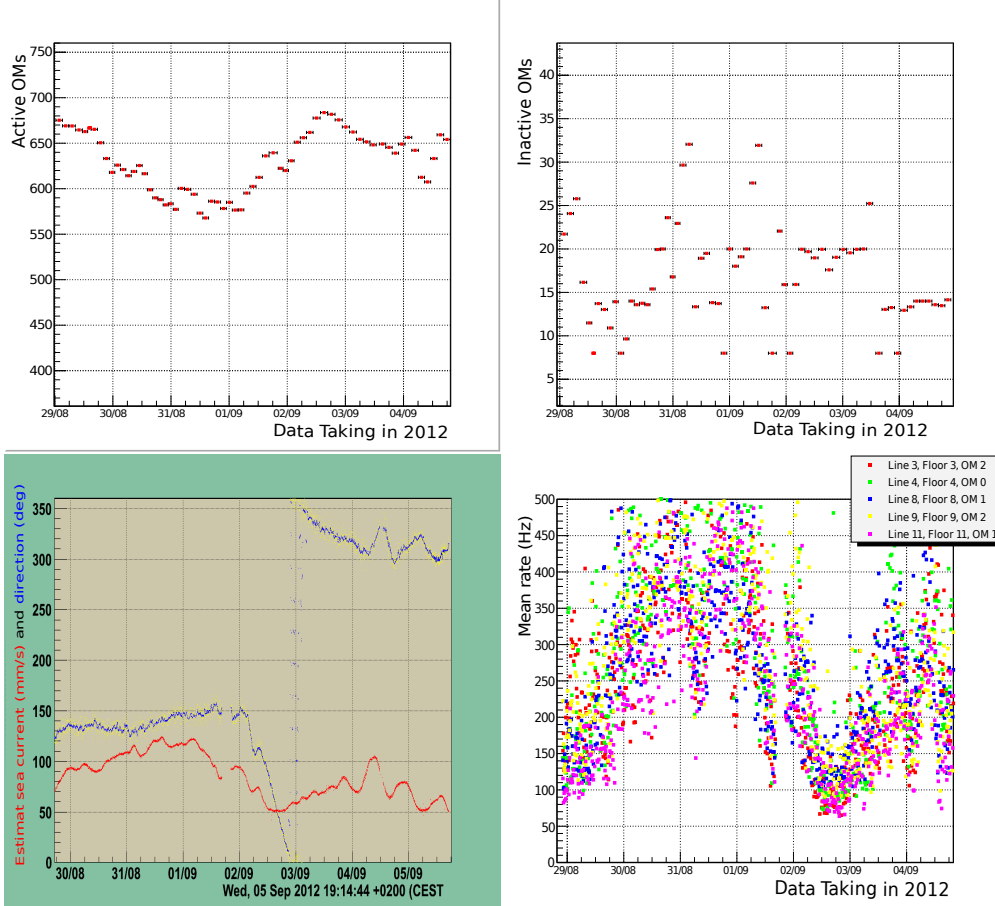
Figure 4.1: Typical ANTARES run statistics in a period of approximately one week in August-September 2012. Shown are the number of active OMs (top left), fraction of inactive OMs (top right), under-water sea current and direction (bottom left) and mean rates (bottom right).

no dynamic variations in the detector status have been added to this simulation sample yet. A random white noise of 60 kHz per OM has been added in order to reproduce the ANTARES typical mean rate. The simulation *CAN* is about the size of the instrumented volume of the ANTARES detector plus a shell with radius of the light attenuation length in sea water (55 m). The sample 1 is specified in table 4.1.

4.5.2 Sample 2

This sample contains the CC interactions of electron neutrinos. Since the dynamic variations of the detector, e.g. quantum efficiency of the OMs or number of inactive OMs, can have a significant influence on the total charge registered by the detector and, consequently, on the parametrisation applied in the shower energy-reconstruction algorithm (see section 5.5), the *TriggerEfficiency* module was applied in this simulated data sample. Compared to NC showers, a larger *CAN* was applied in this simulation, i.e. the size of the instrumented volume of the ANTARES detector plus a shell with a radius 3 times the light-attenuation length in sea water. More details about the simulation procedure are provided in [Bon].

Neutrino interaction	NC ν_μ
Spectral index	E^{-2}
Neutrino energy range	$10^2 - 10^7$ GeV
Direction of incidence	4π isotropically
CAN size	ANTARES detector + shell of radius 55 m
Optical background	60 kHz white noise
Number of generated events	67783

Table 4.1: Characteristic of simulated data sample 1. This sample has been mainly used to test the performance of the shower-reconstruction algorithms (see chapter 5).

The reason for the larger *CAN* is that the leptonic contribution of the neutrino-induced showers can elongate the showers. In order to minimise the computation time, the one-particle approximation was applied for neutrinos with an energy higher than 10^5 GeV (see section 4.2.1). Table 4.2 summarises the specifications of the sample 2.

Neutrino interaction	CC ν_e
Spectral index	$E^{-1.1}$
Neutrino energy range	$10^2 - 10^7$ GeV
Direction of incidence	4π isotropically
CAN size	ANTARES detector + a shell of radius 165 m
Optical background	*TriggerEfficiency* simulation
Number of generated events	10^4 per each energy decade
One-particle approximation	activated for neutrinos with energy $> 10^5$ GeV

Table 4.2: Characteristic of simulated data sample 2. This sample has been used to test the performance of the shower energy-reconstruction algorithm (see section 5.5).

4.5.3 Sample 3

In order to train and test our classifier algorithms (see sections 6.3.1 and 6.3.2), we have used Run-by-Run simulations generated corresponding to experimental data taken in the period of 2008-2010, with a total livetime of about 52 days (see section 6.3). For each experimental run, there are the corresponding *Run-by-Run* simulated atmospheric muon background available as well as the simulated neutrino events. Half of the data has been used for training and the other half for testing the algorithms. The specifications of the data sample can be found in table 4.3.

	Simulation of	simulation of
Type of events	CC $\nu_e(\bar{\nu}_e)$ + NC $\nu_e(\bar{\nu}_e)$ + NC ν_μ + CC ν_μ	Atmospheric muons
Simulation tools	*GENHEN + GEASIM* *+ Run-by-Run*	*MUPAGE* *+ Run-by-Run*
Run numbers ending with 0	31070-49000	31070-49000
Energy range	$10^2 - 10^8$ GeV	$10^2 - 10^8$ GeV
# reconstructed events	68884	3443508
One-particle approximation	energy $> 5 \times 10^4$ GeV	-
Livetime	-	52 days

Table 4.3: Characteristic of data sample 3. This sample has been used to train and test the multivariate classifiers introduced in section 6.3.

4.5.4 Sample 4

This sample consists of the whole Run-by-Run MC samples of the atmospheric muons simulated for the data taken in 2008-2010 corresponding to a livetime of 656 days [1]. The sample is exploited to determine the values of the signal-background discriminating cuts. In order to perform data-MC comparisons, 5% of experimental data has been selected. In order to reduce the statistical bias in choosing the runs, the experimental data with the run numbers ending with 0 (approximately one run per day) have been used [2]. Table 4.4 summarises the

---

[1] Actually, the full set of runs was simulated by three times less statistics. Therefore, we scaled up each MC atmospheric muon event by a factor of three.

[2] We only chose the experimental runs for which the corresponding *Run-by-Run* simulations were available.

sample 4.

	simulation of	Experimental data
Type of events	Atmospheric muons	
Simulation tools	*MUPAGE* *+ Run-by-Run*	-
Run numbers	31070-54250	34050-49000 (ending with 0)
Energy range	$10^2 - 10^8$ GeV	-
# reconstructed events	87239387	4394535
Livetime	656 days	26 days

Table 4.4: Characteristic of data sample 4. This sample has been used for optimisation of shower selection criteria as well as to perform the data-MC comparison.
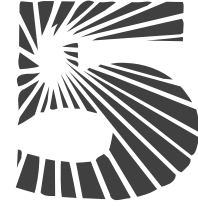
Chapter

Reconstruction

If everyone would be able to correctly benefit in the use of their own talents, the world would become the promised paradise that everyone dreamed of.

Zakariya Razi

This chapter introduces the reconstruction chain that we have developed to estimate the individual parameters of neutrino-induced showers, such as the interaction time and vertex, direction, and energy. The reconstruction chain exploits the causality relation between the Cherenkov light emitted from the shower particles and the arrival times and amplitudes of the hits. In order to maximise the accuracy of a reconstruction algorithm, one needs to reduce the contribution of the optical background in the hit maps to the highest extent. For that purpose, we have constructed a reconstruction chain based on a sequence of fitting and selecting algorithms.

Section 5.1 presents an algorithm for the reconstruction of the shower vertex. The algorithm consists of two consecutive procedures. First, it estimates the mean space-time position of the showers, which provides the starting points for the next fitting procedure, the M-Estimator method.

In section 5.2 the shower vertex parameters which are estimated in the previous stage, are exploited to select the shower hits and discriminate them from the optical background hits.

Section 5.4 addresses the *Light Direction* method that we have developed to reconstruct the direction of events. Primarily, the method is meant to discriminate up-going showers from down-going atmospheric muon background. This aim requires that the method is efficient for the direction reconstruction of both showers and muons.

In section 5.5 an algorithm to reconstruct the shower energy will be introduced. The algorithm requires the shower vertex parameters which are achieved at the vertex reconstruction level.

5.1   Shower Vertex Reconstruction

When a neutrino induces hadronic or leptonic cascades of charged particles, those particles with the velocities exceeding the phase velocity of light, V_p, can emit Cherenkov light as they pass through the water. The phase velocity of light at the ANTARES site [A+11a] is given by:

| Mean | 2.5 |
| RMS | 1.9 |
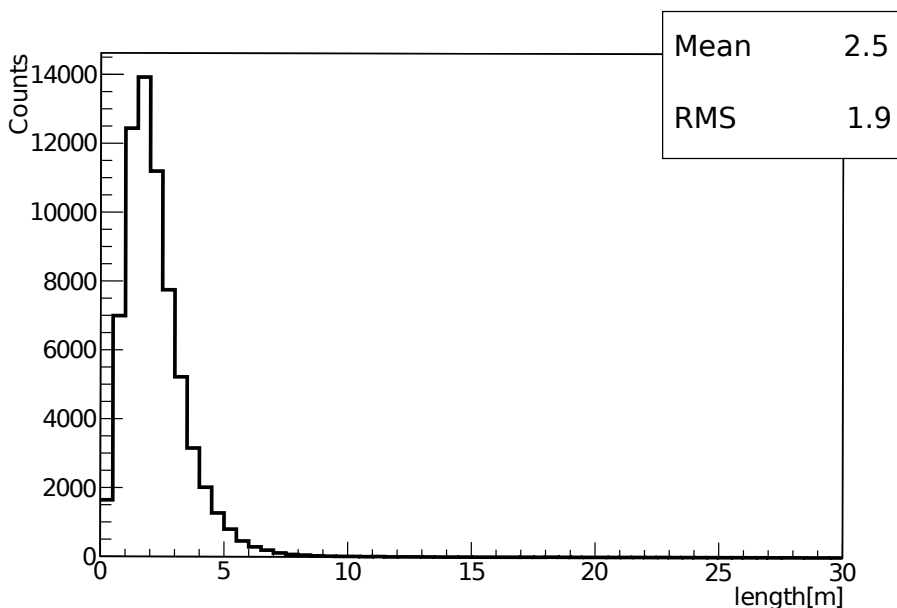
Figure 5.1: Distribution of the length of shower-particle trajectories with a neutrino flux spectrum proportional to E^{-2}.

$$V_p = \frac{c}{n} = 0.74c, \tag{5.1}$$

where c is the speed of light and n is the index of refraction in sea water. The process of the shower light production can effectively be interpreted as the sum of the contributions of the Cherenkov light continuously radiated from many short trajectories of charged particles. Figure 5.1 shows the distribution of the length of the NC shower trajectories, simulated in the energy range of 100 GeV – 10 PeV. The distribution has a mean of about 2.5 m, which indicates that showers can typically have an average length of a few meters in the ANTARES detector volume. Therefore, in order to simplify the shower vertex reconstruction, one can approximate a shower as a point-like object as compared to the granularity of the detector. In the context of this analysis, we approximated showers as point-like objects. Later, in section 5.1.2, we will discuss the effect of such an approximation on the accuracy of the shower vertex reconstruction.

The shower vertex reconstruction algorithm consists of two steps:

The mean space-time estimation: This part of the algorithm estimates the mean space-time position of the shower vertex by analytically solving an over-constrained set of equations describing the shower structure (see section 5.1.1).

The M-Estimator: Given the starting points from the previous step, the M-Estimator minimizes the distance between the measured hit times and the expected arrival time of photons from a point-like source of light (see section 5.1.2).

5.1.1 Shower Mean Space-Time Estimation

If one adopts the hypothesis that a shower is a perfect point source of light and also PMTs measure the light arrival time perfectly, the measured hit time must be equal to the photon travel time from the shower vertex. Figure 5.2 illustrates
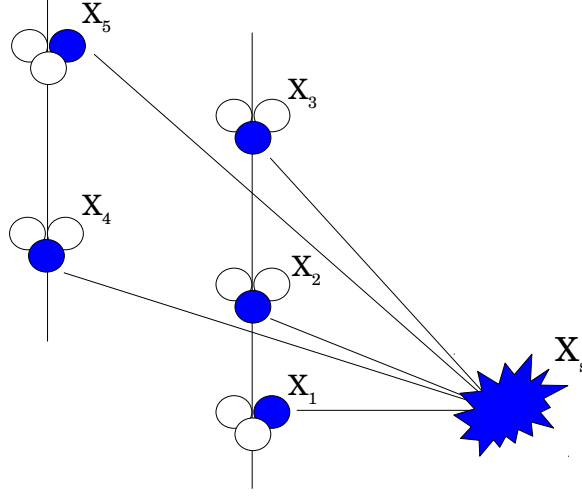
Figure 5.2: Sketch of a hypothetical point-like shower, interacting at a space-time position $\mathbf{X_s}$. The light emitted from the shower is hitting 5 PMTs (filled circles) located at space-time coordinates $\mathbf{X_i}$ ($1 \leqslant i \leqslant 5$).

the detection of a hypothetical point-like shower which interacts at a space-time position $\mathbf{X_s} = \begin{bmatrix} \vec{r}_s & (ic/n)t_s \end{bmatrix}$. The shower light is detected by $N = 5$ PMTs (filled circles) with the known space-time coordinates $\mathbf{X_i} = \begin{bmatrix} \vec{r}_i \\ (ic/n)t_i \end{bmatrix}$ ($i = 1, ..., N$).

ΔT, the time difference between t_i and the expected travel time ($\frac{n}{c}|\vec{r}_s - \vec{r}_i| + t_s$) of light from the shower vertex, is equal to zero for a perfectly point-like shower.

$$\Delta T = \frac{n}{c}|\vec{r}_s - \vec{r}_i| + (t_s - t_i) = 0, \quad 1 \leqslant i \leqslant N \tag{5.2}$$

where t_s is the interaction time. Equation 5.2 is a set of N equations. Pairwise subtraction of the set of equations cancels out the quadratic components of $\mathbf{X_s}$, and $(N-1)$ linear equations of the following form remain [Har06]:

$$2\mathbf{X_s} \cdot (\mathbf{X_{i+1}} - \mathbf{X_i}) = r_{i+1}^2 - r_i^2. \tag{5.3}$$

Therefore, the shower space-time position, $|\mathbf{X_s}|$, can be given by:

$$|\mathbf{X_s}| = b \cdot \frac{1}{2} \begin{bmatrix} \vec{r}_{i+1} - \vec{r}_i \\ \frac{ic}{n}(t_{i+1} - t_i) \end{bmatrix}^{-1} = b \cdot A^{-1}, \tag{5.4}$$

where A is a $(N-1) \times 2$ matrix and b is a vector with the components:

$$b_i = r_{i+1}^2 - r_i^2 - \frac{c^2}{n^2}(t_{i+1}^2 - t_i^2), \quad 1 \leqslant i \leqslant (N-1) \tag{5.5}$$

Equation 5.4 is a set of $(N-1)$ equations with four unknown shower parameters: (x_s, y_s, z_s, t_s). Therefore, in order to solve the equations unambiguously and, in addition, to constrain the shower parameters in 3 dimensions, at least $N = 5$ hits distributed in two detection strings are required. We can define R, the residual parameter, to judge how well an event looks like a point-like object:

$$R = \sqrt{(\mathbf{X_s} - b \cdot A^{-1}) \cdot (\mathbf{X_s} - b \cdot A^{-1})^T} \qquad (5.6)$$

Later, in chapter 6, we will use R as one of the discriminating variables to classify shower and muon-track events.

Figure 5.3 demonstrates the performance of the shower mean space-time estimator (*SMST-Estimator*). Shown are the differences between the thrown MC space-time positions of the shower and the reconstructed space-time position. The MC sample 1 (see section 4.5) was used to generate the performance plots. The method can reasonably reconstruct the shower vertex, since the distributions are peaking around zero. The reason why the shower vertex is better reconstructed in the Z-axis compared with the other two axes is that the density of the detector units is larger in the Z-axis (see section 3.2). The long tails in the distributions, which continue up to several hundred meters, deteriorate the resolution of the vertex reconstruction. One of the main reasons for such long tails in the distributions is the contributions of outliers, caused by the deviation from assumptions, e.g. late hits from the shower development or uncertainties in the measurements of the space-time positions of the hit. Moreover, the offset in the interaction-time reconstruction can be due to the statistical effects of shower-development. This effect will be investigated and discussed in section 5.3. In the next section, we will exploit a robust algorithm, insensitive to outliers, to improve the resolution of the shower vertex reconstruction.

5.1.2 M-Estimator

In this section we apply a robust estimator, the so called M-Estimator (see section 15.7 of [P^{+}07]), for the shower vertex reconstruction. M-Estimators do not necessarily relate to a probability density function. Therefore, they are not fully parametric as likelihood or Bayesian approaches. A robust M-Estimator reduces the effect of outliers by selecting a proper minimizing function, $\rho(x_i)$. x_i is the distance between the ith observed and the expected value which, in the context of this analysis, can be ΔT, introduced in equation 5.2. When the assumptions are met approximately, a robust M-Estimator has a reasonable efficiency in finding the global minimum. Practically, a robust M-Estimator should satisfy the following requirements:

- The influence of large errors should be bounded. This property cuts off the effect of large fluctuations.

- The minimizing function ρ is convex in the estimating parameters. This property, of course, is necessary to ensure a unique minimum for the M-Estimator.

In this analysis, we chose a so called $L_1 - L_2$ M-estimator of the following form [Zha97]:
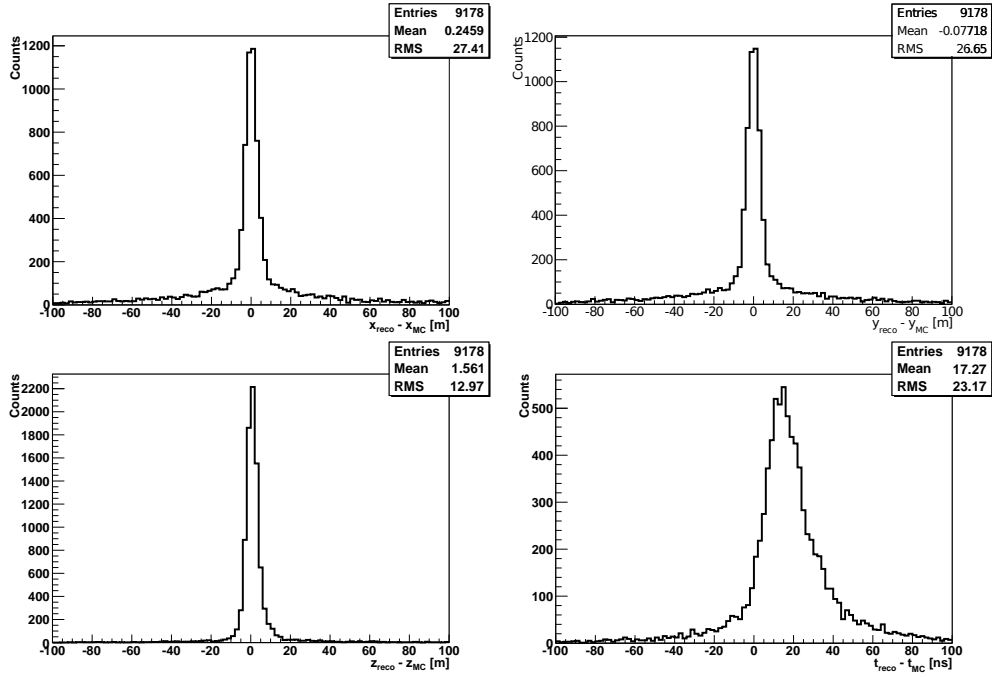
Figure 5.3: Performance of the SMST-Estimator for a MC sample of NC muon-neutrino-induced showers. Shown are the differences of reconstructed and MC-thrown space and time coordinates.

$$M = 2 \times \sqrt{1 + \frac{\Delta T^2}{2\sigma^2}} - 2, \tag{5.7}$$

where σ is the ANTARES error of time measurements which is 1 ns [A$^+$11a] (see section 3.4). The applied M-Estimator behaves linearly in ΔT (see equation 5.2) for large values of ΔT, such that it cuts off the influences of large fluctuations, and quadratic for small values of ΔT, i.e. it is a convex function. Figure 5.4 shows the distribution of the space-time reconstruction residuals of the applied M-Estimator. If one compares the spread of the distributions of the shower parameters reconstructed by the M-Estimator and by the SMST-Estimator, one can notice that the resolution is improved by a factor of about 1.5. However, there is another major source of statistical inaccuracy, i.e. the contamination of hits caused by the activities of the bioluminescence of living creatures and by the decay of ^{40}K, which has not been suppressed yet. In the next section, the shower vertex reconstructed by the M-Estimator will be used to look back into the hit maps of the events in order to only select the hits which are causality related to the vertex.

5.2 Shower Hit Selection

ANTARES exploits a number of different trigger conditions in order to reduce the contamination of the optical-noise hits as well as to enhance the efficiency of the signal-hit selection. In the previous section, we fed the shower vertex reconstruction algorithms (SMST-Estimator and the M-Estimator) with the 3N trigger hits. The ANTARES triggers are mainly optimised for the selection of hits caused
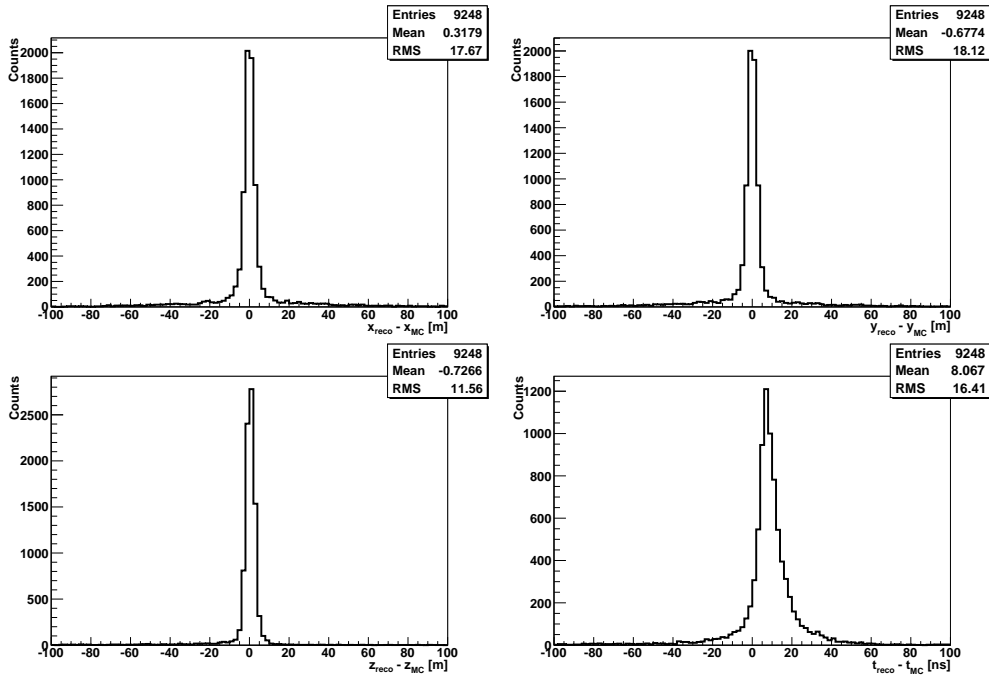
45

Figure 5.4: Performance of the M-Estimator on a MC sample of NC muon-neutrino-induced showers.

by muon tracks. In order to increase the quality of the shower reconstruction as well as to reduce the contamination of the optical noise in the hit maps, in this section we abandon the ANTARES trigger hit selection and apply a new method, *shower-hit selector*, to select the hits which are connected by causality to the shower interaction space-time position.

Figure 5.5 presents, as an example, the distribution of Δt, the time residual, i. e. the mean difference (per event) between the measured hit time and the expected photon arrival time from the reconstructed shower vertex, estimated by the M-Estimator (see section 5.1.2), for CC electron-neutrino-induced showers in the neutrino energy range of $10^3 - 10^4$ GeV. The contributions from the noise-less showers (dashed (red) line), from optical noise (filled (blue) region), and from all hits, i.e. the sum of shower hits and optical-noise hits (solid (black) line) are shown separately. As expected, the time-residual distribution of shower hits is peaking at about zero. However, the distribution is smeared and slightly shifted because of different physical and instrumental processes such as shower development, light scattering, or dispersion of TTS of the PMTs. We observe that the contamination by the optical noise adds a long tail in the large time residuals. To reduce the noise contamination to an acceptable level, we set a time gate Δt in order to achieve a Figure Of Merit (FOM), i.e. *purity $\times$ efficiency*, better than 0.55 in the overall sensitive energy range. This results in an optimal time gate of $-10 < \Delta t < 14$ ns for the shower hit selection.

Figure 5.6 shows efficiency and purity of the hit selection (filled (black) circles) and 3N trigger (filled (red) stars) as function of the neutrino energy in the energy range of $10^2 - 10^8$ GeV. The terms efficiency and purity are defined as the ratio of the selected shower hits over all shower hits and selected shower hits over all selected hits, respectively.
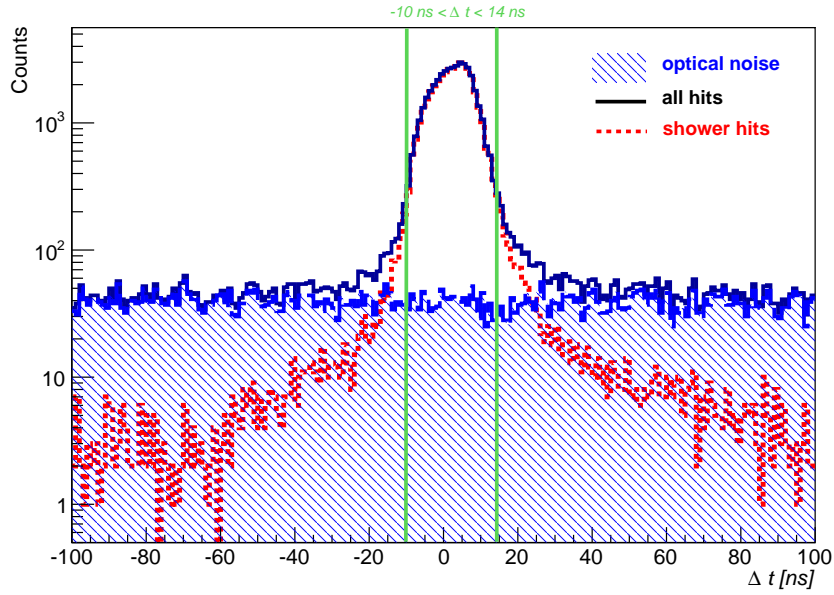
Figure 5.5: Distribution of Δt, the difference between the measured and expected photon arrival time from the reconstructed shower vertex. Contributions of photons from noise-less showers (dashed (red) line) and from the optical noise (filled (blue) area) are shown separately. The vertical (green) lines indicate the imposed time window for the shower hit selection.
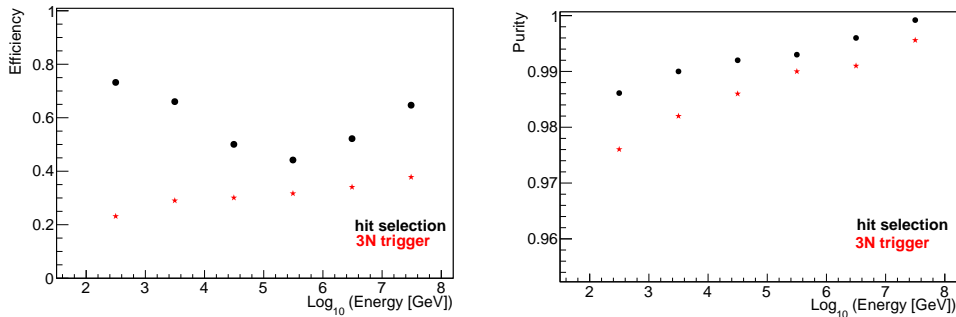
Figure 5.6: Efficiency (left) and purity (right) of the shower hit selection (filled (black) circles) and 3N trigger (filled (red) stars) as function of neutrino energy.

The *shower-hit selector* increases the hit-selection efficiency by a factor of about 1.8 compared to that obtained with the 3N trigger, which was applied for the pre-shower vertex reconstruction, introduced in sections 5.1.1 and 5.1.2.

5.3 Final Shower-Vertex Reconstruction

In order to improve the quality of the shower vertex reconstruction, we combine the hit selection and the vertex reconstruction as follows:

1. **Pre-hit selection**: The first hit selection is obtained by the ANTARES 3N trigger, which accepts events with a minimum of 5 L1 hits appearing in a time window of 2.2 μs.
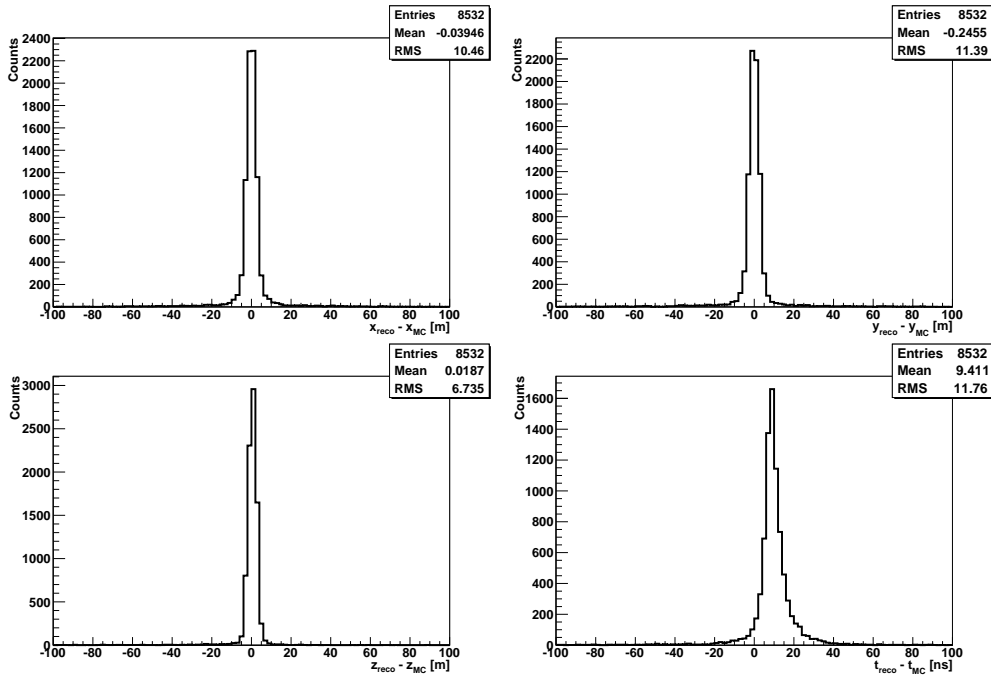
Figure 5.7: Performance of the full shower vertex reconstruction on the MC sample of NC muon-neutrino-induced showers.

2. **Pre-shower vertex reconstruction**: The SMST-Estimator, described in section 5.1.1, uses the 3N-triggered hits to provide starting points for the M-Estimator (see section 5.1.2).

3. **Post-hit selection**: The pre-reconstructed space-time positions of showers, estimated by the M-Estimator in the previous step, are exploited to run the *shower-hit selector* algorithm, introduced in section 5.2. The *Shower-hit selector* accepts all L0 hits, i.e. the number of photo-electrons (p.e.) measured by the PMT has to be larger than 1, and selects hits which appear in the time window of $-10 < \Delta t < 14$ ns. The hits with amplitudes corresponding to a charge larger than 2.5 p.e. are always kept.

4. **Post-shower vertex reconstruction**: The hits selected in the previous step are fed to the SMST-Estimator. The final shower-interaction vertex fit is provided by the M-Estimator, using the selected hits and the starting points provided by the previous SMST-Estimator.

The performance of the full shower-vertex reconstruction algorithm is presented in figure 5.7, resulting from the previously described stepwise combination of the shower-vertex reconstruction and the hit selection. Applying the full shower-vertex reconstruction yields 33% improvement in the resolution of the interaction vertex reconstruction, and a 20% gain in the number of reconstructed showers within ± 5 m from the true shower vertex.

The positive offset seen in the interaction-time reconstruction is likely caused by the fact that the shower light is continuously emitted in the shower depth and not exactly at the shower vertex. The finite travel time of shower particles with velocity above the phase velocity of light in water, equation 5.1, always
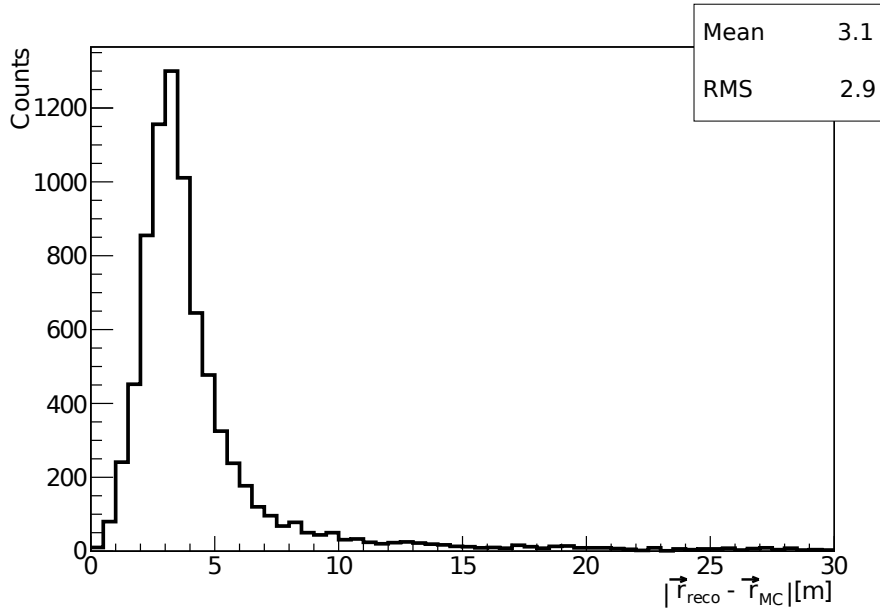
Figure 5.8: The absolute distance between the true MC vertex position of showers and the reconstructed vertex position. The distribution shows a shift of 3.1 m in the shower vertex reconstruction.

causes a positive time shift. Figure 5.8 demonstrates the distribution of the absolute distance between the reconstructed and MC position of the shower vertex. The distribution resembles the distribution of the intrinsic mean depth of showers (see figure 5.1). The shift in the absolute distance between the reconstructed and MC position of the shower vertex is consistent with the positive shift in the interaction-time reconstruction.

5.4 Direction Reconstruction

Light Direction

Besides the main objective to derive information on the direction of possible neutrino sources, a valuable advantage of reconstructing the direction of neutrinos is to separate them from the overwhelming down-going atmospheric muon background. In case of neutrino-induced showers only the cascades of hadronic particles (from NC interactions) or hadronic and leptonic particles (from CC interactions) carry the information of the direction of the incoming neutrinos. Figure 5.9 shows that the mean direction of the cascade particles is correlated with the direction of the incoming neutrinos. Therefore, the direction of showers can be approximated as the direction of the incoming neutrinos. However, since the typical length of showers is at least by 2 orders of magnitude shorter than the length of the muon tracks, the angular resolution of the showers is inherently poorer than that of the muon tracks. This requires a direction reconstruction method which is efficient for both showers and muon tracks. In the following, we introduce a method, called *Light Direction*, which provides a rough estimation of the direction of the events by calculating the direction of the light emission vector $\vec{D}$.
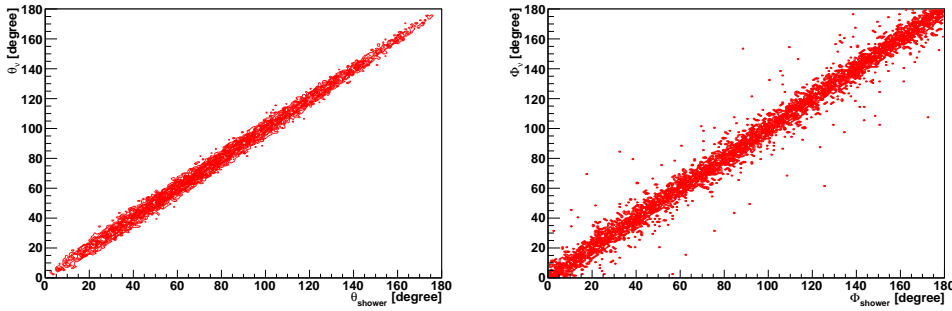
Figure 5.9: Left: Distribution of the zenith angle θ_ν of simulated neutrinos versus that of the mean shower. Right: Distribution of the azimuth angle Φ_ν of neutrinos versus that of the mean shower.
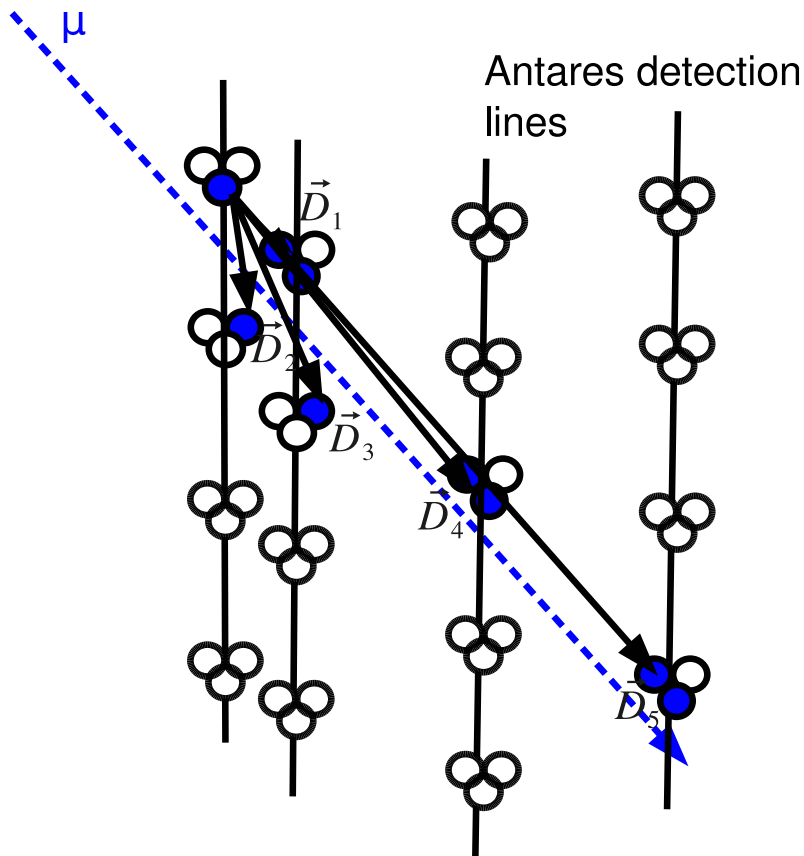
Figure 5.10: The principle of the Light Direction method. The passage of a down-going muon (dashed arrow), the light vectors $\vec{D}_i$ (solid arrows) and the hit PMTs (filled circles) are shown schematically.

Figure 5.10 shows schematically the passage of a down-going muon (dashed arrow) through the ANTARES detector. The Cherenkov light emitted from the muon track hits a certain number of PMTs (filled circles). The light direction $\vec{D}$ is defined as the mean of the light vectors $\vec{D}_i$ (solid arrows), which connect the earliest hits to all other $N - 1$ hits.
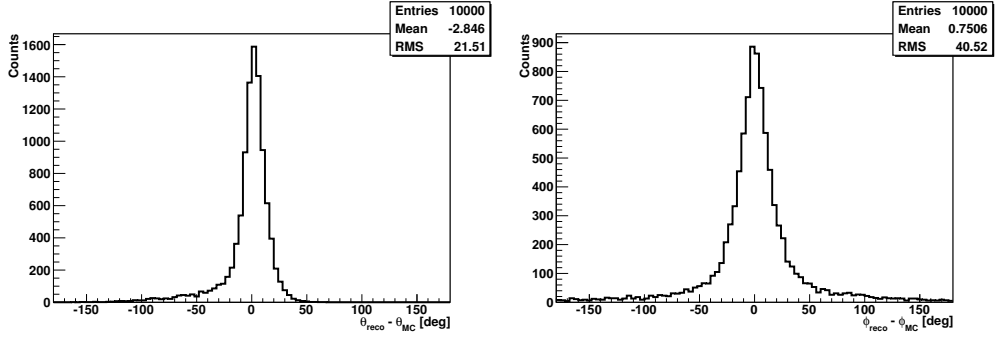
Figure 5.11: The performance of the *Light Direction* method on MC samples of atmospheric muon tracks. Shown are the differences between the true MC zenith angles θ (left) and azimuth angles ϕ (right) for the MC thrown events and the reconstructed ones.
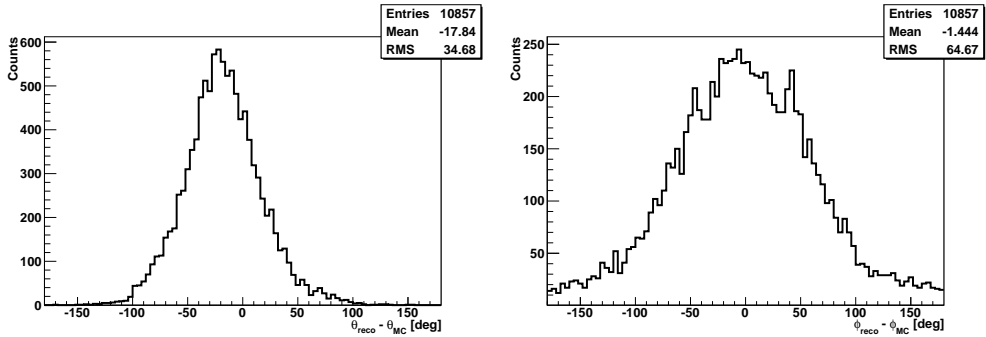
Figure 5.12: The performance of the *Light Direction* method on MC samples of neutrino-induced showers. Shown are the differences between the true MC zenith angles θ (left) and azimuth angles ϕ (right) for the MC thrown events and the reconstructed ones.

$$\vec{D} = \frac{1}{N-1} \sum_{i=1}^{N-1} \vec{D}_i. \tag{5.8}$$

The performance of the *Light Direction* method on the MC samples of atmospheric muon tracks and showers is shown in figure 5.11 and figure 5.12, respectively. The spread of the distribution of the θ angle is about $22°$ for atmospheric muon tracks and $35°$ for showers, and the spread of the ϕ angle is $41°$ and $65°$ for atmospheric muon tracks and showers, respectively. The negative offset in the θ angle distribution in figure 5.12, which indicates the preference of the algorithm to reconstruct an up-going event, is partially caused by the downward orientation of the ANTARES PMTs. Therefore, any up-going selection ($\theta < 90°$) mostly preserves all up-going showers. Even though the *Light Direction* method does not precisely reconstruct the direction of events, it can be exploited to efficiently discriminate the down-going atmospheric muons from up-going showers. In order to keep the efficiency and purity of the discrimination high, we combined the *Light Direction* method with *BBFit*, an algorithm for muon track reconstruction [A+11b]. The combination of both methods will be introduced in chapter 6.

51

5.5 Shower Energy Reconstruction

As discussed in the previous section, the inherent characteristic of showers, i.e. short-length trajectories of cascade particles, deteriorates the directionality of showers compared to that of muons. However, this characteristic can be exploited to advance the energy determination of neutrino-induced showers compared to that of neutrino-induced muons. The information on the energy of incident neutrinos can be retrieved from the light produced by the secondary cascade particles. In case of electromagnetic cascades, the light production can be easily explained: The electron produces bremsstrahlung photons and photons contribute to electron-positron pair productions. The secondary electrons and positrons can emit bremsstrahlung photons and the process can continue until the energy of cascade particles drops below the critical energy, i. e. the energy at which the rates of the losses by bremsstrahlung and ionization [Eid04] are equal.

The light-production process in hadronic showers is more complex than that in electromagnetic showers, since many different hadronic particles contribute to the light production and their contributions can fluctuate from event to event. Neutral and charged pions are the most dominant particles in a NC-induced shower and the remaining particles can be protons, neutrons and kaons, depending on the shower energy. Neutral pions have a very short lifetime and decay into photons which can produce electron-positron pairs, and then induce electromagnetic showers. The contribution of the electromagnetic shower can exceed 90% for showers with an energy of 1 TeV (see [Bru]). Figure 5.13 shows the typical composition of hadronic particles in a simulated NC shower. In the simulation only the primary hadronic particles are tagged, and the Cherenkov light and the electron-positron pair production, caused by the energy loss of the primary particles, are not included. The particles with a lifetime shorter than $10^{-10}s$ are not tagged in the simulation: this is the reason that the highest contribution in figure 5.13 stems from γ which are photons caused by the decay of π^0.

To estimate the neutrino energy, we use the hypothesis that the total hit amplitude A^{tot}, which is the sum of amplitudes of all hits in an event, is correlated to the energy of the incoming neutrino. Since the light acceptance α_i of any ANTARES PMT i is a function of the angle of incidence of the incoming light, the hit amplitudes must be weighted accordingly. In addition, we take into account the light intensity loss according to the light attenuation τ and the distance of the hit PMTs from the source of shower light, which is assumed to be at the shower vertex. Considering all the corrections described above, we formulate the shower energy estimator ρ as follows:

$$\rho[a.u.] = \frac{A^{tot}}{\frac{1}{N} \sum_{i=1}^{N} \frac{\alpha_i}{|\vec{r}_i - \vec{r}_s|} e^{-|\vec{r}_i - \vec{r}_s|/\tau}} \tag{5.9}$$

where r_s is the position of the shower vertex, which is provided by the previously described shower reconstruction algorithm, and r_i is the position of the hit PMT i (see figure 5.14). The summation applied in the equation smoothes out the effect of outliers, i.e. distant hits caused by optical noise, in the determination of the ρ parameter. The shower energy reconstruction method looks very similar to the ANTARES muon energy estimators described in [RBZ03].

To improve the quality of the energy reconstruction, a cut on a defined containment volume is introduced, such that only events whose reconstructed ver-
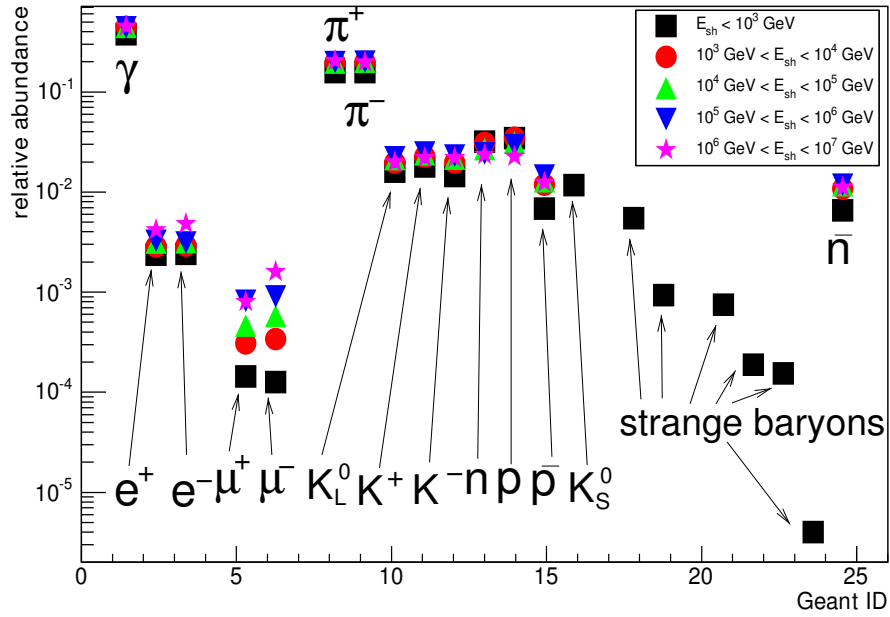
Figure 5.13: Relative abundance of particles in a typical NC neutrino-induced shower for different shower energies. The figure is taken from [Har06].
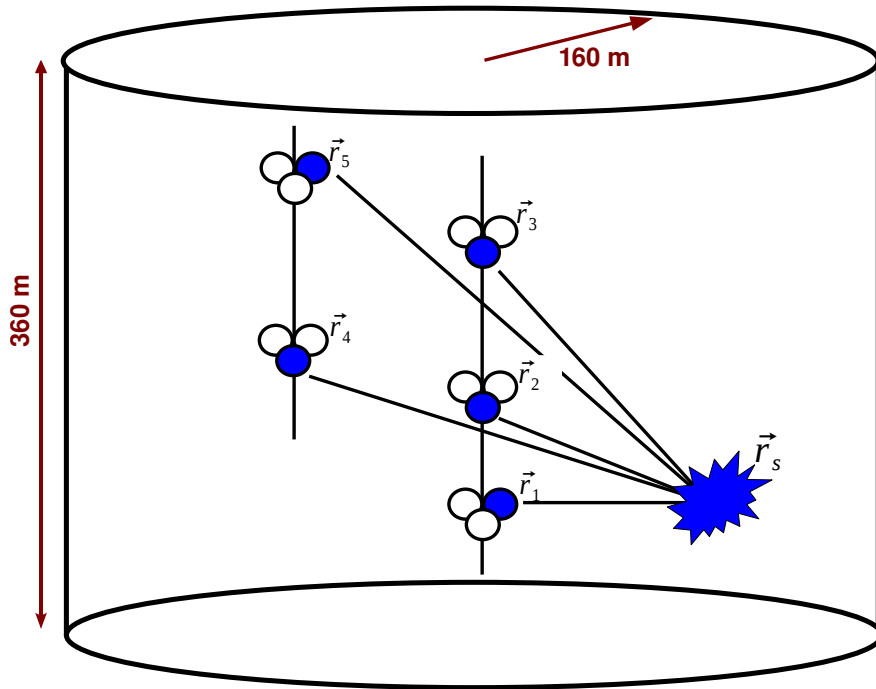
Figure 5.14: Schematic view of the energy reconstruction algorithm. The cylinder shows the containment volume. The centre of the cylinder lies at the centre of the detector.

tices fall into the cut region are considered for the energy reconstruction. The containment volume is a cylinder with a radius of 160 m and a height of 360 m, centred at the detector centre (see figure 5.14).

Figure 5.15 (left) shows the energy estimator ρ as a function of the simulated
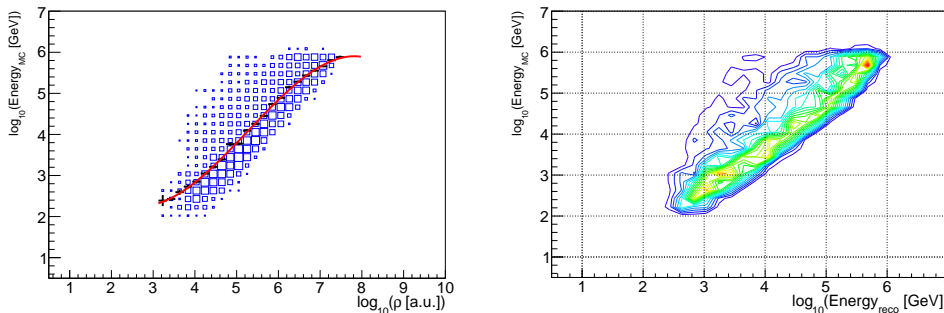
Figure 5.15: Left: Distribution of the true (MC) neutrino energy as a function of the energy estimator ρ. The polynomial function which has been applied to convert ρ to the neutrino energy is shown as the solid curve. Right: Distribution of the true (MC) neutrino energy as a function of the reconstructed neutrino energy.

neutrino energy. Data sample 2, described in section 4.5, has been used for the parametrisation of the neutrino energy. The estimator and the neutrino energy are highly correlated with a correlation coefficient of 0.86. One has to keep in mind that the profile distribution can be very dependent on the input neutrino energy flux. In order to be independent of the neutrino energy, the number of entries in every energy bin has been equalized [1]. To retrieve the shower energy, a 3rd order polynomial function has been fitted to the profile distribution. Then the relation between the shower energy and ρ is given by:

$$
\begin{aligned}
log_{10}(E_\nu[GeV]) \quad &= -0.06 \times log_{10}^3\rho[a.u.] + 0.9 \times log_{10}^2\rho[a.u.] \\
&\quad -3.5 \times log_{10}\rho[a.u.] + 6.5
\end{aligned}
\tag{5.10}
$$

Figure 5.15 (right) shows the reconstructed neutrino energy as a function of the true neutrino energy, applying the parametrisation introduced in equation 5.10. The performance of the method in the neutrino energy range of 100 GeV – 10 PeV is shown by the distribution of the reconstructed energy in figure 5.16. The neutrinos are weighted according to a test flux of cosmic neutrinos [Fer49] [2] of the following form:

$$
\Phi_\nu \propto E^{-2}[GeV^{-1}cm^{-2}s^{-1}sr^{-1}].
\tag{5.11}
$$

The method results in an energy resolution of a factor of $10^{0.403} = 2.5$ on the neutrino energy. Despite some necessary simplifications in the shower-reconstruction method, the obtained energy resolution of neutrinos performs better than other methods used to reconstruct the neutrino energy from induced muon tracks. Previous methods in ANTARES [RBZ03] achieved a maximum resolution of a factor of 3 on the neutrino energy.

In order to reduce the effect of systematic uncertainties in the parametrisation of neutrino energy, we will abandon the parametrisation of ρ and we will directly

---

[1] In order to minimize the statistical bias, we randomly pick the entries from the whole statistics and put them equally in each energy bin.
[2] In section 6.4, we use this flux to search for high-energy neutrinos.

Figure 5.16: Performance of the energy reconstruction algorithm in the neutrino energy range of 100 GeV – 10 PeV. Each entry in the histogram is weighted according to a cosmic neutrino flux of $\Phi \propto E^{-2}$.

exploit ρ as a discriminating parameter in order to suppress the background of atmospheric neutrino events (see section 6.4.2).

Chapter

Event Selection

When the theoretical sciences are isolated and their possessors do not have the faculty for exploiting them for the benefit of others, they are defective philosophy.
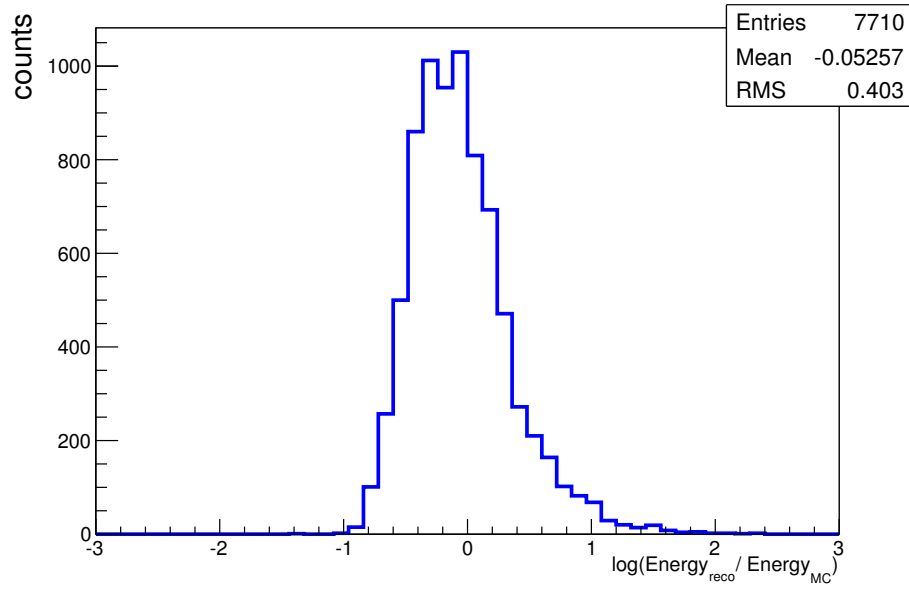
Abu (Al-)Nasr (Al-)Farabi

Atmospheric muons constitute one of the most serious backgrounds for any search of high-energy neutrinos. ANTARES is primarily designed to reject this background by selecting upward-going muons, using the Earth as a filter against all particles except neutrinos. Such a rejection strategy relies on a very efficient direction reconstruction method. As previously presented in section 5.4, neutrino-induced showers have an inherently poor angular resolution. This means that any effort to reject the overwhelming amount of down-going muons from shower events would face an unacceptably low efficiency, if the analysis method only exploits the conventional event-selection strategy based on the direction reconstruction. In this chapter we introduce a new selection strategy that serves to reject the background of atmospheric muons to an acceptable level. The selection strategy is based on selection criteria which exploit several cuts on direction and topology of neutrino-induced showers. The strategy has been optimised for the observation of showers induced by a diffuse flux of high-energy cosmic neutrinos. To avoid a possible bias in the selection strategy, a blind analysis has been applied. We have tuned the selection strategy by analysing a Run-by-Run MC sample corresponding to ANTARES data taken during 2008-2010.

Section 6.1 describes a method to suppress the down-going atmospheric muon background by exploiting the reconstructed direction of the events. In order to achieve a high muon background-rejection factor, we have combined the results of the *Light Direction* algorithm (see section 5.4) with BBFit, an algorithm for muon track reconstruction (see [A+11b]).

We take advantage of the shower topology which resembles a compact object, differentiating showers from muon tracks (see section 6.2). The fit-quality parameters obtained from the shower vetrex reconstruction algorithms (see section 5.1) will be exploited to select shower-like events.

Section 6.3 presents a multivariate analysis (MVA) of neutrino-induced showers, which consists of two levels: Pre-filtering of muons (see section 6.1 and section 6.2) and post-event classification. To provide a benchmark test, we have applied two independent classification methods for the post-event classification (see section 6.3.1 and section 6.3.2). The final event selection will be furnished by a cut on the total deposited charge serving as energy estimator.
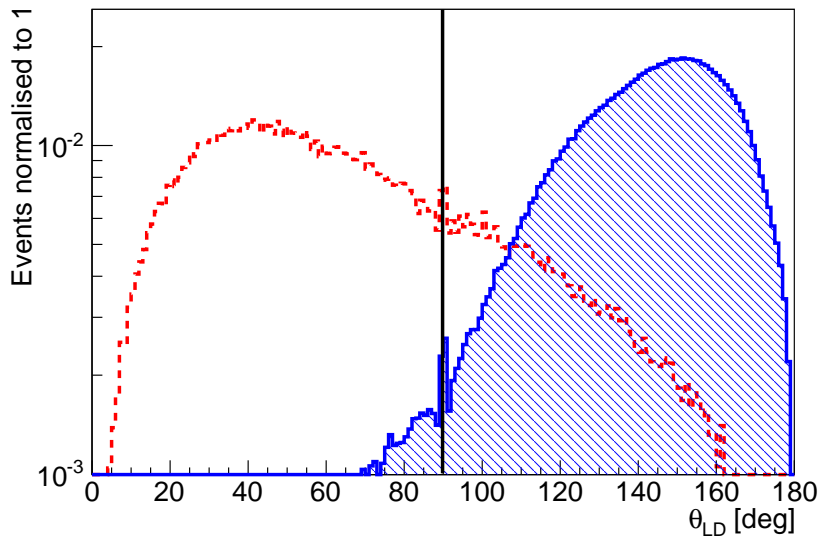
Figure 6.1: Distribution of the zenith angle θ_{LD} for simulated atmospheric muons (filled (blue) area) and neutrino-induced showers (dashed (red) line) reconstructed by the *Light Direction* method. The vertical line indicates the position of a cut at $\theta_{LD} = 90°$. The contents of the two distributions are separately normalised to 1.

Section 6.4 describes a method to optimise the shower selection strategy by exploiting a stepwise optimisation procedure. First, we largely suppress the background of atmospheric muons by applying an optimal cut-doublet on total deposited charge per event and a MVA score. The optimal cut-doublet is achieved by maximizing the significance of shower selection (see equation 6.3). Finally we select cosmic neutrino-induced shower candidates by imposing an additional cut on the energy estimator ρ (see section 5.5). The final optimisation step relies on the maximization of the sensitivity for the observation of showers induced by a diffuse flux of cosmic neutrinos.

6.1 Up-Going Selection

As the first-level filter, we cut on the direction of the events and select the up-going events, exploiting the Earth as a natural filter against atmospheric muons. This requires a direction reconstruction algorithm which efficiently reconstructs the muon directions and at the same time preserves the up-going showers. As shown in section 5.4, the *Light Direction* method can be a good option for this algorithm. Figure 6.1 shows the distribution of the reconstructed zenith angle θ_{LD} for atmospheric muons (filled (blue) area) and neutrino-induced showers (dashed (red) line). By imposing a cut at $\theta_{LD} = 90°$ the *Light Direction* method selects showers with an efficiency of about 74% and rejects atmospheric muons by a factor of about 17.

To suppress the remaining contamination by mis-reconstructed atmospheric muons appearing as up-going tracks, we have exploited BBFit [A+11b], an independent muon-track reconstruction algorithm. BBFit is a robust algorithm which
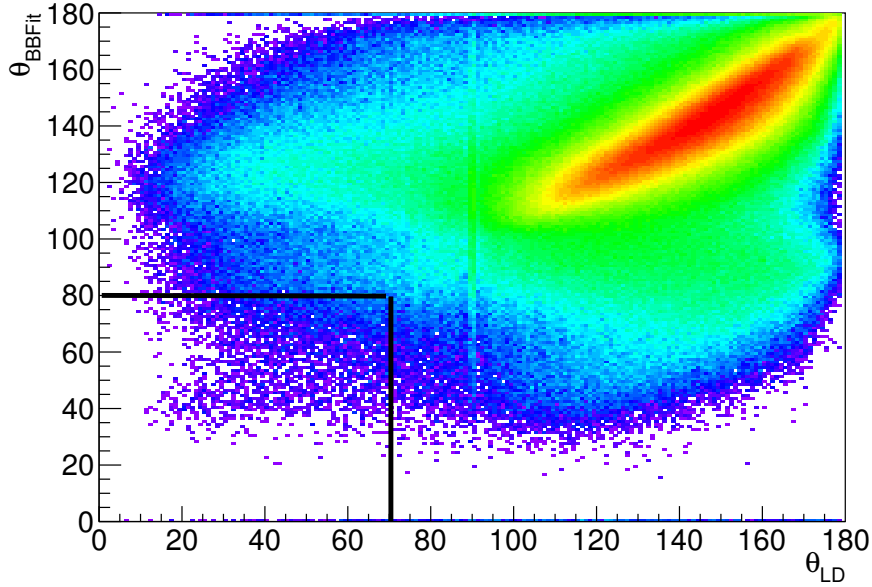
Figure 6.2: Distribution of the zenith angle θ_{BBFit}, reconstructed by BBFit, as a function of the zenith angle θ_{LD}, reconstructed by the *Light Direction* method, for simulated atmospheric muons. The region of the up-going directions is marked by a rectangle. The colour code represents the intensity from high to low by red to white.

has been optimised to reconstruct up-going muon tracks. BBFit consists of a hit-selection procedure which allows to select hits caused by muon tracks with high purity, while keeping the efficiency high. The algorithm selects direct Cherenkov photons emitted from the point of closest approach of muons to the ANTARES detection lines. Subsequently the selected hits are exploited to fit the events based on either the muon-track hypothesis or the hypothesis of a point-like light source. A χ^2 function is defined to judge the goodness of the fit for track events, χ^2_{Track}, and point-like light sources, χ^2_{Bright}. At this step, we did not apply any cut on the fit-quality parameters of BBFit, but we include the χ^2_{Track} parameter in the multivariate analysis in section 6.3.

Figure 6.2 presents the distribution of zenith angles of atmospheric muons reconstructed by BBFit as a function of zenith angles reconstructed by the *Light Direction* method. In order to suppress the atmospheric muon background most efficiently, we have combined the two direction reconstruction algorithms, such that we have applied a rectangular cut requiring $\theta_{LD} < 70°$ and $\theta_{BBFit} < 80°$. This selection accepts only events which are reconstructed as up-going by both algorithms. The combination of *Light Direction* method and BBFit results in a muon rejection factor of about 250 with a shower selection efficiency of 40%.

6.2 Cut on Shower-Fit Quality Parameters

The hypothesis under which shower vertices have been fitted in section 5.1 follows the idea that all shower light is produced by a point-like source. The estimated values of the fit-quality parameters R (see equation 5.6) and M (see equa-
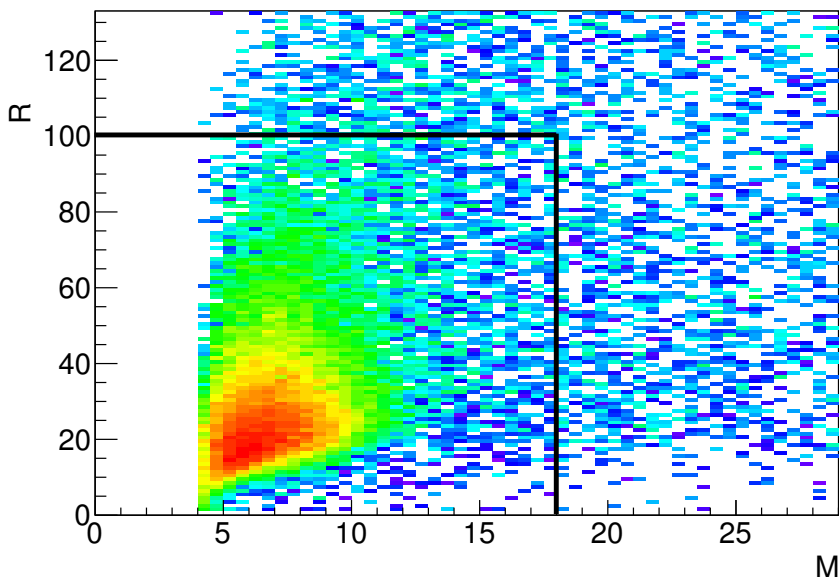
Figure 6.3: The distribution of the residual R as a function of the M-Estimator for up-going showers. The rectangle marks the shower region ($R < 100$ and $M < 18$). The colour code represents the intensity from high to low by red to white.

tion 5.7) can judge how well an event indeed looks like a point-like object. In this section, we apply cuts on R and M in order to suppress the mis-reconstructed atmospheric muons remaining after the up-going selection, by selecting shower-like events.

Figure 6.3 shows the distribution of the residual R as a function of the M-Estimator for up-going shower events. Since most of the showers are concentrated in the region $R < 100$ and $M < 18$, we call it the *shower region*. Selecting events in the shower region rejects the mis-reconstructed up-going atmospheric muons by a factor of about 2000 with a cumulative shower selection efficiency (i.e. including the up-going rejection) of 14%.

The criteria introduced in sections 6.1 and 6.2 perform the *pre-filtering* of events. Events passing these criteria are fed to the next step of *post-event classification* which applies a multivariate method, introduced in the next section.

Table 6.1 summarises the shower selection efficiency and muon rejection factor after each pre-selective cut.

6.3 Multivariate Classification of Events

The main objective to apply a multivariate classifier is to reduce a multi-dimensional set of discriminating parameters to a single discriminating parameter. This approach will simplify the complexity in optimising the search for neutrino-induced showers. In addition, despite of the selective cuts applied in the previous stages, the signal-to-noise ratio is still low, i.e. about 1:2400. Therefore, a multi-dimensional optimisation of the selective cuts can significantly improve the signal-to-noise ratio. In this analysis we have used two independent event classifiers: *K-Nearest Neighbour* (KNN) and *Boosted Decision Tree* (BDT). We exploit the Toolkit for Mul-

cut	shower selection efficiency	muon rejection factor
up-going $\theta_{LD} < 70°$ and $\theta_{BBFit} < 80°$	40%	250
$M < 18$ and $R < 100$	14%	2000

Table 6.1: Cumulative shower selection efficiency and muon rejection factor after the pre-selection level. The shower selection efficiency and muon rejection factor are defined for reconstructed events, i.e. the intrinsic event reconstruction efficiency is not included in the calculations of the shower selection efficiency and muon rejection factor.

tivariate Data Analysis (TMVA) with ROOT [H+39] to implement the two classifiers. TMVA consists of different steps of training, testing and evaluating for each classifier. It can take data sets in the form of ROOT trees or text files for training and testing. Each event can be weighted either individually, in order to reproduce the expected exponential slope, or globally. In this analysis, in order to avoid the statistical bias due to weighting of events, we applied a global weight of 1.0 for both the shower and atmospheric muon events. In addition, in order to avoid classification problems due to the correlation of the discriminating variables, we chose an option in TMVA, which transforms the distribution of the discriminating variables such that they comply with distributions of normalised Gaussian shape.

The discriminating parameters used in the multivariate classifiers are the following:

- θ_{LD}, zenith angle reconstructed by *Light Direction* method.

- θ_{BBFit}, zenith angle reconstructed by BBFit.

- χ^2_{Track}, the BBfit track fit quality parameter.

- R, Residual parameter (see section 5.1.1).

- M, M-Estimator fit-quality parameter (see section 5.1.2).

- $\sqrt{R \times M}$.

Figure 6.4 shows the distribution of the discriminating parameters for MC simulations of atmospheric muon events (solid (blue) histogram) and neutrino-induced shower events (dashed (red) histogram), as well as the 5% of the experimental events mentioned in table 4.4 (cross markers). We observe a very good agreement between experimental data and MC simulations of atmospheric muons. Even though many of the discriminating parameters have been used for the pre-filtering of the events, their combined exploitation allows for sharper cuts and, therefore, has a high discriminating potential.
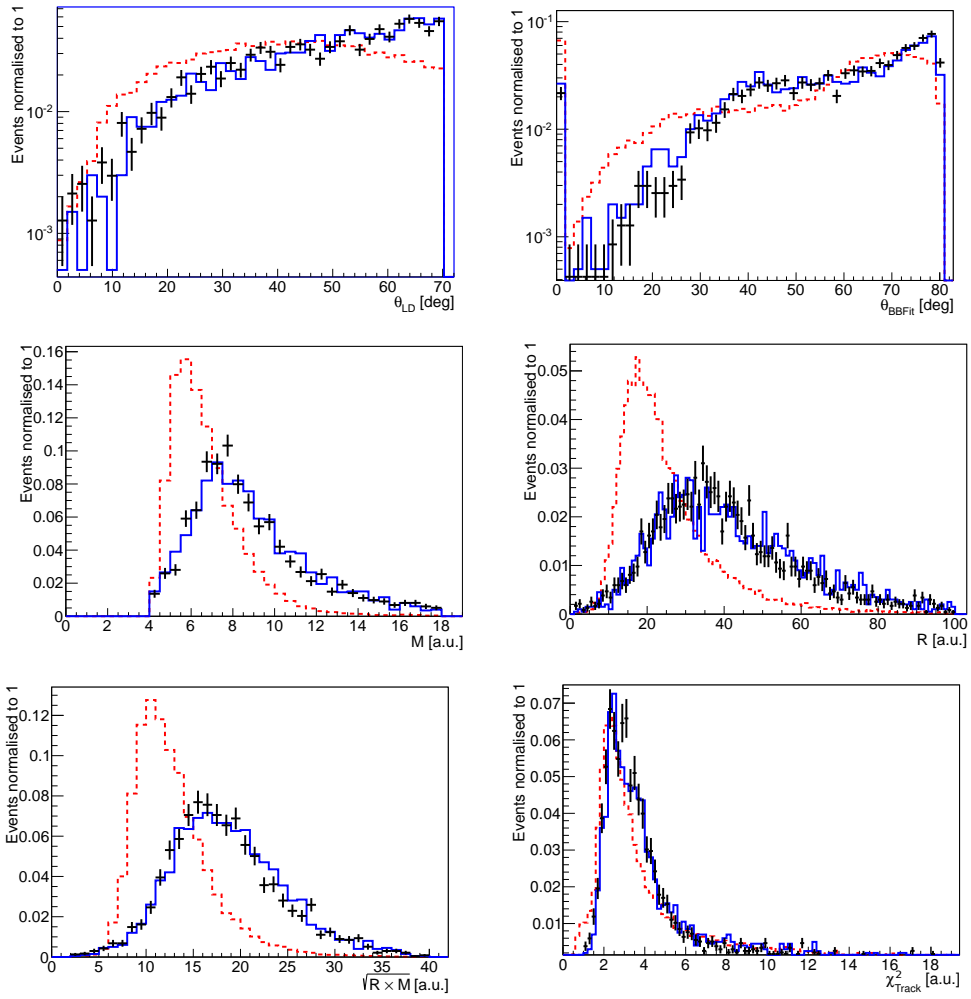
Figure 6.4: Distribution of the discriminating parameters for MC atmospheric muons (solid (blue) histogram) and neutrino-induced showers (dashed (red) histogram), as well as experimental events (cross markers).

The TMVA algorithm can be trained to provide optimal values of the discriminating parameters. In this analysis we have used Run-by-Run simulated data samples for atmospheric muons and neutrino-induced showers (see section 4.4), corresponding to a livetime of 52 days. Half of the samples were used to train the algorithm and the other half has been used to evaluate the Multivariate classifiers. In the next sections, the training and testing procedures for KNN and BDT classifiers will be explained.

6.3.1   K-Nearest Neighbour

The KNN algorithm compares observed data sets (testing events) to a reference data set (training events). KNN scores each observed event based on the number density of the signal events in a multi-dimensional training space containing *k* events nearest to the observed event. More details about the KNN method can be found in section 8.5 of [H+39]. The degree of *near* is measured by using the Euclidean distance D, defined as:
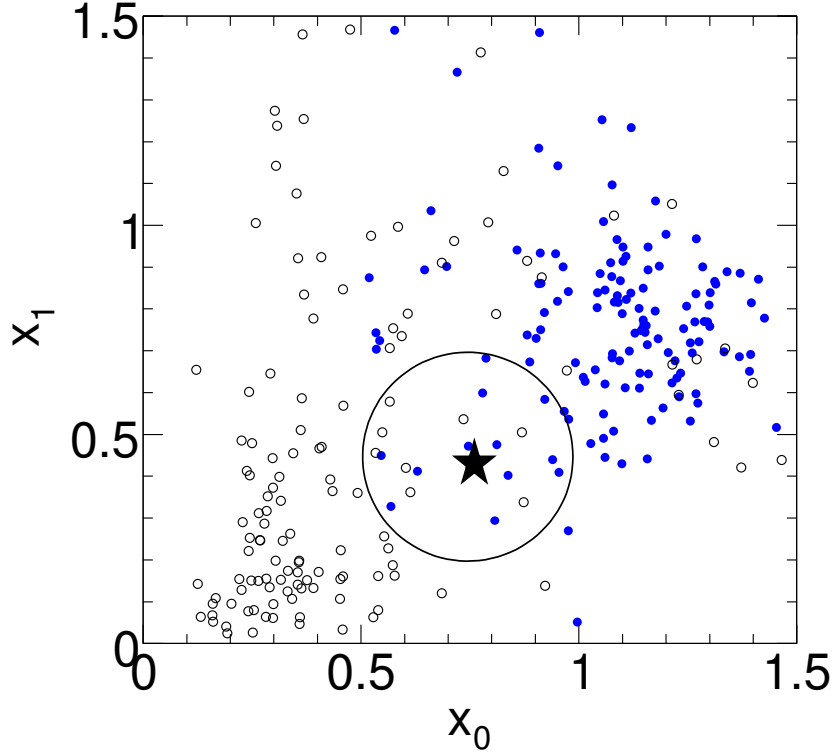
Figure 6.5: Schematic of the *k-Nearest Neighbour* algorithm. Shown is the correlation of discriminating parameters x_0 and x_1 for signal events (filled (blue) circles) and background events (open (black) circles). The algorithm searches for $k = 20$ neighbours around the test event (star). The image was taken from [H+39] and has been slightly modified for the purpose of this analysis.

$$D = \left(\sum_{j=1}^{n_{par}} |x_j - y_j|^2 \right)^{1/2}, \tag{6.1}$$

where n_{par} is the number of discriminating parameters, x_j and y_j are the values of the jth parameter from training and testing events, respectively. Therefore, k events with the smallest D are the $k - nearest\ neighbours$. Figure 6.5 schematically illustrates the KNN scoring procedure for the ith test event (star) in two-dimensional space (i.e. for two discriminating parameters x_0 and x_1). The circle represents the region containing $k = 20$ events. The nearest neighbourhood counts 12 signal and 8 background points so that the test event may be classified as a signal event with a score of $\frac{12}{20}$.

In this analysis the numbers of signal (shower) and background (atmospheric muon) events are taken to be equal in the training samples. The event weights were assumed to be equal 1.0 for all shower and atmospheric muon events. Therefore, the output of *KNN* can be interpreted as the signal posterior P_S, the probability of observing a shower after a set of discriminating parameters $\vec{\xi}$. The signal posterior is given by the following relation:

$$P_S(S|\vec{\xi}) = \frac{P(\vec{\xi}|S)P(S)}{P(\vec{\xi}|S)P(S) + P(\vec{\xi}|B)P(B)}, \tag{6.2}$$

where the vector $\vec{\xi} = (\theta_{LD}, \theta_{BBFit}, \chi^2_{Track}, R, M, \sqrt{R \times M})$ contains the set of discriminating parameters, introduced previously. The term $P(\vec{\xi}|S)$ is the signal likelihood, which indicates how likely $\vec{\xi}$ is observed if the event is of shower type. $P(S)$ and $P(B)$ are the probabilities of observing showers and atmospheric muons, respectively, before $\vec{\xi}$ is selected. According to our previous assumptions, i.e. the number of showers is equal to that of muons and each event weight is equal 1.0 for all events, $P(S) = P(B) = 0.5$.

Figure 6.6 (top) shows the distribution of the KNN scores of testing events for neutrino-induced showers (signal shown as a solid (red) histogram) and muon tracks (background shown as a filled (blue) histogram). The superimposed data points with the statistical error bars indicate the distribution of KNN scores for the training events, which is in good agreement with that for the testing events.

To evaluate the performance of the multivariate algorithms, the following evaluation parameters are defined:

$$
\begin{aligned}
Signal\ efficiency &= \frac{S}{S_0} \\
Background\ efficiency &= \frac{B}{B_0} \\
Signal\ purity &= \frac{S}{S + B} \\
Significance &= \frac{S}{\sqrt{S + B}}
\end{aligned}
\tag{6.3}
$$

where S and B are the number of signal and background events after a cut, respectively, and S_0 and B_0 are the number of signal and background events before a cut, respectively.

Figure 6.6 (bottom) shows the behaviour of the evaluation parameters (equation 6.3) as a function of the KNN score. The number of shower and atmospheric muon events is equal to 1000. To optimise the selection of shower events, we combine a cut on the KNN score with a cut on the total deposited charge per event. This procedure will be introduced in section 6.4.1.

6.3.2 Boosted Decision Tree

The Boosted Decision Tree (BDT) method consists of a sequence of cuts which split the events into either signal-like or background-like events. In this sense the selection strategy of BDTs is equivalent to rectangular cuts, however, with the major difference that the BDTs are able to split the phase space into a large number of partially identified sub-events, i.e. signal-like and background-like events, which define so-called hypercubes.

Figure 6.7 schematically presents a decision tree. A decision tree looks like an inverted tree starting from the root node. At the root node, the algorithm selects a best discriminating parameter (x_v) and a cut value c_n, which splits the root node into signal-like and background-like sub-nodes. The selection will continue choosing the best discriminating parameter by cutting at each sub-node and splitting the events into more sub-nodes until the number of events in a node reaches a minimum value. The nodes at the end of the tree, the so-called leaf nodes, are labelled as signal or background depending on the purity of the events in the respective leaf nodes.

Figure 6.6: Top: Distribution of the KNN score for atmospheric muons (filled (blue) histogram) and neutrino-induced showers (solid (red) histogram). Bottom: Evaluation parameters as a function of the KNN score.

The statistical fluctuations in the training events can cause an instability problem in the decision tree. The instability problem can be due to two or more parameters having the same discriminating potential. Thus the tree may decide to split all nodes by choosing only one discriminating parameter, which can cause more fluctuations in the tree, while the other parameters could have been chosen without causing the fluctuations. To overcome such a problem, a *boosting procedure* is applied. In a boosting procedure a forest of decision trees is constructed by using the same training events repeatedly. After a tree is constructed, the events mis-classified in this tree will be weighted higher in the next tree, so that the same discriminating parameters and cut values are less likely to be chosen for the next tree. Finally, an event is classified according to the major votes of individual de-
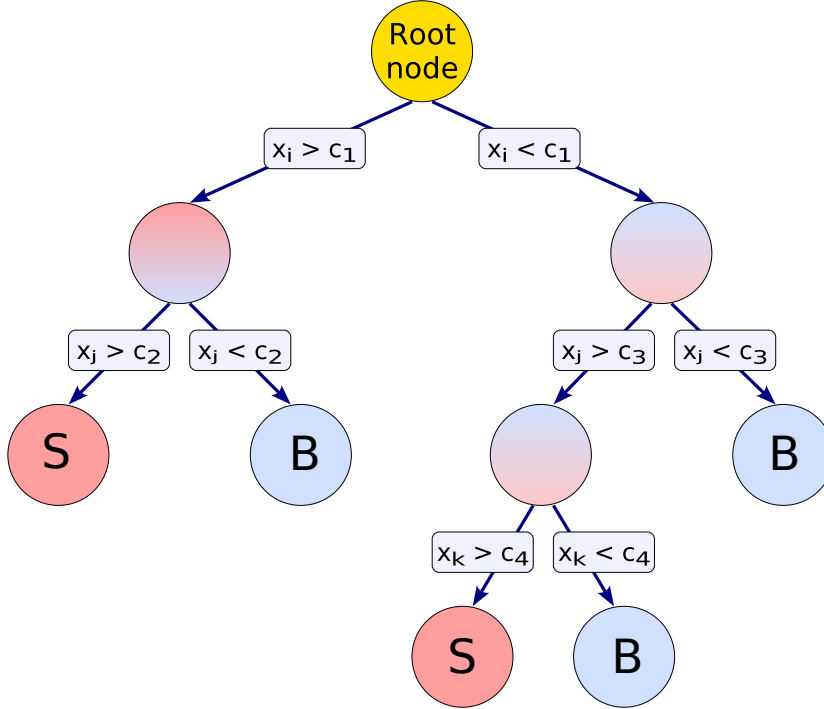
Figure 6.7: Schematic view of the BDT algorithm. Choosing the best discriminating parameters x_ν and cut values c_n at each node, the algorithm labels the nodes at the bottom of the tree as "S" for signal and "B" for background, depending on the purity of the events at the respective nodes (the figure is adapted from [H+39]).

cisions made by each tree in the forest. For a more detailed explanation we refer to [H+39].

In this analysis, we constructed a forest of 400 trees. The same discriminating parameters as used for the KNN method were exploited for the BDT method. Figure 6.8 (top) presents the distribution of the BDT scores of testing events for neutrino-induced showers (signal shown as solid (red) histogram) and atmospheric muons (background shown as filled (blue) area). The data points are the distribution of BDT scores for the training events.

Figure 6.8 (bottom) shows the behavior of the evaluation parameters (equation 6.3) as a function of the BDT score. The number of shower and atmospheric muon events is equal to 1000.

6.4   Cut optimisation

In this section, we introduce two additional cut parameters, i.e. a cut on the total deposited charge per event (charge cut) and a cut on the energy-estimator ρ (ρ cut), in order to increase the significance of the shower selection. Therefore, we have three final cut parameters to be optimised. We introduce an optimisation procedure which consists of two steps: Two-dimensional charge-MVA score cut optimisation and ρ cut optimisation. The first optimisation step is exploited to remove the contamination of atmospheric muon events in the neutrino-induced shower events. The final optimisation step selects cosmic neutrino-
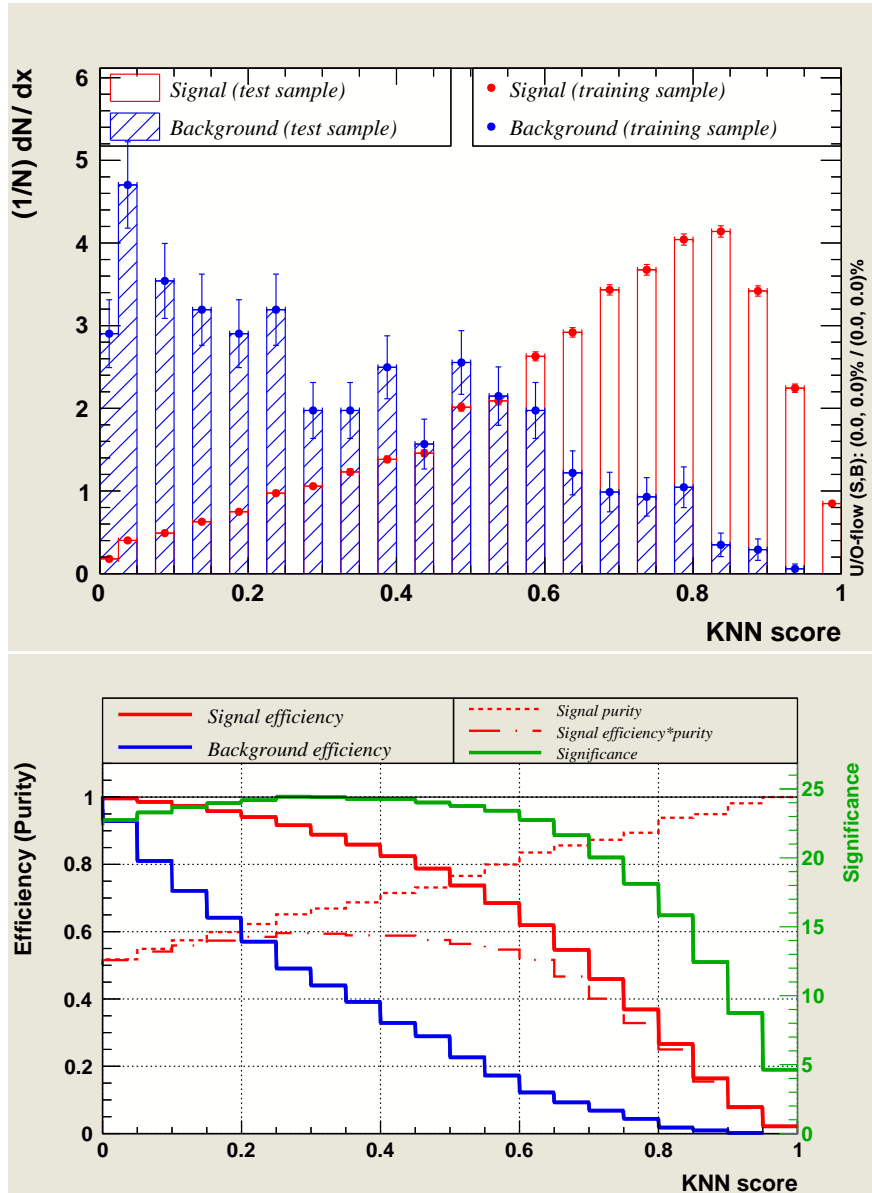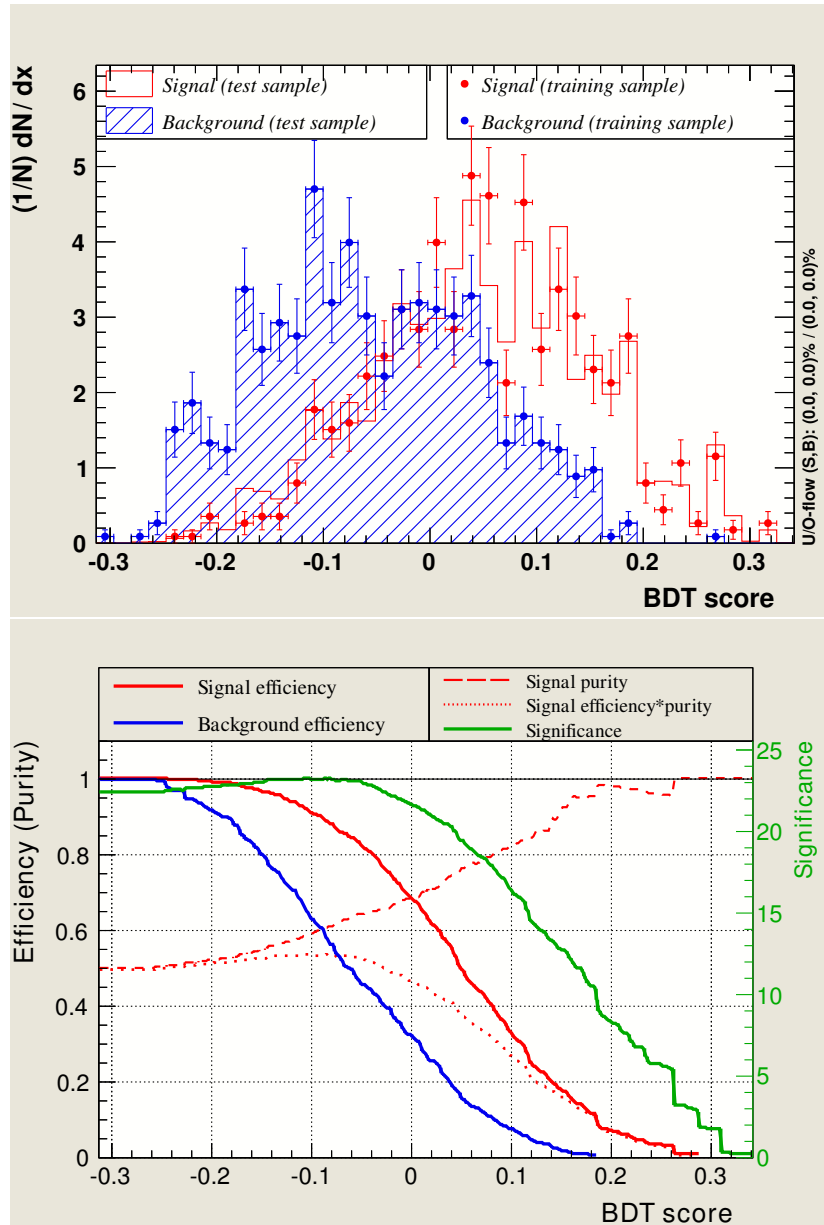
Figure 6.8: Top: Distribution of the BDT score for atmospheric muons (filled (blue) area) and neutrino-induced showers (solid (red) histogram). Bottom: Evaluation parameters as a function of the BDT score.

induced showers among the overwhelming amount of atmospheric neutrinos. The efficiency and purity of the optimisation method will be discussed in the following sections.

6.4.1 Two-dimensional Charge-MVA Score Cut Optimisation

As previously discussed in section 6.3, in order to avoid the statistical fluctuations in the training samples, we assumed the same detection rates for neutrino-induced showers and atmospheric muons. In this section, we scale down the detection rate of neutrino-induced showers according to realistic neutrino fluxes,
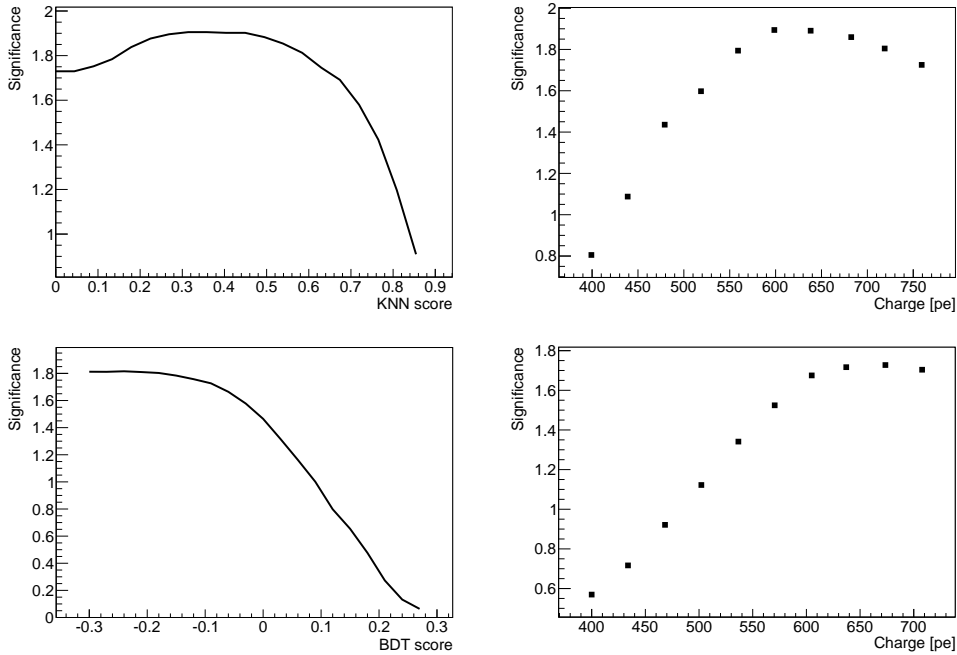
Figure 6.9: Significance as a function of a doublet of cuts on charge-KNN score (top) and on charge-BDT score (bottom).

i.e. atmospheric neutrinos and a diffuse flux of cosmic neutrinos in order to estimate the purity and the efficiency of the selection strategy. The main reason why we impose the two-dimensional cut on charge (in photo-electron) and MVA score is to largely suppress the contamination of the atmospheric muon events. The optimisation method relies on the maximization of the significance parameter introduced in equation 6.3. The optimisation is defined in this way:

- KNN and BDT scores were scanned in an interval of [0, 1] and [-0.3, 0.3], respectively. At each MVA score the maximum significance was calculated for different charge cuts.

- The optimal cut doublet (charge, MVA score) is selected according to the maximum value of the significance.

The optimisation method results in optimal cut doublets (600 p.e., 0.27) and (658 p.e., -0.09) corresponding to maximum significance values of 1.9 and 1.8 for KNN and BDT classifiers, respectively.

Figure 6.9 shows the significance as function of charge and score values for the KNN classifier (top) and the BDT classifier (bottom).

Figure 6.10 shows the distribution of the total deposited charge after cuts on the KNN score (top) and BDT score (bottom) of 0.27 and -0.09, respectively, for MC atmospheric muons (solid (blue) histogram) and all neutrino-induced shower types (dashed (red) histogram), i.e. cosmic neutrino-induced showers and atmospheric neutrino-induced showers, corresponding to a livetime of 656 days.

The number N_{ν_s} of (atmospheric and cosmic) neutrino-induced MC showers and the number N_μ of MC muons, remaining after the optimal cut-doublets,
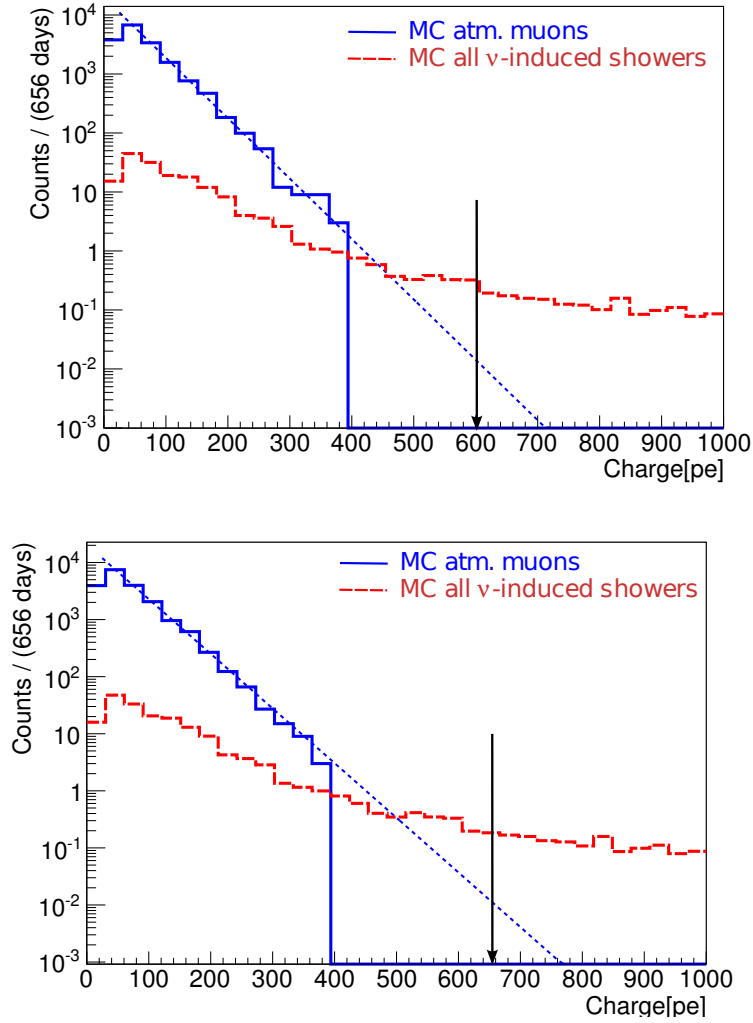
Figure 6.10: Distributions of total deposited charge per event after an applied cut on MVA scores of 0.27 and -0.09 for KNN method (top) and the BDT method (bottom). The neutrino detection rates are scaled down according to realistic neutrino fluxes. An exponential function has been fitted to the distribution of the atmospheric muons in order to avoid statistical fluctuations in the MC samples. The vertical arrow indicates the value of the optimal charge cut.

are summarised in table 6.2. In order to avoid statistical fluctuations in the MC samples, an exponential function has been fitted to the charge distribution of atmospheric muons to better estimate the expected number N_μ^{fit} of atmospheric muons after the applied cut-doublets.

6.4.2 ρ Cut Optimisation

As shown in the previous section, applying a two-dimensional cut on charge and MVA score can discriminate showers from atmospheric muons with purities better than 99%. In this section, we apply an additional cut on the energy estimator ρ (see section 5.5) in order to suppress the contamination of atmospheric neutrinos in the cosmic neutrino-induced shower samples.

MVA method	cut-doublet	N_{ν_s}	N_μ	N_μ^{fit}	purity
KNN	(600 p.e., 0.27)	3.9	0	0.02	99.5%
BDT	(658 p.e.,-0.09)	3.5	0	0.01	99.7%

Table 6.2: The expected number of events left after the optimal cut-doublets.

Figure 6.11 shows the distribution of the energy estimator ρ for atmospheric neutrinos (NC ν + CC ν_e + CC ν_μ) and cosmic showers induced by a test diffuse flux of cosmic neutrinos after cut-doublets (600 p.e., 0.27) and (658 p.e., -0.09) for the KNN (top) and BDT (bottom) classifiers, respectively. For the atmospheric neutrino flux, we take into account the so-called *Bartol* flux [B+30], i.e. the conventional atmospheric neutrinos from charged meson decay. The test diffuse flux for cosmic neutrinos follows the flux corresponding to the Fermi acceleration (see section 2.1):

$$E^2[GeV]\Phi_{cosmic} = \Phi_0 = 6 \times 10^{-7} \text{GeVcm}^{-2}\text{s}^{-1}\text{sr}^{-1}, \tag{6.4}$$

where Φ_0 is the strength of the flux. A cut at a high value of ρ can efficiently suppress the contamination of the atmospheric neutrino background in the selected cosmic shower signal.

To optimise the ρ cut, we search for the minimum value of the average flux upper limit at 90% confidence level $\bar{\Phi}_{90\%}$, under the assumption of no shower-signal observation. The average flux upper limit for the expected number N_s of showers induced by the test diffuse flux Φ_0 of cosmic neutrinos and the expected number N_b of atmospheric neutrinos (NC ν + CC ν_e + CC ν_μ) is given by:

$$\bar{\Phi}_{90\%} = \frac{\bar{\mu}_{90\%}(N_b)}{N_s}\Phi_0 \tag{6.5}$$

The upper limit for shower observation $\bar{\mu}_{90\%}(N_b)$ is given by:

$$\bar{\mu}_{90\%}(N_b) = \sum_{n_{obs}=0}^{\infty} \bar{\mu}_{90\%}(n_{obs}, N_b)\frac{(N_b)^{n_{obs}}}{(n_{obs})!}e^{-N_b} \tag{6.6}$$

where n_{obs} is the number of observed experimental events. We calculate the average upper limit, by applying the Feldman-Cousins method [FC98]. The average upper limit for shower observation $\bar{\mu}_{90\%}(N_b)$ is independent of the information from experimental data and, therefore, it does not introduce a bias on the selection criteria. The optimal cut on the energy estimator ρ is obtained by minimizing the so-called *Model Rejection Factor* (MRF) [HR03] $\bar{\mu}_{90\%}(N_b)$:N_s in equation 6.5, i.e. the ratio of the average upper limit for shower observation and the expected number of showers.

Figure 6.12 presents the average upper limit $\bar{\Phi}_{90\%}$ as function of the energy estimator ρ for the KNN (top) and the BDT (bottom) methods. The optimisation results in optimal cuts on $log_{10}(\rho)$ at 4.4 and 4.7 for the KNN and the BDT methods, respectively, providing an equal average upper limit $\bar{\Phi}_{90\%} = 1.04 \times 10^{-7}\text{GeVcm}^{-2}\text{s}^{-1}\text{sr}^{-1}$ for both methods.
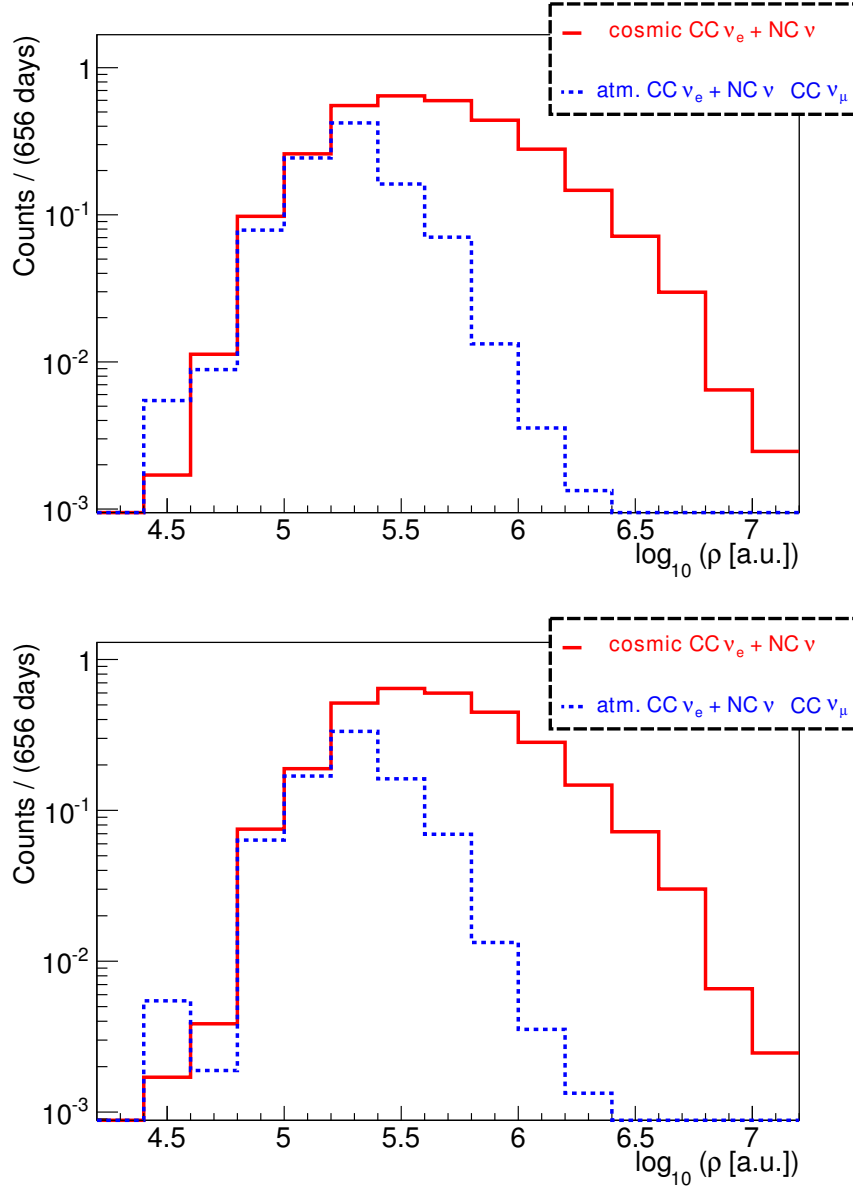
Figure 6.11: Distribution of the energy estimator ρ for atmospheric neutrinos (dashed (blue) histogram) and cosmic neutrino-induced showers (solid (red) histogram) after cut-doublets (600 p.e., 0.27) and (658 p.e., -0.09) for the KNN (top) and BDT (bottom) methods, respectively.

6.5 Experimental Data-MC Comparison

As described in section 4.5.3, we have selected a limited number of experimental runs, taken in 2008-2010, corresponding to a total livetime of 26 days in order to perform data-MC comparisons (see section 4.5.4).

Figure 6.13 compares the distributions of the total deposited charge for the MC atmospheric muon samples (solid (blue) histogram) and the experimental data (cross markers), remaining after a cut on the KNN (top) and BDT (bottom) scores of 0.27 and -0.09, respectively. The flux of the MC samples is scaled down corresponding to the livetime of the experimental data, i.e. 26 days. The mean
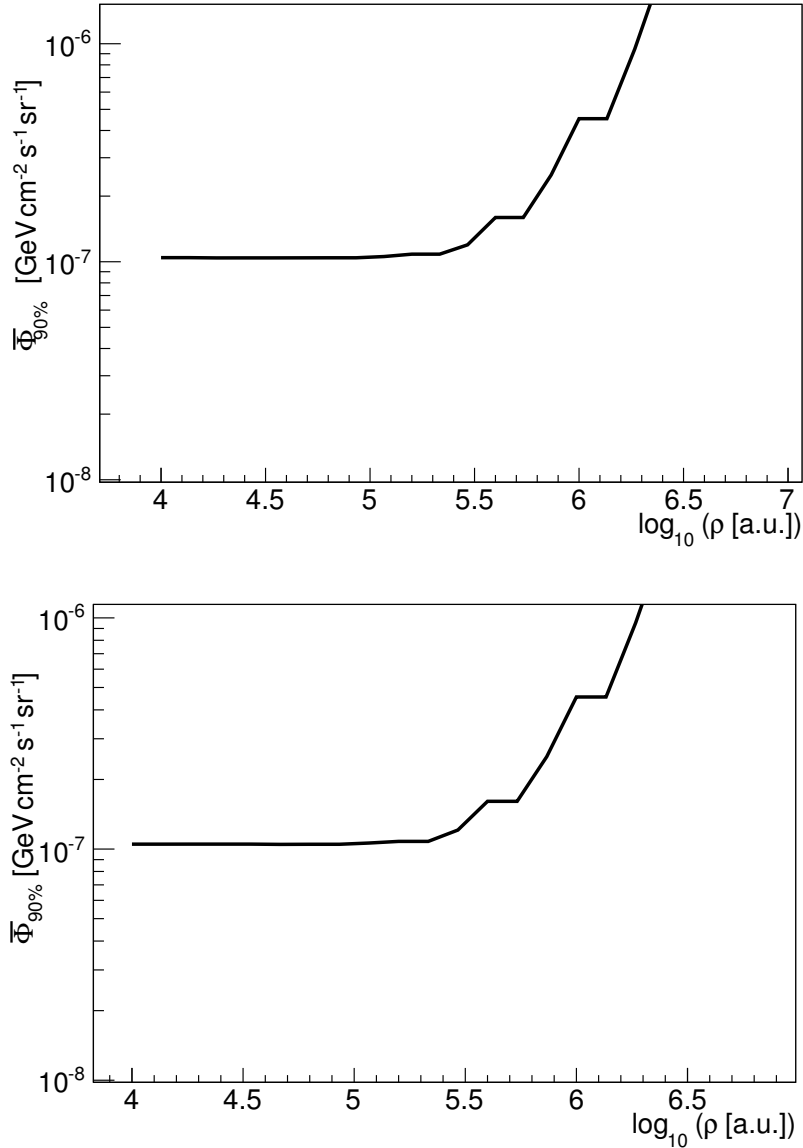
Figure 6.12: Average upper limit $\bar{\Phi}_{90\%}$ as function of the energy estimator ρ for KNN (top) and BDT (bottom) methods.

ratio of the experimental data and MC is 0.98 ± 0.25 and 0.9 ± 0.28 for the KNN and the BDT method, respectively, and the average of both ratios is 0.94 ± 0.19. An exponential function is fitted to both the MC and experimental data samples. The slopes of the exponential functions fitted to the experimental data sample are 16% (for the KNN method) and 17% (for the BDT method) steeper than the slopes of the exponential functions fitted to the MC sample. The effect of this discrepancy on the expected number of events will be discussed and estimated in section 6.6.3.
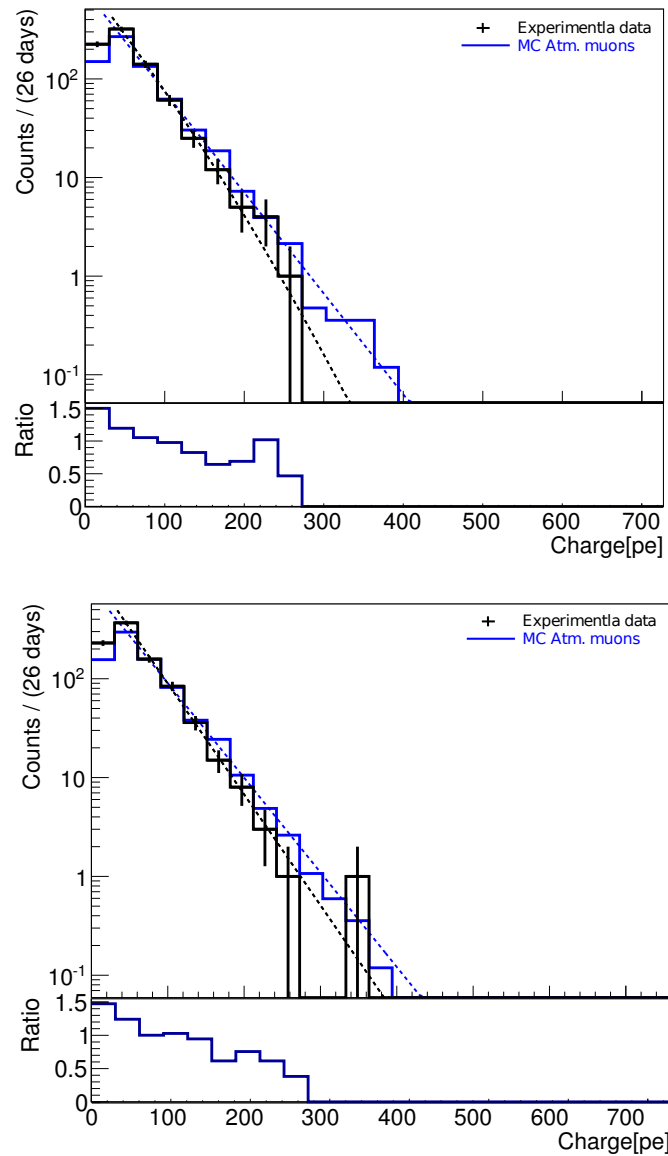
Figure 6.13: Distributions of total deposited charge per event after an applied cut on MVA scores of 0.27 and -0.09 for KNN method (top) and the BDT method (bottom) for experimental data (solid (black) histogram), MC atmospheric muons (solid (blue) histogram). The inset shows the ratio of data and MC per each bin.

6.6 Systematic Uncertainties

This section discusses the major sources of systematic uncertainties which may effect the estimation of the upper limit of the diffuse flux of cosmic neutrinos. Three categories of systematic uncertainties can be recognised: the acceptance of the detector, systematic uncertainties in the MC simulations and the uncertainties in the reconstruction and the selection criteria (cut efficiencies).

6.6.1 Acceptance of the Detector

The acceptance of the detector is defined as the constant ratio between the number of neutrino events and a neutrino flux strength ϕ_0. The acceptance can be a function of different detector parameters such as detector configuration, calibration of time and charge, efficiency of OMs. The configuration of the ANTARES neutrino telescope has been changed several times in the period from 2008 to 2010. The variations in the detector configuration can result in significant effects on the detector response. In order to eliminate any influence of the configuration on the obtained data, the ANTARES collaboration has released simulation data sets in which the configuration and the status of the detector is updated for each data-taking run. The simulation data set is called Run-by-Run simulation which is described in section 4.4. Several detector parameters, including the time and charge calibrations, are read from the data-taking databases and applied in the simulation. In order to minimise the systematic uncertainties imposed by the calibrations and detector configuration, we have only selected the experimental runs for which the Run-by-Run simulation was available.

The efficiency of the OMs and its effect on the acceptance of the detector is studied in [AM+12]. A comparison between the atmospheric neutrino data and a simulation was performed in which a systematic uncertainty of 15% was assigned to the acceptance for signal neutrinos following a spectrum with an E^{-2} energy dependence.

6.6.2 Uncertainties in the MC Simulation

The major sources of uncertainties in the MC simulation originate from theories describing the neutrino cross section, models predicting the event fluxes, light scattering in water and the model describing the optical background in the sea water. The neutrino cross section at high energies is uncertain. An analysis performed in [GQRS96] has obtained the uncertainty for the neutrino cross section for energies up to 10^{21} eV. The uncertainty for our energy range of interest, i.e. below 10^8 GeV, is less than 5%.

The simulation of the atmospheric muon background is affected by the uncertainties in the predictions for the flux and the composition of the primary cosmic rays. An uncertainty of 50% on the flux of the atmospheric muon background has been estimated using the ANTARES measurements for down-going muon events [A+10b]. The uncertainty in theoretical predictions for the primary atmospheric neutrino flux has been estimated in [BRGS06] and results in an uncertainty of 30%.

As described in section 4.2.1, the light scattering was not taken into account for the neutrino simulations used in this analysis. Scattered light can lead to the production of indirect photons from the trajectories of charged secondary particles induced by neutrinos. These indirect photons, therefore, can cause photons which produce late hits in optical modules, which may deteriorate the quality of the reconstruction of the shower parameters. An investigation, performed in [Fol], shows that the effect of light scattering is only significant at energies above 10^8 GeV (which is above our sensitive energy range).

The model, which has been exploited to simulate the optical background in sea water (see section 3.5), relies on the simplified assumption that optical back-

ground causes a random hit in the detector. Any deviation from a random model for optical background may have an influence on the shower reconstruction and, consequently, on the selection criteria. The uncertainties caused by the environmental background can be investigated by comparing experimental data and the MC simulation. In the next section we will evaluate the uncertainty in the MC simulation by comparing 5% of the experimental data, analysed before unblinding, with the full MC simulation.

6.6.3 Cut Efficiencies

As discussed in section 6.5, the slope of the exponential function fitted to the 5% of the experimental data is steeper than that fitted to the MC atmospheric muons. Considering the livetime of the 5% of the experimental data, i.e. 26 days, the majority of the observed events should be atmospheric muons. Therefore, this discrepancy should be due to the contribution of systematic uncertainties which have an effect on the selection criteria. In order to calculate these uncertainties, we have relaxed the charge cut by 16% and 17% for the KNN and BDT methods, respectively, in order to achieve the same significance for the softer charge spectrum of the experimental data, as obtained for the MC simulation in section 6.4.1. In order to estimate the systematic uncertainties imposed by the optimised charge cuts, we scanned the charge cut in the regions [510 p.e., 600 p.e.] and [546 p.e., 658 p.e.] for KNN and BDT, respectively. Then we estimated the number of neutrino signal and background events after each charge cut. Using the order statistics [1], we have estimated the upper bound, central value and lower bound of the neutrino events according to the values of the first, second and third quantiles.

This method results in the numbers and error bounds of signal and background neutrinos of $3.42^{+0.16}_{-0.22}$ and $1.5^{+0.27}_{-0.2}$, respectively, for the KNN method and the numbers of signal and background neutrinos of $3.25^{+0.15}_{-0.1}$ and $1.1^{+0.3}_{-0.1}$, respectively, for the BDT method.

6.6.4 Uncertainty on the Number of Signal Neutrinos

Unfortunately the simulation of τ neutrinos has not been included in the ANTARES simulation tools, although it is expected that τ neutrinos will have a significant contribution in the cosmic neutrino signal. The upper limit on the diffuse flux of neutrinos may improve since τ neutrinos only contribute in the neutrino signal and not in the neutrino background. As discussed in section 3.6, the track length of the induced τ lepton in water is shorter than 10 m for neutrino energies below a few PeV. Therefore, a τ neutrino event would resemble a neutrino-induced shower event, since the leptonic track of the τ neutrino interaction is too short to be resolved.

In this section, we estimate the uncertainty imposed by the absence of τ-neutrino events in the simulation sample. One can define the parameter $\Delta S / S$ as the relative difference between the reduced number of signal neutrinos $S = N_{\nu_\mu} + N_{\nu_e}$ and the number of signal neutrinos with the presence of τ-neutrino events $S' = N_{\nu_\mu} + N_{\nu_e} + N_{\nu_\tau}$:

---

[1]The kth-smallest value of a statistical sample is called the kth order statistics.

$$\frac{\Delta S}{S} = \frac{S' - S}{S} = \frac{N_{\nu_\tau}}{N_{\nu_\mu} + N_{\nu_e}}. \tag{6.7}$$

For the ANTARES sensitive energy range, i.e. 100 GeV – 1 PeV, we can expect that the largest contribution from ν_τ in the number of signal neutrinos will be approximately the same as the contribution from ν_e. Therefore, $\Delta S/S$ can be approximated as:

$$\frac{\Delta S}{S} \approx \frac{N_{\nu_e}}{N_{\nu_\mu} + N_{\nu_e}} = 0.85 \tag{6.8}$$

$\Delta S/S$ can be associated with the Full Width at Tenth of Maximum (FWTM) of a half normal distribution with a width of σ:

$$FWTM = 2\sqrt{2ln10}\sigma = 0.85 \tag{6.9}$$

resulting in $\sigma \approx 0.2$. Therefore, an uncertainty of about 20% on the number of signal neutrinos is imposed by the absent of tau-neutrino events in the signal neutrino events.

6.6.5 Total Systematic Uncertainties

Using the information presented in the previous sections, we evaluate the total contribution of the systematic uncertainties. Adding the errors in quadrature, separately for the upper and lower error bounds, the numbers of expected signal and background neutrinos are $3.42^{+0.9}_{-0.6}$ and $1.5^{+0.57}_{-0.54}$, respectively, for the KNN method and the numbers of expected signal and background neutrinos are $3.25^{+0.85}_{-0.52}$ and $1.1^{+0.5}_{-0.38}$, respectively, for the BDT method.

Table 6.3 summarises the systematic uncertainties.

Systematic uncertainties	atm. μ	atm. ν	signal ν
Acceptance	15%	15%	15%
Theoretical uncertainties	50%	30%	5%
cut efficiency			
KNN	-	$+18\%$ -13%	$+5\%$ -7%
BDT	-	$+27\%$ -9%	$+5\%$ -3%
Signal neutrino uncertainty	-	-	$+20\%$ -0%
Total uncertainties			
KNN	52.2%	$+38\%$ -36%	$+26\%$ -17%
BDT	52.2%	$+43\%$ -35%	$+26\%$ -16%

Table 6.3: Systematic uncertainties for the atmospheric muons and the atmospheric and signal neutrinos.

Results

When I want to understand what is happening today or try to decide what will happen tomorrow, I look back.

Omar Khayyam

7.1 Rejection of Sparking Events

As described in section 3.7, some very rare events are recorded by the ANTARES detector which are caused by sparking PMTs. These events typically consist of an anomalously large number of hits (see figure 3.11), so that these events can mimic the interactions of high-energy neutrinos. Methods have been developed to identify sparking runs [Pre11, Cor]. The methods reject events which resemble a point-like source of light which is located close to an OM. However, a high-energy shower event appearing close to an OM might also be excluded, since it can be misidentified as a sparking event. Therefore, we have developed a new method to exclude the sparking events. This section studies the potential of our selection strategy for rejecting any remaining sparking events.

In order to study the sparking events, we have analysed the runs identified as sparking runs [colb]. Figure 7.1 shows the distribution of the residual R (see section 5.1.1) as a function of the M-Estimator fit quality parameter M (see section 5.1.2) for events in the sparking runs. The shower region defined in section 6.2 is marked by the dashed (red) rectangle. The distribution shows an anomalous second dense region most likely due to the sparking events. The sparking events reveal a marked asymmetric topology because of the large values of R and M.

Table 7.1 summarises the number of events in the sparking runs passing each selective cut defined in the previous chapter. No sparking event has passed the selective cuts.

7.2 Final Experimental Data Samples

In the previous chapter, the ANTARES sensitivity for a diffuse flux of neutrino-induced showers was estimated for a livetime of 656 days, using Run-by-Run simulation samples (see section 4.5). We have analysed ANTARES experimental data taken from January 2008 to December 2010 corresponding to a livetime
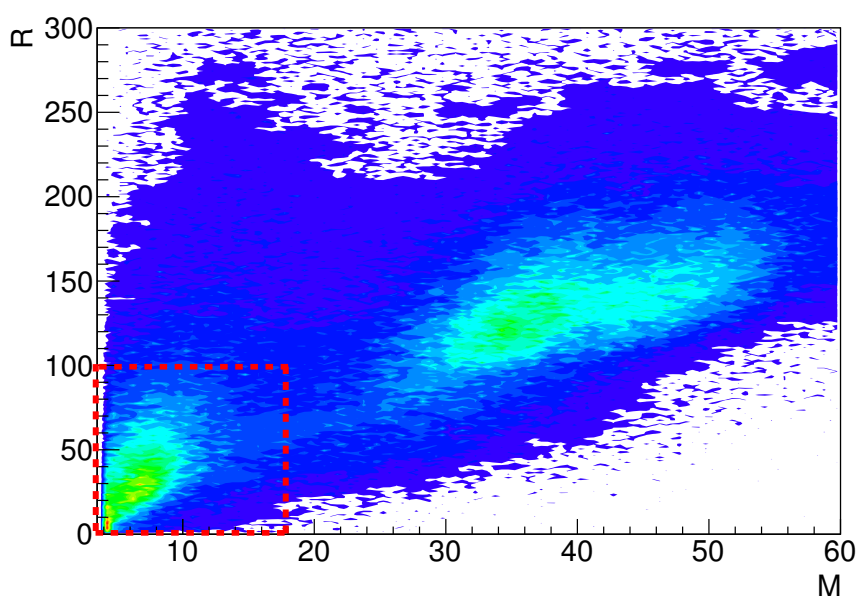
Figure 7.1: The distribution of the residual R as a function of the M-Estimator fit quality parameter M for events in the sparking runs. The distribution includes up-going and down-going events. The shower region is marked by the dashed (red) rectangle. The colour code represents the intensity from high to low by red to white.

cut	events in the sparking runs
no cut	657418
up-going	3792
$M < 18$ and $R < 100$	28
KNN score > 0.27	15
BDT score > -0.09	18
$Charge > 600$ p.e.	0

Table 7.1: Number of events in the sparking runs left after each consecutively applied selective cut.

of 656 days. During this period, the configuration of the detector has changed several times. In addition, the environmental conditions can significantly vary season by season. Therefore, it is very important to study the consistency of the response of the detector in different periods. For this reason, we have subdivided the data sample into six samples, i.e. each year into two samples: January-June

and July-December. Table 7.2 summarises the data samples. We have selected all the runs for which the Run-by-Run MC simulations are available. In addition we have excluded the known sparking runs.

sample	duration	run number	livetime (days)
S1	Jan. 2008 - Jun. 2008	31049-35075	130.5
S2	Jul. 2008 - Dec. 2008	35147-38230	76.2
S3	Jan. 2009 - Jun. 2009	38233-41626	91
S4	Jul. 2009 - Dec. 2009	41628-45536	130.1
S5	Jan. 2010 - Jun. 2010	45538-49766	105.2
S6	Jul. 2010 - Dec. 2010	049770-54250	122.8

Table 7.2: The analysed experimental dataset has been divided into six sub-samples as defined in section 7.2.

Figures 7.2 shows the distributions of total deposited charge per event after cuts on KNN score (top) and BDT score (down) of 0.27 and -0.09, respectively, for the experimental data samples S1, S2, S3 and S4 (see table 7.2). Events shown in the figure have passed all the pre-selection cuts defined in sections 6.1 and 6.2. In order to compare the event ratios per each charge bin, all the data samples are scaled to S1. The inset panels show the mean ratio (solid (blue) curve) between the data samples. The blue band shows the spread around the mean ratio. The mean ratio is around 1 over the sensitive charge range, which indicates that the response of the detector is consistent for the selected events.

Figure 7.3 compares distributions of the total deposited charge for the MC atmospheric muon sample (solid (blue) histogram) and the experimental data (markers), remaining after a cut on KNN (top) and BDT scores (bottom) of 0.27 and -0.09, respectively. The experimental data sample is the sum of the data described in table 7.2, corresponding to a total livetime of about 656 days. The MC atmospheric muon sample consists of Run-by-Run simulations corresponding to each experimental run selected for the experimental data sample. The inset panels show the ratio between the experimental data events and MC atmospheric muon events per each charge bin. The average data-MC ratios are 71% $\pm$ 0.21 and 68% $\pm$ 0.3 for KNN and BDT methods, respectively. This deviation between the data and MC was studied in section 6.6 and the effect on the systematic uncertainty was evaluated.
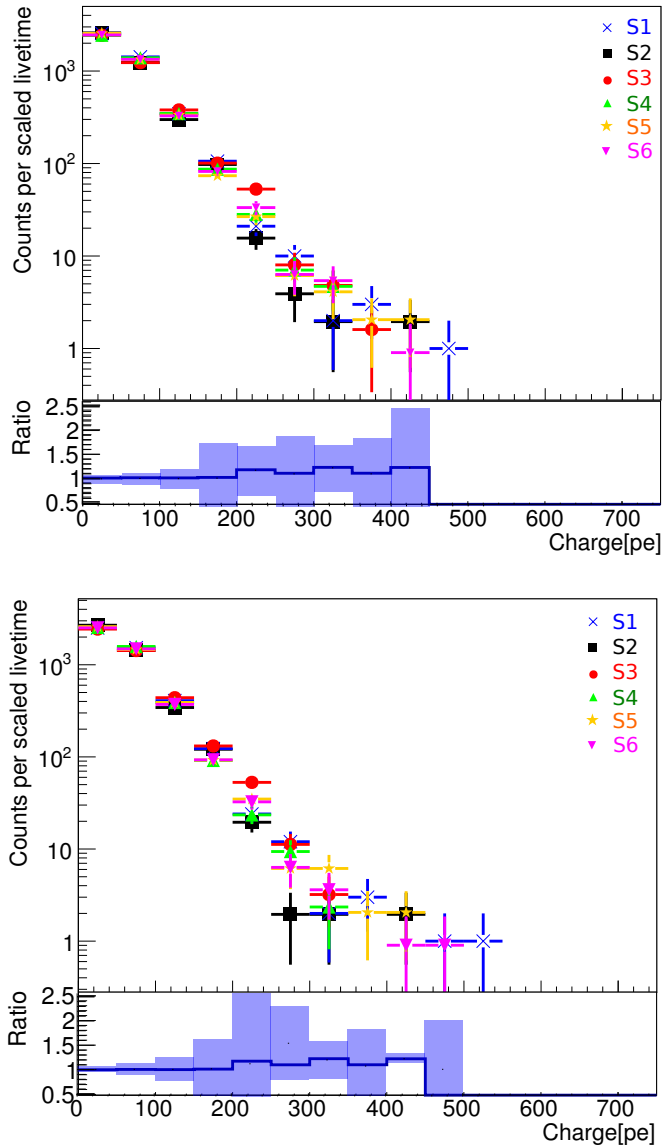
Figure 7.2: Distributions of the total deposited charge per event after a cut on MVA scores of 0.27 and -0.09 for the KNN method (top) and the BDT method (bottom) for experimental data samples S1, S2, S3, S4, S5 and S6 defined in table 7.2. The inset panels show the mean ratio between the data samples. The blue band shows the 1σ spread around the mean ratio.

7.3 Limit on the Diffuse Flux of Neutrinos

In the previous chapter we estimated the ANTARES sensitivity for the detection of showers induced by a diffuse flux of cosmic neutrinos by estimating the expected rates for signal and background events after the selection criteria, using the Run-by-Run MC simulations.

In this section, we will analyse the event rates for signal and background after each selective cut and compare them to the event rate for the experimental data sample corresponding to a livetime of 656 days. Based on this analysis, we will determine the upper limit for a diffuse flux of cosmic neutrino-induced showers.
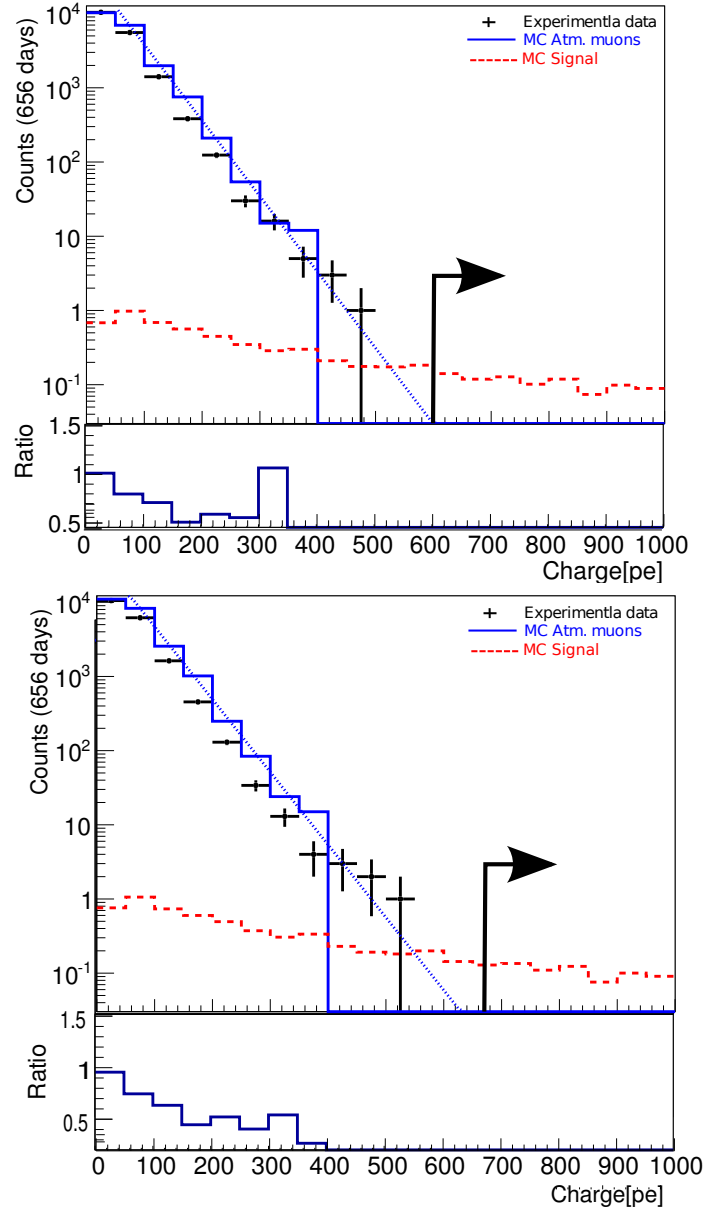
Figure 7.3: Distributions of total deposited charge per event for experimental data, MC atmospheric muon and MC signal neutrino data after KNN (top) and BDT (bottom) cuts of 0.27 and -0.09, respectively. An exponential function has been fitted to the distribution of the MC atmospheric muons. The arrow indicates the value of the optimal charge cut. The inset panels show the ratio of experimental events and MC muon events per each charge bin.

Table 7.3 summarises the number of events remaining after each consecutively applied selective cut. In the table, *atm. ν* and *signal ν* denote the sum of expected CC interactions of ν_e and ν_μ as well as the sum of NC interactions of ν_e and ν_μ for atmospheric and signal neutrinos, respectively. After all cuts, an average number of $1.3^{+0.38}_{-0.35}$ background neutrinos for both the KNN and BDT methods are expected from the atmospheric neutrino flux (see section 6.4.2) and

$3.34^{+0.62}_{-0.42}$ signal neutrinos are expected from the diffuse flux of cosmic neutrinos defined in equation 6.4. The upper and lower bounds on the expectation values of signal and background are estimated according to the systematic error study in section 6.6. On the other hand, no experimental event remains after all cuts which is consistent with the expected number of events from atmospheric neutrino background. Using the Feldman-Cousins method [FC98] (see section 6.4.2), the upper limit at 90% confidence level for the diffuse flux of cosmic neutrinos ($\nu_\mu + \nu_e + \nu_\tau$) according to the observed and expected numbers of events is obtained:

$$E[GeV]^2 \bar{\Phi}_{90\%} < 2.53^{+0.42}_{-0.32} \times 10^{-7} \text{GeVcm}^{-2}\text{s}^{-1}\text{sr}^{-1} \tag{7.1}$$

In this calculation, we considered the neutrino flavour ratio of ($\nu_\mu : \nu_e : \nu_\tau = 1 : 1 : 1$) at the Earth. The equivalent diffuse flux upper limit on each individual neutrino flavour is obtained:

$$E[GeV]^2 \bar{\Phi}^i_{90\%} < 0.84^{+0.14}_{-0.11} \times 10^{-7} \text{GeVcm}^{-2}\text{s}^{-1}\text{sr}^{-1} \tag{7.2}$$

Figure 7.4 presents the energy spectra for background and signal neutrinos remaining after the selection criteria for KNN (top) and BDT (bottom) methods. 95% of the expected cosmic signal neutrinos have energies between 3.1 TeV and 1 PeV.

Figure 7.5 compares the ANTARES shower sensitivity (656 days) with other experiments for a diffuse flux of high-energy cosmic neutrinos with an E^{-2} energy spectrum. All the measurements have been normalised to one neutrino flavour. The obtained upper limit on the diffuse flux of neutrino reaches the predicted neutrino flux in a model describing the pγ interactions in Blazar jets [Man95].

7.4 Conclusion

We have developed a method to largely suppress the overwhelming background and reconstruct neutrino-induced showers by combining selective cuts on the observables describing the event direction and topology. We have optimised the selection criteria in order to maximise the ANTARES sensitivity for the observation of showers induced by a diffuse flux of cosmic neutrinos with an E^{-2} spectral shape. The selection criteria suppress the background by 8 orders of magnitude, whereas showers are selected with an efficiency of several percent. We have applied the method in order to search for cosmic neutrinos, unblinding the ANTARES experimental data corresponding to a total livetime of 656 days. Despite the smaller volume of the ANTARES detector, this result is compatible with the world's best upper limit on the diffuse flux of neutrino-induced showers measured by the IceCube 79-string configuration [col13], scaled to one neutrino flavour, i.e. $E[GeV]^2 \bar{\Phi}^{IC}_{90\%} < 0.23 \times 10^{-7} \text{GeVcm}^{-2}\text{s}^{-1}\text{sr}^{-1}$. In addition, our obtained limit on the Southern Sky is complementary to the IceCube limit on the Northern Sky, such that the combination of both results provides a consistent upper limit for the full Sky. However, the flux upper limit that we have determined is only a factor of about 4 above the Waxman and Bahcall upper limit on the cosmic neutrinos [WB98], i.e. $E[GeV]^2 \Phi^{WB} < 2 \times 10^{-8} \text{GeVcm}^{-2}\text{s}^{-1}\text{sr}^{-1}$. Running the analysis on a larger dataset with a total livetime larger than four years may improve the flux upper limit of neutrino-induced showers by a factor of about

cut	atm. μ $\times 3$	atm. ν	signal ν	experimental data
no cut	86765823	4194.5	280.2	84187765
up-going	344007	2470.9	105.7	366667
$M < 18$ and $R < 100$	39219	633.5	21.7	30408
CAN size $<$ ANTARES radius + 60 m	34563	490	14.5	27082
KNN score > 0.27 BDT score > -0.09	20244 23268	400 495	12.5 13	17919 19000
Charge > 600 p.e. (KNN) Charge > 658 p.e. (BDT)	0 0	1.5 1.2	3.5 3.4	0 0
$log_{10}(\rho) > 4.4$ (KNN) $log_{10}(\rho) > 4.7$ (BDT)	0 0	1.5 1.1	3.42 3.25	0 0

Table 7.3: Number of events after each consecutively applied selective cut.

two, thus approaching the Waxman and Bahcall limit very closely. In that region of sensitivity, the theoretical models of neutrino production may be constrained.
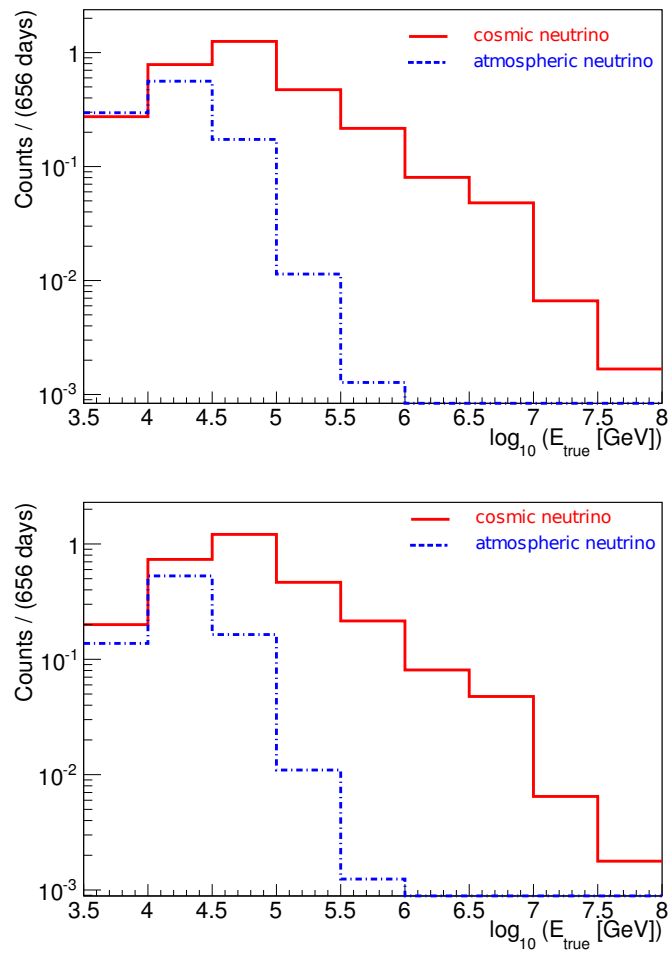
Figure 7.4: Energy spectrum of neutrinos remaining after the selection criteria for MC atmospheric (dashed (blue) histogram) and signal (solid (red) histogram) neutrinos.
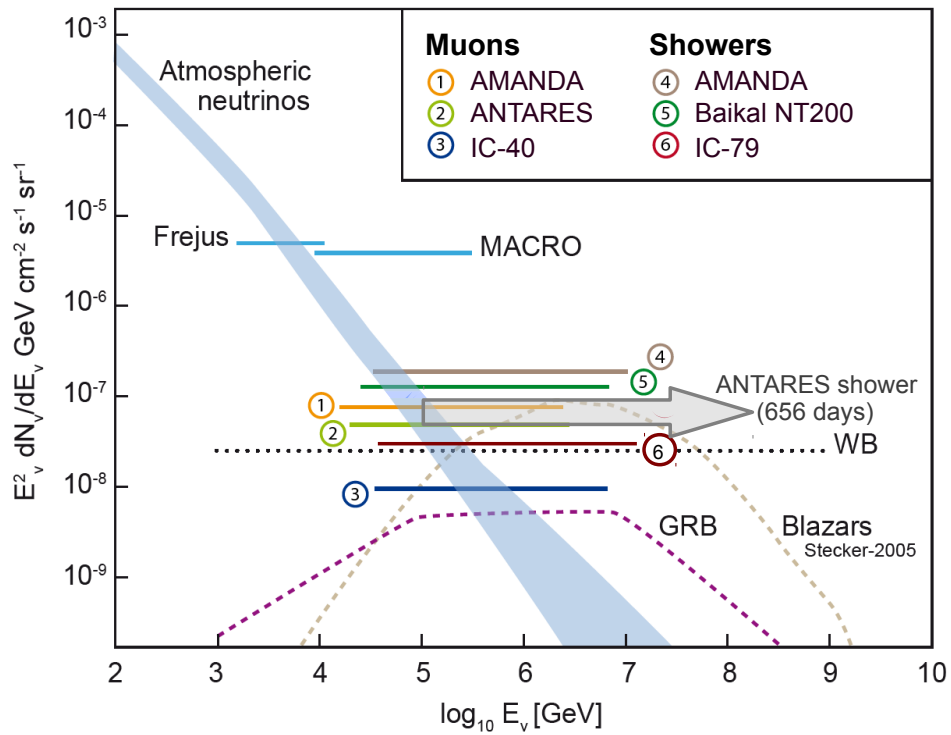
Figure 7.5: The upper limits on the E^{-2} diffuse flux of cosmic neutrinos at 90% confidence level. The (gray) arrow marks the sensitivity of the ANTARES detector for detection of high-energy neutrino-induced showers. For more detail about the entries in the figure, see section 2.5.

Chapter

Summary and Outlook

This dissertation reports on measurements and the corresponding data analysis, which was designed to reconstruct and identify neutrino-induced showers in the ANTARES neutrino telescope. The reconstruction of such showers, which are recognised by their local light production, can protrude the sensitivity of a neutrino telescope to all neutrino flavours. Moreover, showers are well-contained events in the detection volume. This characteristic of showers allows for a better energy estimation compared to muon tracks induced by muon neutrinos. In this analysis, we aimed at the reconstruction of a complete set of shower parameters, i.e. the space-time position, energy and direction of neutrino-induced showers. We have exploited and combined two independent event reconstruction algorithms in order to obtain the precise estimation of the shower parameters. A necessary prerequisite for a successful analysis strategy is to efficiently suppress the background of atmospheric muons. We have chosen for defining and combining selection criteria for observables describing the directions and topologies of shower-candidate events. We applied a multivariate data analysis (MVA) in order to efficiently combine the selective cuts and to express them as one discriminating variable. In order to cross-check the final result, we have exploited two independent MVA methods, the *K-Nearest Neighbour* and the *Boosted Decision Tree*. The final shower selection strategy is based on stepwise selection criteria expressed by three final cuts, i.e. total deposited charge per event, the MVA score and the energy estimator ρ. First we optimise a cut-doublet on total deposited charge per event and a MVA score in order to largely suppress the contamination of atmospheric muons in selected shower samples. The optimal cut-doublet selects neutrino-induced showers from atmospheric muons with a purity better than 99%. Finally, we select cosmic showers among the background of atmospheric neutrinos by optimising a cut on the energy estimator ρ. The optimisation procedure relies on the minimization of the value of the average upper limit of the diffuse flux $\bar{\Phi}_{90\%}$ of cosmic neutrinos, under the assumption of no shower-signal observation. In order to avoid a possible bias in the selection criteria, we have exploited a blind analysis using only 5% of the ANTARES experimental data taken in the period 2008-2010. This blind analysis aimed to verify the consistency of the experimental data and MC simulations, as well as to provide the estimation of the systematic uncertainties. After the selection criteria were finalised, the analysis was unblinded. We have run the analysis on 656 days of the ANTARES experimental data in the period January 2008 to December 2010. The average number of $3.34^{+0.62}_{-0.42}$ and $1.3^{+0.38}_{-0.35}$ signal and background neutrinos, respectively,

are expected after the selection criteria from the diffuse flux of cosmic neutrinos defined in equation 6.4. On the other hand, no experimental event has passed the selection criteria, which is consistent with the background expectation; therefore, we have determined the upper limit on the expected signal of cosmic neutrinos. Assuming a flavour ratio ($\nu_\mu : \nu_e : \nu_\tau = 1 : 1 : 1$) at the detector site and an E^{-2} spectral shape, our estimation for the upper limit on the diffuse cosmic neutrino ($\nu_\mu + \nu_e + \nu_\tau$) flux at the 90% C.L. is:

$$E[GeV]^2 \bar{\Phi}_{90\%} < 2.53^{+0.42}_{-0.32} \times 10^{-7} \text{GeVcm}^{-2}\text{s}^{-1}\text{sr}^{-1} \tag{8.1}$$

This value is equivalent to a limit of $E[GeV]^2 \bar{\Phi}^i_{90\%} < 0.84^{+0.14}_{-0.11} \times 10^{-7} \text{GeVcm}^{-2}\text{s}^{-1}\text{sr}^{-1}$ on each individual neutrino flavour. 90% of the expected neutrino signals have energies between 3.1 TeV and 8 PeV. Despite the smaller volume of the ANTARES detector, this result is close to the world's best upper limit on the diffuse flux of neutrino-induced showers measured by the IceCube detector [col13], i.e. $E[GeV]^2 \bar{\Phi}^{IC}_{90\%} < 0.23 \times 10^{-7} \text{GeVcm}^{-2}\text{s}^{-1}\text{sr}^{-1}$. In addition, our obtained limit on the Southern Sky is complementary to the IceCube limit on the Northern Sky, such that the combination of both results provides a consistent upper limit for the full Sky.

Our limit is only a factor of about 4 above the Waxman and Bahcall upper limit on the cosmic neutrinos [WB98], i.e. $E[GeV]^2 \Phi^{WB} < 2 \times 10^{-8} \text{GeVcm}^{-2}\text{s}^{-1}\text{sr}^{-1}$. Running the analysis on a dataset with a total livetime larger than four years may improve the flux upper limit of neutrino-induced showers to a value of $E[GeV]^2 \bar{\Phi}^i_{90\%} < 0.35 \times 10^{-7} \text{GeVcm}^{-2}\text{s}^{-1}\text{sr}^{-1}$, which may provide constraints for theoretical models of neutrino production.

Perspective for the Km3NeT Neutrino Telescope

The future deep-sea neutrino telescope of multi cubic-km size, KM3NeT [B$^+$11], has been designed for an efficient search for high-energy neutrinos originating from galactic and extragalactic sources. The detection of cosmic neutrinos may provide us with yet concealed information about non-thermal processes in the Universe. Based on the experience of the pilot projects ANTARES, NEMO [C$^+$09] and NESTOR [Rap09], the KM3NeT collaboration plans to equip an active detection volume at the bottom of the Mediterranean Sea with an array of digital optical modules (DOMs), i.e. only digital information will be sent from a DOM to shore for further analysis (see figure 8.1). The direction and energy of neutrinos can be inferred from a precise determination of DOM position, arrival time and total detected charge. For the identification of point-like neutrino sources an angular resolution better than 0.3° can be provided for neutrino energies above 10 TeV.

In addition to Cherenkov photons originating from charged tracks or hadronic showers caused by neutrinos, a DOM is exposed to a random optical background which is due to the decay of radioactive isotopes and biological processes in sea water (see section 3.5). In ANTARES, each photo sensor of 10-inch diameter measures typically a pulse rate of 60 - 100 kHz, mostly single photo electrons produced by ^{40}K decay ($\approx$40 kHz) and by the bioluminescence from the deep-sea fauna causing a constant contribution with occasional bursts of much higher
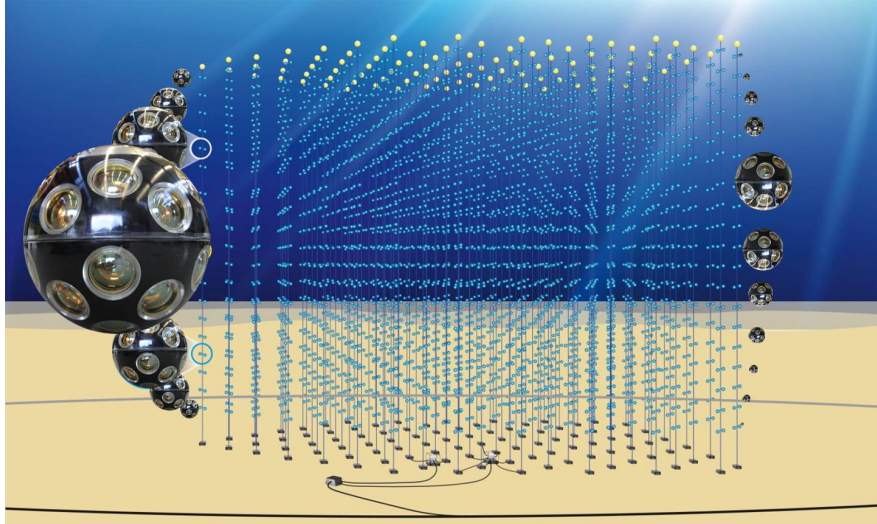
Figure 8.1: Artist's impression of the KM3NeT neutrino telescope equipped with DOMs. The figure is taken from [cold].

intensity. These uncorrelated signals are suppressed by requiring local coincidences in nearby photo sensors on each floor of the detector array and a certain minimum number of photon hits on several floors [H+12]. In order to improve the local optical-background rejection, a multi-PMT DOM (figure 8.2) housing 31 3-inch PMTs has been developed and proposed in the KM3NeT Technical Design Report [B+df]. The multi-PMT DOM has a number of advantages compared to an optical module (OM) housing a single large PMT, such as a smaller transit time spread, a longer lifetime, and a better two-photon separation [AM+13, Arb10] in addition to a simplified charge determination by counting the number of fired PMTs. Small PMTs do not require magnetic shielding, since they are much less sensitive to the Earth's magnetic field. Moreover a multi-PMT DOM has a higher reliability compared to a single-PMT OM, since failure of one small PMT has a limited effect on its total performance.

In addition, a detector equipped with multi-PMT DOMs may provide a better direction estimation for down-going atmospheric muons, since the sensitive area of the multi-PMT DOM is also extended to its upper hemisphere. Misidentified down-going atmospheric muons present the most severe background for the detection of neutrino-induced showers. As proposed in this dissertation, a way to efficiently reject the atmospheric muons is to select up-going events by exploiting cuts on the event direction. Therefore, a multi-PMT DOM detector may measure neutrino-induced showers providing a higher sensitivity.

The other main advantage of KM3NeT compared to ANTARES stems from its larger detection volume, i.e. a 100 times larger size. A larger detection volume increases the effective area (see section 4.1), which may eventually lead to a higher detection rate for signal neutrinos. Assuming the same detection efficiency as ANTARES, one can expect that the sensitivity of the KM3NeT detector for 1 year of data taking may exceed a sensitivity level of $E[GeV]^2\bar{\Phi}_{90\%}^{KM3} < 10^{-8}\mathrm{GeVcm^{-2}s^{-1}sr^{-1}}$, where the limit is mainly determined by the background level. Therefore, the potential of the detection of neutrino-induced showers with KM3NeT is very promising. However, sensitivity studies on a certain configu-
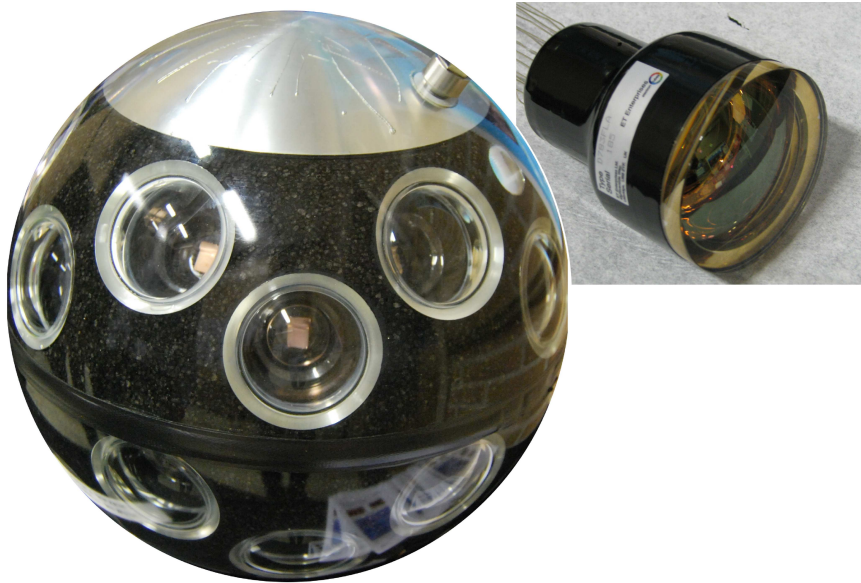
Figure 8.2: Prototype of the multi-PMT DOM with 31 3-inch PMTs arranged in a 17-inch diameter pressure glass sphere. Insert top right: the photograph of the ET Enterprises Ltd. D783FL 3-inch diameter PMT which was investigated by us and found suitable for KM3NeT [H$^+$12].

ration of KM3NeT resulted in a less accurate space-time position reconstruction for neutrino-induced showers [Zij11] as compared to ANTARES. This effect is due to a larger spacing between the DOMs chosen for the specific KM3NeT configuration, which increases the effect of light scattering in water. Therefore, the final KM3NeT configuration has to result from a carefully chosen compromise between a maximised detection volume and an optimised space-time position reconstruction.

In addition, due to the large detection volume, KM3NeT will have access to higher energies, i.e. above the PeV energy range. As discussed in section 3.6, in such an energy regime, the track component of tau-neutrino interactions can be long enough so that the double-bang event topology may be detected. Detection of tau neutrinos may furnish a measurement of the neutrino flavour ratio. The expected standard neutrino-flavour ratio on Earth is $\nu_e : \nu_\mu : \nu_\tau = 1 : 1 : 1$, assuming neutrino production through the decay of charged pions caused by interactions of high-energy protons with photons or nucleons [LP95] and taking into account neutrino oscillations. Any observed deviation from the standard neutrino-flavour ratio can either provide constraints on astrophysical models [KW05] or probe for new physics [LP95, AJY00].

Chapter

Samenvatting

Dit proefschrift beschrijft de metingen en de bijbehorende data-analyse, die werd ontwikkeld voor het reconstrueren en identificeren van neutrino geïnduceerde showers in de ANTARES neutrino telescoop. De reconstructie van zulke showers, die herkend worden aan de vrij lokale lichtproductie, kan de gevoeligheid van een neutrino telescoop uitbreiden naar alle neutrino soorten. Verder worden deze showers in het algemeen geheel opgevangen binnen de grenzen van het detectievolume. Deze eigenschap zorgt voor een betere energiebepaling vergeleken met sporen van muonen die geïnduceerd worden door muon neutrino's. De doelstelling van de hier gepresenteerde analyse was de reconstructie van een volledige set van shower parameters, namelijk de ruimte-tijd positie, de energie en de richting van neutrino's. We hebben twee onafhankelijke event reconstructie algoritmes gebruikt en gecombineerd voor de precieze bepaling van de shower parameters. Een noodzakelijke voorwaarde voor een succesvolle analyse strategie is dat de achtergrond van atmosferische muonen efficiënt kan worden onderdrukt. We hebben gekozen voor het definiëren en combineren van selectieve criteria voor observabelen, die de richtingen en topologieën van kandidaat showers beschrijven. We hebben een multivariate data-analyse (MVA) toegepast voor het efficiënt combineren van selectieve filters zodat deze door een enkele onderscheidende variabele uitgedrukt kunnen worden. Voor het verifiëren van het uiteindelijke resultaat hebben we twee onafhankelijke MVA methodes gebruikt, de "K-nearest neighbour" en de "Boosted Decision Tree". De uiteindelijke strategie voor de shower selectie is gebaseerd op het stapsgewijs toepassen van drie selectieve criteria, namelijk de totale afgegeven lading per event, de MVA score en de energie schatting ρ. Eerst optimaliseren we een dubbele filter op de totale afgegeven lading per event en de MVA score om de contaminatie van atmosferische muonen grotendeels te onderdrukken. De optimale dubbele filter selecteert neutrino geïnduceerde showers van atmosferische muonen met een zuiverheid van beter dan 99%. Tot slot selecteren we kosmische showers uit de achtergrond van atmosferische neutrino's door het optimaliseren van een filter op de energie schatting ρ. Veronderstellen wij, dat er geen shower signaal geobserveerd wordt, dan doelt de optimalisatieprocedure op de minimalisatie van de bovenlimiet voor de diffuse flux $\bar{\Phi}_{90\%}$ van kosmische neutrino's. Om een mogelijke bias in de selectiecriteria te voorkomen, hebben we een "blinde analyse" uitgevoerd op 5% van de ANTARES experimentele data uit de periode 2008-2010. De doelstelling van deze blinde analyse was om de consistentie van de experimentele data en Monte Carlo simulaties te verifiëren, alsmede om de systematische onzekerheden te schatten. Nadat de optimale selectiecriteria waren

vastgesteld, werd de analyse ongeblindeerd. We hebben de uiteindelijke analyse uitgevoerd op 656 dagen van de ANTARES experimentele data in de periode van januari 2008 tot december 2010. In totaal worden in deze dataset na de selectiecriteria $3.34^{+0.62}_{-0.42}$ and $1.3^{+0.38}_{-0.35}$ achtergrondneutrino's verwacht voor een diffuse kosmische neutrino flux zoals die in vergelijking 6.4 gedefinieerd is.

Anderzijds kon geen van de experimentele events aan de selectiecriteria voldoen, hetgeen consistent is met de verwachting van de achtergrond; daarom hebben we de bovenlimiet bepaald van het verwachte signaal van de kosmische neutrino's. Als een flavour ratio ($\nu_\mu : \nu_e : \nu_\tau = 1 : 1 : 1$) op de plaats van de detector en een E^{-2} spectrale vorm verondersteld worden, is onze schatting voor de bovenlimiet van de diffuse kosmische neutrino ($\nu_e + \nu_\mu + \nu_\tau$) flux met 90% C.L. gelijk aan:

$$E[GeV]^2\bar{\Phi}_{90\%} < 2.53^{+0.42}_{-0.32} \times 10^{-7}\text{GeVcm}^{-2}\text{s}^{-1}\text{sr}^{-1} \tag{9.1}$$

Deze waarde is equivalent aan de limiet van $E[GeV]^2\bar{\Phi}^i_{90\%} < 0.84^{+0.14}_{-0.11} \times 10^{-7}\text{GeVcm}^{-2}\text{s}^{-1}\text{sr}^{-1}$ op elk individueel neutrino flavour. 90% van de verwachte signaal neutrino's heeft een energie tussen de 3.1 TeV en 8 PeV. Ondanks het kleinere volume van de ANTARES detector is dit resultaat dichtbij 's werelds beste bovenlimiet van de diffuse flux van neutrino geïnduceerde showers gemeten door de IceCube detector [col13], namelijk
$E[GeV]^2\bar{\Phi}^{IC}_{90\%} < 0.23 \times 10^{-7}\text{GeVcm}^{-2}\text{s}^{-1}\text{sr}^{-1}$. Daarnaast is onze limiet, verkregen aan de zuidelijke hemel, complementair aan de IceCube limiet aan de noordelijke hemel, zodat de combinatie van beide resultaten een consistente bovenlimiet voor de gehele hemel geeft. Onze limiet is maar een factor 4 boven de Waxman en Bahcall bovenlimiet van kosmische neutrino's [WB98], namelijk
$E[GeV]^2\Phi^{WB} < 2 \times 10^{-8}\text{GeVcm}^{-2}\text{s}^{-1}\text{sr}^{-1}$. Als de analyse uitgevoerd wordt op een dataset met een totale effectieve meettijd van langer dan 3 jaar, kan de bovenlimiet voor de flux van neutrino geïnduceerde showers verbeteren tot een waarde $E[GeV]^2\bar{\Phi}^i_{90\%} < 0.35 \times 10^{-7}\text{GeVcm}^{-2}\text{s}^{-1}\text{sr}^{-1}$, hetgeen randvoorwaarden kan verschaffen voor theoretische modellen van neutrino productie.

Perspectief voor de Km3NeT neutrino telescoop

De toekomstige diepzee neutrino telescoop van meerdere kubieke km grootte, KM3NeT [B+11], is ontworpen voor een efficiënte zoektocht naar hogere energie neutrino's afkomstig uit galactische en extragalactische bronnen. De detectie van kosmische neutrino's kan ons tot nog toe verborgen informatie verschaffen over niet-thermische processen in het universum. Gebaseerd op de ervaring van de piloot projecten ANTARES, NEMO [C+09] en NESTOR [Rap09], is het plan van de KM3NeT samenwerking, om een actief detectievolume uit te rusten met een reeks digitale optische modules (DOM's), zodat alleen digitale informatie zal worden verzonden vanuit een DOM naar de kust voor verdere verwerking (zie figuur 8.1). De richting en energie van neutrino's kan worden afgeleid uit een precieze bepaling van de DOM positie alsmede de aankomsttijd van de gemeten signalen en de totale gedetecteerde lading. Voor de identificatie van puntachtige neutrino bronnen kan een hoek resolutie beter dan 0.3° worden bereikt voor neutrino energieën boven 10 TeV.

Naast Cherenkov fotonen, afkomstig uit sporen van geladen deeltjes of door neutrino's veroorzaakte hadronische showers, wordt een DOM blootgesteld aan een random optische achtergrond, hetgeen afkomstig is van biologische processen in zeewater (zie sectie 3.5) en van het verval van radioactieve isotopen. In ANTARES meet elke lichtsensor met 10 inch diameter een typische pulsfrequentie van 60–100 kHz. Deze signalen zijn voornamelijk afkomstig van enkelvoudige foto-elektronen geproduceerd door ^{40}K verval ($\approx$40 kHz) en door de bioluminescentie van diepzee fauna, dat een constante bijdrage veroorzaakt met sporadische uitbarstingen van veel hogere intensiteit. Deze ongecorreleerde signalen worden onderdrukt door een lokale coïncidentie te vereisen in nabij liggende lichtsensoren op elke verdieping van de reeks detectoren, alsmede een bepaald minimum aan foton treffers op verschillende verdiepingen [H$^+$12].

Om de lokale optische achtergrond meest efficiënt te onderdrukken, werd een multi-PMT DOM (figuur 8.2) met daarin 31 3-inch fotomultiplicator buizen (PMT's) ontwikkeld en voorgesteld in het KM3NeT Technical Design Report [B$^+$df]. De multi-PMT DOM heeft een aantal voordelen vergeleken met een optische module (OM) met daarin een enkele grote PMT, zoals een kleinere spreiding in de signaalverwerkingstijd, een langere levensduur en een betere twee-foton scheiding [AM$^+$13, Arb10], naast de eenvoudige ladingsschatting door het tellen van het aantal signaalgevende PMT's. Bovendien is voor kleine PMT's geen magnetische afscherming nodig aangezien ze veel minder gevoelig zijn voor het magnetische veld van de aarde. Verder is een multi-PMT DOM veel betrouwbaarder dan een OM met een enkele PMT, aangezien een storing in een kleine PMT een beperkt effect heeft op de totale prestatie.

Daarnaast kan een detector met multi-PMT DOM's de richting van neergaande atmosferische muonen veel beter aangeven, aangezien het gevoelige oppervlak van de multi-PMT DOM ook is uitgebreid naar de bovenste helft. Verkeerd geïdentificeerde neergaande atmosferische muonen representeren de meest storende achtergrond voor de detectie van neutrino geïnduceerde showers. Zoals voorgesteld in deze dissertatie, kunnen atmosferische muonen meest efficiënt onderdrukt worden door selectieve filters op opgaande events. Hierdoor zou een detector met multi-PMT DOM's de neutrino geïnduceerde showers met een hogere gevoeligheid kunnen meten.

Het andere voornaamste voordeel van KM3NeT vergeleken met ANTARES komt door zijn wel 100 maal groter detectievolume. Een groter volume verhoogt het effectieve oppervlak (zie sectie 4.1), hetgeen uiteindelijk kan leiden tot een hogere detectiefrequentie voor signaal neutrino's. Als dezelfde detectie efficiëntie, als voor ANTARES bepaald werd, wordt verondersteld, kan de gevoeligheid van de KM3NeT detector voor een meetperiode van 1 jaar beter zijn dan $E[GeV]^2\bar{\Phi}_{90\%}^{KM3} < 10^{-8}GeV cm^{-2}s^{-1}sr^{-1}$, waarbij de limiet hoofdzakelijk bepaald wordt door het niveau van achtergrond signalen. Hierdoor is de kracht van KM3NeT voor detectie van neutrino geïnduceerde showers veelbelovend. Echter, studies van de gevoeligheid van een bepaalde configuratie voor KM3NeT resulteerden in een minder accurate reconstructie van de ruimte-tijd positie voor neutrino geïnduceerde showers [Zij11] vergeleken met ANTARES. Dit effect is hoofdzakelijk te wijten aan de grotere afstand tussen de DOM's, die gekozen was om een groter volume te bereiken maar die anderzijds het effect van licht verstrooiing in het water vergroot. Wij concluderen hieruit dat de uiteindelijke KM3NeT configuratie bepaald moet worden door een zorgvuldig gekozen com-

promis tussen een gemaximaliseerd detectievolume en een geoptimaliseerde reconstructie van de ruimte-tijd positie.

Vanwege het grotere detectievolume zal KM3NeT toegang hebben tot hogere energieën, namelijk boven het PeV energiebereik. Zoals besproken in sectie 3.6, kan in een dergelijk energie regime de spoorlengte van τ neutrino interacties lang genoeg zijn, zodat de "double-bang" event topologie gedetecteerd kan worden. Een zuivere detectie van τ neutrino's kan een meting van de neutrino flavour ratio mogelijk maken. De verwachte standaard neutrino flavour ratio op aarde is $\nu_e : \nu_\mu : \nu_\tau = 1 : 1 : 1$ in de veronderstelling, dat neutrino productie veroorzaakt wordt door het verval van geladen pionen afkomstig uit interacties van hoge energie protonen met fotonen of nucleonen [LP95]; verder wordt er rekening gehouden met neutrino oscillaties. Iedere geobserveerde afwijking van de standaard neutrino flavour ratio kan of randvoorwaarden verschaffen op astrofysische modellen [KW05] of nieuwe fysica onderzoeken [LP95, AJY00].

AGN	Active Galactic Nuclei
AMANDA	Antarctic Muon And Neutrino Detector Array
ANTARES	Astronomy with a Neutrino Telescope and Abyss environmental RESearch
ARS	Analogue Ring Sampler
BDT	Boosted Decision Tree
BSS	Bottom String Socket
CC	Charged Current
DAQ	Data AcQuisition
DIS	Deep Inelastic Scattering
DOM	Digital Optical Module
FOM	Figure Of Merit
GEANT	General Event-Analysis Tools
GPS	Global Positioning System
GRB	Gamma Ray Burst
GZK	Greisen Zatsepin Kuzmin
H.E.S.S.	High Energy Stereoscopic System
KM3NeT	Cubic Kilometre Neutrino Telescope
KNN	K-Nearest Neighbour
LCM	Local Control Module
LED	Light Emitting Diode

MEOC	Main Electro-Optical Cable
MC	Monte Carlo
MVA	Multi Variate Analysis
NC	Neutral Current
OM	Optical Module
PMT	PhotoMultiplier Tube
ROOT	Rapid Object-Oriented Technology
RQPM	Recombination Quark Parton Model
SCM	Sector Control Module
SMST	Shower Mean Space Time
TMVA	Toolkit for Multi Variate Analysis
TTS	Transit Time Spread

Bibliography

[A+07]   J.A. Aguilar et al. The data acquisition system for the ANTARES neutrino telescope. *Nucl. Instr. and Meth. A*, 570:107–116, 2007.

[A+10a]   J.A. Aguilar et al. AMADEUS the acoustic neutrino detection test system of the ANTARES deep sea neutrino telescope. *accepted for publication in Nucl. Instr. and Meth., doi:10.1016/j.nima.2010.09.053*, 2010.

[A+10b]   J.A. Aguilar et al. Zenith distribution and flux of atmospheric muons measured with the 5-line ANTARES detector. *Astropart. Phys.*, 34:179, 2010.

[A+11a]   M. Ageron et al. ANTARES: the first undersea neutrino telescope. *Nuclear Instruments and Methods in Physics Research Section A*, 656:11–38, 2011.

[A+11b]   J.A. Aguilar et al. A fast algorithm for muon track reconstruction and its application to the ANTARES neutrino telescope. *Astropart. Phys.*, 34:652–662, 2011. arXiv:1105.4116.

[A+80]   E. Aliu et al. Multiwavelength Observations of the AGN 1ES 0414+009 2 with VERITAS, Fermi-LAT, Swift-XRT, and MDM. *Astrophys. J.*, 755:118, 2012, arXiv:1206.4080.

[Act08]   Oxana Actis. *Search for neutrino-induced cascades with 5 years of the AMANDA-II data*. PhD thesis, Mathematisch-Naturwissenschaftliche Fakultät I, Humboldt-Universität zu Berlin, Germany, 2008.

[AJY00]   H. Athar, M. Jezabek, and O. Yasuda. Neutrino properties from high energy astrophysical neutrinos. *Phys. Rev. D.*, 62:103007, 2000.

[AM+12]   S. Adrian-Martinez et al. Search for cosmic neutrino point sources with four years of data from the ANTARES telescope. *Astrophys. Jour.*, 760:53, 2012.

[AM+13]   S. Adrián-Martìnez et al. Expansion cone for the 3-inch PMTs of the KM3NeT optical modules. *JINST*, 8:T03006, 2013.

[And33]   C. D. Anderson. The positive electron. *Phys. Rev.*, 43:491, 1933.

[Arb10]   Jakko Arbeider. Improving the sensitivity of a new MultiPMT optical module for KM3NeT. Bachelor thesis, Rijksuniversiteit Groningen, Netherlands, 2010.

[ATftKC13] R. Coniglione A. Trovato and P. Sapienza for the KM3NeT Collaboration. KM3NeT discovery potential for galactic point-like sources. In *Proc. The 33rd International Cosmic Ray Conference, Brazil*, 2013.

[B+11]   P. Bagley et al. Technical design report for a deep-sea research infrastructure in the mediterranean sea incorporating a very large volume neutrino telescope. *ISBN 978-90-6488-033-9*, 2011.

[B+30]   G.D. Barr et al. Three-dimensional calculation of atmospheric neutrinos. *Phys. Rev. D*, 70:023006, 2004; arXiv:astro-ph/0403630.

[Bai]   D.J.L. Bailey. Genhen: Extension of genneu for high energy neutrino inter-actions. *ANTARES-SOFT-2000-005*.

[Bia10]   Simone Biagi. *Search for a Diffuse Flux of Astrophysical Muon Neutrinos in the ANTARES Telescope*. PhD thesis, University of Bologna, Italy, 2010.

[Bon]   G. De Bonis. Electron neutrinos. `http://antares.in2p3.fr/internal/dokuwiki/doku.php?id=electron_neutrinos`. website.

[BR97]   Rene Brun and Fons Rademakers. Root - an object oriented data analysis framework. *Nucl. Instrum. Meth. A*, 389:81–86, 1997.

[Bra]   J. E. Brau. Galaxies; building blocks of the universe. `http://physics.uoregon.edu/~jimbrau/astr123/Notes/Chapter24.html`. website.

[BRGS06]   G. D. Barr, S. Robbins, T. K. Gaisser, and T. Stanev. Uncertainties in atmo-spheric neutrino fluxes. *Phys. Rev. D*, 74:094009, 2006.

[Bru]   J. Brunner. Cherenkov light from HE showers. *ANTARES-Soft-2002-015*.

[B$^+$df]   P. Bagley et al. KM3NeT technical design report. 2011, ISBN 978-90-6488-033-9; http://www.km3net.org/TDR/TDRKM3NeT.pdf.

[C$^+$08]   G. Carminati et al. Atmospheric MUons from PArametric formulas: a fast GEnerator for neutrino telescopes (MUPAGE). *Phys. Commun.*, 179:915–923, 2008.

[C$^+$09]   A. Capone et al. NEMO phase 1: construction, operation and first results. *Nucl. Instrum. Meth. A*, 602:47–53, 2009.

[Cha]   HAP / A. Chantelauze. Cosmic ray mystery. `http://www.hap-astroparticle.org/184.php`. website.

[Cle98]   B. T. Cleveland. Measurement of the solar electron neutrino flux with the Homestake Chlorine detector. *Astrophys. J.*, 496:505, 1998.

[cola]   ANTARES collaboration. Known problematic runs. `http://antares.in2p3.fr/internal/dokuwiki/doku.php?id=list_of_problematic_runs`. website.

[colb]   ANTARES collaboration. Known problematic runs. `http://antares.in2p3.fr/internal/dokuwiki/doku.php?id=list_of_problematic_runs`. website.

[colc]   H.E.S.S. collaboration. Discovery of gamma rays from the edge of a black hole. `http://www.mpi-hd.mpg.de/hfm/HESS/pages/press/old/PressRelease/M87Press/PressRelease_E.html`. website.

[cold]   KM3NeT collaboration. `"http://www.km3net.org/images.php"`.

[Col05]   ANTARES Collaboration. Study of large hemispherical photomultiplier tubes for the ANTARES neutrino telescope. *Nucl. Instrum. Meth. A*, 555:132–141, 2005.

[Col10]   Pierre Auger Collaboration. Measurement of the energy spectrum of cosmic rays above 10^{18} eV using the Pierre Auger observatory. *Phys. Lett. B*, 658:239, 2010.

[Col11]   Fermi LAT Collaboration. Observations of the young supernova remnant RX j1713.7-3946 with the Fermi Large Area Telescope. *Astrophys. Journ.*, 734:28, 2011.

[col13]   IceCube collaboration. Search for extraterrestrial neutrino-induced cascades using IceCube 79-strings. In *Proc. The 33rd International Cosmic Ray Confer-ence, Rio de Janeiro*, 2013.

[Col32]   ANTARES Collaboration. A deep sea telescope for high energy neutrinos. 1999, arXiv:astro-ph/9907432.

[Cor]   Laura Core. Private communication.

[Cosv3]   C.G.S. Costa. The prompt lepton cookbook. *Astropart. Phys.*, 16:193–204, 2001; arXiv:hep-ph/0010306v3.

[Cos93]   C.G.S. Costa. Geant program manual. *CERN program library long writeup*, W5013, 1993.

[dJ]   M. de Jong. The TriggerEfficiency program. *ANTARES-SOFT-2009-001*.

[E+22]   R. Enomoto et al. The acceleration of cosmic-ray protons in the supernova remnant rx j1713.7-3946. *Astrophys. J. Lett.*, 416:823–826, 2002, arXiv:astro-ph/0204422.

[Eid04]   S. Eidelman. Review of particle physics. *Physics Letters B*, 592:1, 2004.

[EK]   Th. Eberl and C. Kopper. The SeaTray software framework. *ANTARES-SOFT-2009-013*.

[ESA]   ESA/Hubble. Microquasar. `http://www.spacetelescope.org/extras/posters/microquasar/`. website.

[FC98]   G. J. Feldman and R. D. Cousins. A unified approach to the classical statistical analysis of small signals. *Phys. Rev. D*, 57:3873, 1998.

[Fer49]   E. Fermi. On the origin of the cosmic radiation. *Phys. Rev.*, 75:1169, 1949.

[Fol]   Florian Folger. Private communication.

[Fol09]   Florian Folger. Reconstruction of neutrino induced hadronic showers with the ANTARES neutrino telescope. Diploma thesis, University of Erlangen-Nuremberg, Germany, 2009.

[G+]   M. Gault et al. Run-by-Run Monte Carlo and data quality. *ANTARES-PHYS-2011-016*.

[G+08]   T. J. Galama et al. An unusual supernova in the error box of the γ-ray burst of 25 April 1998. *Nature*, 395:670–672, 2008.

[G+68]   A. Giuliani et al. Neutral pion emission from accelerated protons in the supernova remnant w44. *Astrophys. J. Lett.*, 742:L30, 2011, arXiv:1111.4868.

[G+17]   G. Ghisellini et al. A theoretical unifying scheme for gamma-ray bright blazars. *Mon. Not. Roy. Astron. Soc.*, 301:451, 1998, astro-ph/9807317.

[Gai90]   T. Gaisser. *Cosmic rays and particle physics*. Cambridge University Press, 1990.

[GQRS96]   R. Gandhi, C. Quigg, M.N. Reno, and I. Sarcevic. Ultrahigh-energy neutrino interactions. *Astropart. Phys.*, 5:81, 1996.

[Gre66]   K. Greisen. End to the cosmic ray spectrum? *Phys. Rev. Lett.*, 16:748, 1966.

[GSv1]   T. K. Gaisser and T. Stanev. Neutrinos and cosmic rays. 2012, arXiv:1202.0310v1.

[GS06]   T. K. Gaisser and T. Stanev. High-energy cosmic rays. *Nuclear Physics A*, 777:98–110, 2006.

[H+87]   K. Hirata et al. Observation of a neutrino burst from the supernova sn1987a. *Phys. Rev. Lett.*, 58:1490, 1987.

[H+12]   Q. Dorosti Hasankiadeh et al. Performances of photo-sensors for KM3NeT. *Nucl. Instrum. Meth. A*, DOI: 10.1016/j.nima.2012.11.154, 2012.

[H⁺39]   A. Hoecker et al. TMVA - toolkit for multivariate data analysis. *PoS (ACAT)*, 040, 2007; arXiv:physics/0703039.

[Har06]   Bettina D. Hartmann. *Reconstruction of Neutrino-Induced Hardronic and Electromagnetic Showers with the ANTARES Experiment*. PhD thesis, University of Erlangen-Nuremberg, Germany, 2006.

[Hei04]   Aart Heijboer. *Track reconstruction and point source searches with ANTARES*. PhD thesis, Universiteit van Amsterdam, Netherlands, 2004.

[HK10]   Francis Halzen and Spencer R. Klein. IceCube: An instrument for neutrino astronomy. *Rev. Sci. Instrum.*, 81, 2010.

[HL]   Q. Dorosti Hasankiadeh and Herbert Löhner. Search for showers induced by diffuse flux of cosmic neutrinos. *ANTARES-PHYS-2012-011*.

[HoftHC00] W. Hofmann and others for the H.E.S.S. Collaboration. The high energy stereoscopic system (H.E.S.S.) project. *AIP Conf. Proc.*, 515:500–509, 2000.

[HR03]   G. C. Hill and K. Rawlins. Unbiased cut selection for optimal upper limits in neutrino detectors: the model rejection potential technique. *Astropart. Phys.*, 19:393–402, 2003.

[I⁺86]   G. Ingelman et al. LEPTO 6.5 - a Monte Carlo generator for deep inelastic lepton-nucleon scattering. *Comput. Phys. Commun.*, 101:108, 1997; arXiv:hep-ph/9605286.

[K⁺01]   F. Krennrich et al. Cutoff in the TeV energy spectrum of Markarian 421 during strong flares in 2001. *Astrophys. Journ.*, 560:45, 2001.

[KS07]   U. Katz and C. Spiering. High-energy neutrino astrophysics: Status and perspectives. *Prog. Part. Nucl. Phys.*, 67:651–704, 2012, arXiv:1111.0507.

[KW05]   T. Kashti and E. Waxman. Flavoring astrophysical neutrinos: Flavor ratios depend on energy. *Phys. Rev. Lett.*, 95:181101, 2005.

[LM00]   J. G. Learned and K. Mannheim. High-energy neutrino astrophysics. *Ann. Rev. Nucl. Past. Sci.*, 50:679, 2000.

[LP95]   J.G. Learned and S. Pakvasa. Detecting tau-neutrino oscillations at PeV energies. *Astropart. Phys.*, 3:267, 1995.

[LRR07]   William H. Lee and Enrico Ramirez-Ruiz. The progenitors of short gamma-ray bursts. *New Journ. of Phys.*, 9:17, 2007.

[Man95]   K. Mannheim. High-energy neutrinos from extragalactic jets. *Astropart. Phys.*, 3:295, 1995.

[MR93]   P. Meszaros and M. J. Rees. Relativistic fireballs and their impact on external matter- Models for cosmological gamma-ray bursts. *Astrophys. J.*, 275:278, 1993.

[NR43]   N. Nereson and B. Rossi. Further measurements on disintegration curve of mesotrons. *Phys. Rev.*, 64:199, 1943.

[Opp]   A. Oppelt. Detection of the moon shadow. *ANTARES-PHYS-2001-012*.

[P⁺07]   W. H. Press et al. *Numerical Recipes; the Art of Scientific Computing*. Cambridge University Press, third edition edition, 2007.

[Pre11]   Eleonora Presani. *Neutrino Induced Showers From Gamma-Ray Bursts*. PhD thesis, Universiteit van Amsterdam, Netherlands, 2011.

[Pro12]   R. J. Protheroe. Origin and propagation of the highest energy cosmic rays. *Phys. Rep.*, 327:109–247, 2000; arXiv:astro-ph/9612212.

[Rap09]   P. A. Rapidis. The NESTOR underwater neutrino telescope project. *Nucl. Instrum. Meth. A*, 602:54–57, 2009.

[RB47]   G.D. Rochester and C.C. Butler. Evidence for the existence of new unstable elementary particles. *Nature*, 160:885, 1947.

[RBZ03]   A. Romeyer, R. Bruijn, and J. D. Zornoza. Muon energy reconstruction in ANTARES and its application to the diffuse neutrino flux. In *Proc. The 28th International Cosmic Ray Conference, Japan*, 2003.

[Ree84]   M. J. Rees. Black hole models for active galactic nuclei. *Ann. Rev. Astron. Astrophys.*, 22:471–506, 1984.

[Roy99]   M. Roy. Ultra high energy neutrinos from supernova remnants. *J. Phys.*, 25:129, 1999.

[S$^+$98]   P. Sreekumar et al. Egret observations of the extragalactic gamma ray emission. *Astrophys. J.*, 494:523, 1998.

[Sik10]   M. Sikora. Hadronic jet models today. *Proceedings IAU Symposium*, 275, 2010.

[Sjo94]   T. Sjostrand. High-energy physics event generation with pythia 5.7 and jet-set 7.4. *Comput. Phys. Commun.*, 82:74, 1994.

[uIfHEI]   Inter university Institute for High Energies IIHE. Icecube neutrino observatory explores origin of cosmic rays. `http://w3.iihe.ac.be/press/press-2012-04-19.php`. website.

[V$^+$88]   J. C. Van Der Velde et al. Neutrinos from sn1987a in the IMB detector. *Nucl. Instrum. Meth. A*, 264:28, 1988.

[vdS$^+$40] E. van der Swaluw et al. Pulsar wind nebulae in supernova remnants. Spherically symmetric hydrodynamical simulations. *Astron. and Astrophys.*, 380:309–317, 2001, arXiv:astro-ph/0012440.

[WB97]   E. Waxman and J. Bahcall. High energy neutrinos from cosmological gamma-ray burst fireballs. *Phys. Rev. Lett.*, 78:2292, 1997.

[WB98]   E. Waxman and J. Bahcall. High energy neutrinos from astrophysical sources: An upper bound. *Phys. Rev. D*, 59:023002, 1998.

[Z$^+$10]   J. F. Zhang et al. High-energy neutrino emission from low-mass microquasars. *Monthly Notices of the Royal Astronomical Society*, 407:2468–2474, 2010.

[Zha97]   Z. Zhang. Parameter estimation techniques: A tutorial with application to conic fitting. *Image and Vision Computing Journal*, 15:59, 1997.

[Zij11]   Gerrit Zijlstra. Reconstruction of high-energy neutrino-induced showers in KM3NeT. Bachelor thesis, Rijksuniversiteit Groningen, Netherlands, 2011.

[ZK66]   G. T. Zatsepin and V. A. Kuzmin. Upper limit of the spectrum of cosmic rays. *JETP Lett.*, 4:78, 1966.

Presentations and Publications

Oral Presentations:

- Search for showers induced by a diffuse flux of extraterrestrial neutrinos, Karlsruhe Institute of Technology, Karlsruhe, Germany, 2012. (invited)

- Deep-Sea ANTARES Neutrino Telescope, IPM international school and workshop on Particle Physics, Tehran, Iran, 2012. (invited)

- Neutrino-induced showers in the ANTARES Deep-Sea Telescope, VLVnT workshop, Erlangen, Germany, 2011.

- Performance of Photo-Sensors for KM3NeT, VLVnT workshop, Erlangen, Germany, 2011.

- Detection of neutrino-induced showers with the ANTARES neutrino telescope, International School of Subnuclear Physics, Erice, Italy, 2011.

- Identification of shower-type events in the ANTARES neutrino telescope, NNV najaarsvergadering, Lunteren, Netherlands, 2010.

Poster Presentations:

- Detection of high energy neutrino-induced showers in the ANTARES Deep-Sea Telescope, International School of Subnuclear Physics, Erice, Italy, 2012.

- Neutrino track and shower events in the ANTARES Deep-Sea Telescope, Physics@FOM, Veldhoven, Netherlands, 2011.

Publications in Refereed Journals :

With Significant Own Contributions:

- Expansion cone for the 3-inch PMTs of the KM3NeT Optical Modules, S. Adrián-Martínez et al. (Q. Dorosti Hasankiadeh) , JINST, 8:T03006, 2013.

- Neutrino-induced showers in the ANTARES Deep-Sea Telescope, Q. Dorosti Hasankiadeh and Herbert Löhner, Nucl. Instr. and Meth. A, 725:110–113, 2013.

- Search for Showers Induced by Diffuse Flux of Cosmic Neutrinos, Q. Dorosti Hasankiadeh and Herbert Löhner, ANTARES-PHYS-2012-011, 2012.

- Performances of Photo-Sensors for KM3NeT, Q. Dorosti et al., Nucl. Instr. and Meth. A, 725:158–161, 2013.

- Multi-PMT optical module for the KM3NeT neutrino telescope, Q. Dorosti Hasankiadeh et. al., Nucl. Instr. and Meth. A, 695:338-341, 2012.

- Photo-sensors for a Multi-PMT optical module in KM3NeT, O. Kavatsyuk, Q. Dorosti Hasankiadeh and H. Löhner, Nucl. Instr. and Meth. A, 626:154–156, 2011.

With Contributions Through Data Taking and Analysis:

- Search for cosmic neutrino point sources with four years of data from ANTARES telescope, S. Adrián-Martínez et al. (Q. Dorosti Hasankiadeh) , Astrophys. Jour., 760:53, 2012.

- Measurement of atmospheric neutrino oscillations with the ANTARES neutrino telescope, S. Adrián-Martínez et al. (Q. Dorosti Hasankiadeh) , Phys. Lett. B, 714:224-230, 2012.

- The positioning system of the ANTARES neutrino telescope, S. Adrián-Martínez et al. (Q. Dorosti Hasankiadeh) , JINST, 7:T08002, 2012.

- Search for neutrino emission from gamma-ray flaring blazars with the ANTARES telescope, S. Adrián-Martínez et al. (Q. Dorosti Hasankiadeh) , Astropart. Phys., 36:204-210, 2012.

- A method for detection of muon induced electromagnetic showers with the ANTARES detector, J. A. Aguilar et al. (Q. Dorosti Hasankiadeh) , Nucl. Instr. and Meth. A, 675:56-62, 2012.

- Search for relativistic magnetic monopoles with the ANTARES neutrino telescope, S. Adrián-Martínez et al. (Q. Dorosti Hasankiadeh) , Astropart. Phys., 35:634-640, 2012.

- Measurement of the group velocity of light in sea water at the ANTARES site, S. Adrián-Martínez et al. (Q. Dorosti Hasankiadeh) , Astropart. Phys., 35:552-557, 2012.

- The ANTARES telescope neutrino alert system, M. Ageron et al. (Q. Dorosti Hasankiadeh) , Astropart. Phys., 35:530-536, 2012.

- First search for point sources of high-energy cosmic neutrinos with the ANTARES neutrino telescope, S. Adrián-Martínez et al. (Q. Dorosti Hasankiadeh) , Astrophys. Jour. Lett., 743:L14, 2011.

- ANTARES: The first undersea neutrino telescope, M. Ageron et al. (Q. Dorosti Hasankiadeh) , Nucl. Instr. and Meth. A, 656:11-38, 2011.

- A fast algorithm for muon track reconstruction and its application to the ANTARES neutrino telescope, S. Adrián-Martínez et al. (Q. Dorosti Hasankiadeh) , Astropart. Phys., 34:652-662, 2011.

- Search for a diffuse flux of high-energy ν_μ with the ANTARES neutrino telescope, J. A. Aguilar et al. (Q. Dorosti Hasankiadeh) , Phys. Lett. B, 696:16-22, 2011.

Acknowledgments

Looking back in time, I can admit that the completion of this dissertation has been one of the most intense academic challenges I have ever come across in my life, through which not only my academic knowledge and skills have been improved, but also my personality has positively developed. However, this dissertation would have never been completed without the supports, patience, guidance and company of many people to whom I owe my deepest gratitudes.

I would like to express the deepest appreciation to my promotor Prof. dr. Herbert Löhner, who has the attitude and the substance of a genius: he continually conveyed a spirit of adventure in regard to research, and an excitement in regard to education. Without his guidance and persistent discussions and supports this dissertation would not have been possible. Beyond all, his wisdom, insights and specially his commitment to the highest standards have deeply inspired me. I have to admit that having the opportunity of working with him have had tremendous positive effects on my current career and life as scientst. My gratitude to him is unabated.

Furthermore, I would also like to acknowledge with much appreciation the crucial role of Prof. dr. Maurizio Spurio as the supervisor of the physics analysis in the ANTARES collaboration. I had the opportunity to benefit from his constructive comments and his kind and consistent supports.

I would like to express my gratitudes to my reading committee members, Prof. dr. Ad van den Berg, Prof. dr. Paschal Coyle and Prof. dr. Maurizio Spurio for their careful reading of my manuscript and for their vaulable suggestions and comments.

I gratefully acknowledge the valuable discussions in the ANTARES Shower Group, in particular the supports by Florian Folger, and valuable comments and suggestions by Dr. Tommaso Chiarusi, Dr. Thomas Eberl and Prof. dr. Maurizio Spurio.

Special gratitude I owe to my colleague and friend Dr. Oksana Kavatsyuk. Considering my currently busy schedule, I could not imagine this work could have been finished smoothly without her kind and persistent supports. In addition, I owe my deep gratitude to her for her daily supervisions on the project concerning the development of the Multi-PMT Digital Optical Modules for the KM3NeT experiment. In addition, I would like to thank her for being always passionate, motivating and supportive during my PhD research. As an example, I would like to include here (with her permission) one of her paintings illustrating nicely the ANTARES infra-structure for Oceania research (see Figure).

I would like to thank Mohammad (Babai) for many hours of fruitful discussions we had over pattern recognition and machine learning subjects, through which I could learn many aspects of multidimensional statistical analysis which have been performed in this dissertation.

I would like to thank my friend Ruud for the translation of the Dutch summary. A special word of thanks is reserved for my valuable friends Mahmoud, Zohreh, Ali (Najafi) who helped me to design the nice cover page, and I would like to thank my paranymphs Oksana and Ali (Ghavami).

In addition, I would like to particularly appreciate the company of my best friends Ali (Najafi) and Ali (Ghavami), who have always been trustful, supportive and devoted friends, and have been great footholds specially during the hard times I faced in the past few years.

I cannot list all the people with whom I have shared many joyful and exciting moments at the KVI, however, there are some friends whose pictures and names flash into my mind as soon as I think about working at the KVI. Thanks to: Ali, Gianluca, Manisha, Olena, Olga, Oksana, Ganesh, Elmaddin, Hossein (Moeini), Mohammad (Babai), Myroslav, Marta (Kavatsyuk),

Miguel, Nasser, Fereshteh, Johan, Ola (Aleksandra), Siva, Maryam, Ayan, Nacho, Soumya, Roxana, Oliver, David, Krijn, Daniel, Stefano, Wendy, Ruud, Sybren, Hilde, Nafiseh, Zahrah, Ahmad, Masoud, Hans (Beijers).

My closing words go to my beloved parents, Alireza and Madineh, and my unique brother Qaran and my beautiful sister Sahar, who receive my inexpressible gratitudes and love for their endless dedication and the many years of unconditional support during every single moment of my life. I dedicate this dissertation to them.

<div align="right">

Qader Dorosti Hasankiadeh
Karlsruhe
Germany
September 1, 2013

</div>
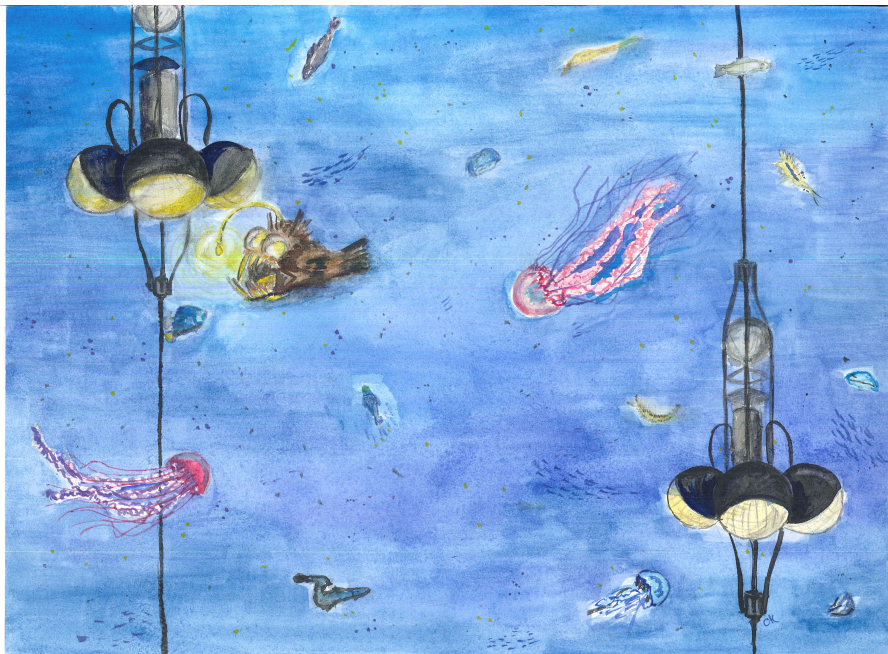
Artist's impression of Ocean research being carried out by the ANTARES deep-sea infrastructure. The picture is painted by Oksana Kavatsyuk.